On the Uncertainty of Space Debris Trajectory Predictions

Geul, J.

DOI
10.4233/uuid:1b4b7d8b-56cc-49aa-9b98-615241e08799

Publication date
2023

Document Version
Final published version

Citation (APA)
Geul, J. (2023). *On the Uncertainty of Space Debris Trajectory Predictions*. [Dissertation (TU Delft), Delft University of Technology]. https://doi.org/10.4233/uuid:1b4b7d8b-56cc-49aa-9b98-615241e08799

On the Uncertainty of Space Debris Trajectory Predictions

On the Uncertainty of Space Debris Trajectory Predictions

Dissertation

for the purpose of obtaining the degree of doctor
at Delft University of Technology
by the authority of the Rector Magnificus, prof. dr. ir. T.H.J.J. van der Hagen,
chair of the Board for Doctorates
to be defended publicly on Tuesday, 5 September 2023, at 15:00 o'clock

by

Jacco Geul

Master of Science in Aerospace Engineering,
Delft University of Technology, Delft, The Netherlands,
born in Vlaardingen, The Netherlands.

This dissertation has been approved by the promotors.

Composition of the doctoral committee:

Rector Magnificus,	chairperson	
Prof. dr. ir. P.N.A.M. Visser,	Delft University of Technology,	*promotor*
Dr. ir. E. Mooij,	Delft University of Technology,	*copromotor*

Independent members:

Dr. F. Silvestri,	TNO Optics
Prof. dr. T. Schildknecht,	Universität Bern, Switzerland
Ir. R. Noomen,	Delft University of Technology
Prof. dr. D.G. Simons,	Delft University of Technology
Prof. dr. ir. R.F. Hanssen,	Delft University of Technology

Reserve member:

Prof. dr. L.L.A. Vermeersen,	Delft University of Technology

Keywords: space debris, uncertainty propagation, conjunction analysis, re-entry prediction, interval analysis, regularisation, astrodynamics

Printed by: Ipskamp Printing

Front & Back: Painting by Jacco and Marja Geul

ISBN 978-94-6473-198-9

An electronic version of this dissertation is available at
http://repository.tudelft.nl/.

We are the local embodiment of a Cosmos grown to self-awareness. We have begun to contemplate our origins: starstuff pondering the stars; organized assemblages of ten billion billion billion atoms considering the evolution of atoms; tracing the long journey by which, here at least, consciousness arose. Our loyalties are to the species and the planet. We speak for Earth. Our obligation to survive is owed not just to ourselves but also to that Cosmos, ancient and vast, from which we spring.

Carl Sagan, Cosmos

CONTENTS

SUMMARY

Space debris presents a growing societal and technical problem. Space debris can be generative through fragmentation events, in which an object (e.g., a satellite), breaks up into many smaller pieces, for instance, as a result of a collision. Both the likelihood and severity of the risk related to fragmentations are increasing. The likelihood increases with an increase in the number of active and passive objects in space. Trends, such as the miniaturisation of satellites, the reduction of launch costs, and the fielding of mega constellations, all contribute to space becoming increasingly congested and contested. At the same time, the severity also increases as the societal, economic, and strategic reliance on satellite technology and space services grows.

The monitoring of the space environment, through space situational awareness (SSA), is key to the continued usage of space. Vital to this awareness is understanding which objects are present, through space surveillance and tracking (SST), and where these objects will be in the future, through orbit prediction and analysis. Specifically, conjunction analysis aims to predict which satellites have a high risk of collisions, and supports the planning of collision-avoidance manoeuvres, while re-entry predictions indicate possible ranges of impact locations and epochs for satellites returning back to Earth.

The goal of this research is to improve these types of predictions for space debris objects, to reduce the number of predicted satellite collisions and to improve the re-entry forecasting, and make space operations more sustainable and remain possible in the future. The focus is specifically on space debris objects, as opposed to active satellites, as the majority of objects in space are debris: currently, debris makes up 77 % of all observable objects, and practically 100 % of all objects, including also unobservable smaller objects.

Space-debris orbit predictions are very complex and rely on many different components, that are critical to the quality and ultimately the usability of these predictions. As a result, a number of the driving components is investigated, to understand and improve these individually, and as a result improve the prediction quality in general.

First, the current process of SSA of debris is investigated, including the way in which the states (e.g., position and velocity) of these objects are determined and how this information is shared. Space debris states serve as input for space-debris prediction methods and are thus very influential to the overall quality. In particular, the frequency by which these states are updated, the different parameters that are shared, and the accuracy of these parameters are instrumental in making good space-debris orbit predictions and are all researched in more detail.

Considering the types of sensors that are tasked with SST and their locations, the main consideration for the network is its capacity to provide regular updates on the state of the large number of objects. On the other hand, the parameters available and their accuracy are found to be most impacted by the particular format in which these states are shared. The two-line element (TLE) format presents the most widely available source

of state estimates on space debris publicly available. The two most important issues of TLEs are identified as the limited accuracy and the lack of covariance information. The accuracy is inherently limited by the Simplified General Perturbations (SGP) model, that was introduced in the 1970s, and has to be used to propagate TLEs. However, major advances in astrodynamics and information technology allow for more accurate models to be used. Yet due to its prevalence, the TLE format continues to persist. The lack of covariance information is most troubling. The covariance is used to give a measure of the accuracy of the state estimate. It is necessary to know this covariance specifically for the state estimate, as it is variant across different orbits, among different objects, and over time. The covariance is essential to space-debris orbit predictions, to make meaningful predictions of possible future states. To solve this issue, a method is developed to estimate the initial covariance, based on publicly available historic TLE data. The method is validated for a single satellite using GPS data and the results are shown to be in good agreement with the expected covariance. It remains necessary to replace TLEs with a more modern format and model, and include covariance information as obtained from the estimation process. Such a change requires the cooperation of the United States government, currently responsible for providing TLEs, or another organisation with similar space debris surveillance capabilities and a desire to publish these states timely and publicly.

Second, short-term re-entry predictions are examined. Particularly, what uncertainties in the state, but also in the modelling of the dynamic environment are driving the quality of these predictions. As a case study, the re-entry of the GOCE satellite is studied, on which a number of studies have been published, and for which various relevant datasets are available. Re-entry predictions using publicly available TLEs are compared to predictions based on much more accurate GPS solutions. In practice, GPS orbit solutions are, of course, not available for space debris. It is found that while the accuracy of TLE position and velocity is sufficient for re-entry predictions, its estimate of a ballistic coefficient is not. This even holds when the reported ballistic coefficient is disregarded and re-estimated to a higher fidelity. The best guess of the ballistic coefficient for TLEs suffers from aforementioned limited accuracy of the state itself, combined with a very limited time resolution. The precision, however, is primarily caused by large uncertainties in thermospheric density modelling. Currently, the predicted and actual density in these upper layers of the atmosphere can differ significantly. At present, the operational usefulness of re-entry predictions is limited, as it is only possible to make meaningful predictions on the impact time and impact location windows shortly before actual re-entry, in the order of hours. To improve these predictions more research into atmospheric density modelling is required.

Third, the models for predicting satellite states into the future have been investigated. A novel mathematical formulation of the equations of motion for propagating space object states is studied. This formulation is known as Dromo and employs regularisation to increase the numerical efficiency and accuracy significantly. Dromo was already shown to perform favourably against other regularised methods. In this research, the method is quantitatively compared to more traditional propagation methods. Dromo is found to be orders of magnitude more accurate and take significantly fewer function evaluations than traditional methods across a range of different space

debris orbit problems, making it very suitable for applications that require very high accuracy and/or a very low number of function evaluations. One practical limitation of Dromo is that time is a dependent variable, hence it is not possible to directly propagate to a pre-determined future epoch. To this end, a method is proposed to solve this issue, which has only minor impact on the total accuracy and has little computational overhead.

Lastly, Dromo is used for the problem of projecting the state uncertainty into the future. This uncertainty represents the volume of possible space debris states at a particular moment, and should account for all the errors due to imperfect knowledge of the initial state, as well as the errors in the dynamic models. An ideal uncertainty volume contains (nearly) all possible solutions, without being overly large. For applications where no solutions outside the uncertainty volume are acceptable, special interval methods exist that provide a verified solution containing all errors. The ability to provide verified solutions makes interval methods very powerful. However, the application of interval methods to space debris propagation is known to suffer from several issues. The primary issue is the interval explosion problem, where the uncertainty volume inflates so rapidly that it quickly yields impractically large, physically nonsensical, and, finally, mathematically unstable solutions. In this research, two improvements to verified space debris propagation have been proposed: a regularised formulation into an interval form and an improved interval state transformation method. This new propagator is shown to be much more stable than any previously published efforts. This allows the forecasting window to be prolonged from several hours to several weeks, improving the practical application of interval methods for space debris predictions. A continuation of this research into conjunction analysis of verified solutions of various space objects is promising and recommended.

This research looks at several aspects of space surveillance and tracking, and predictions. Various challenges are identified, for which solutions are developed and analysed. In all, this work contributes towards the aim of improving the predictions of space debris states and potential collisions.

These predictions fall within the larger context of SSA, which is one of many areas of research on the space debris problem. Space debris is a serious problem with many different aspects. At the end of the day, the problem should be addressed from all sides and simultaneously. The usage of space has a significant scientific, economic and sociological impact on our world. To continue to benefit and even increase this impact, it is necessary to treat space as limited resource and use it sustainably.

SAMENVATTING

Ruimteschroot vormt een groeiend maatschappelijk en technisch probleem. Doormiddel van fragmentatiegebeurtenissen kan ruimteschroot generatief zijn, waarbij een object (zoals een satelliet) opbreekt in vele kleinere stukken, bijvoorbeeld als gevolg van een botsing. Zowel de waarschijnlijkheid als de ernst van het fragmentatierisico nemen toe. De waarschijnlijkheid is gekoppeld met een toename van het aantal actieve en passieve objecten in de ruimte. Trends, zoals de miniaturisatie van satellieten, de goedkopere lanceerkosten, en de plaatsing van megaconstellaties, dragen er allen toe bij dat de ruimte steeds voller en betwister raakt. Tegelijkertijd neemt ook de ernst toe naarmate de maatschappelijke, economische en strategische afhankelijkheid van satelliettechnologie en ruimtediensten toeneemt.

Het monitoren van de ruimte, door middel van omgevingsbewustzijn in de ruimte (SSA of space situational awareness), is de sleutel tot voortdurend gebruik van de ruimte. Essentieel voor dit omgevingsbewustzijn is het vergaren van de aanwezige objecten, door middel van ruimtebewaking en volgen (SST of space surveillance and tracking), en waar deze objecten in de toekomst zullen zijn, door baanvoorspelling en analyse. Specifieke, conjunctie-analyse tracht te voorspellen welke satellieten een hoog botsingsrisico hebben, ter ondersteuning van onder andere manoevreplanning ter botsingsvermijding, terwijl voorspellingen van de terugkeer van satellieten naar aarde mogelijke inslaglocaties en tijdblokken aanduiden.

Het doel van dit onderzoek is om dergelijke voorspellingen voor ruimteschroot te verbeteren, het aantal voorspelde satellietbotsingen te verminderen en de terugkeervoorspelling te verbeteren, en ruimtevaartoperaties in de toekomst duurzamer te maken en mogelijk te houden. De focus ligt specifiek op ruimteschroot, in tegenstelling tot actieve satellieten, aangezien schroot de meeste objecten in de ruimte zijn: momenteel vormt schroot 77 % van alle waarneembare objecten en praktisch 100 % van alle objecten, inclusief ook niet-waarneembare kleinere objecten.

Baanvoorspellingen van ruimteschroot zijn zeer complex en berusten op veel verschillende componenten, welke cruciaal zijn voor de kwaliteit en uiteindelijk de bruikbaarheid van deze voorspellingen. Hiertoe wordt een aantal doorslaggevende componenten onderzocht om deze afzonderlijk te beschouwen en te verbeteren, met als doel de algehele voorspellingskwaliteit te verbeteren.

Ten eerste wordt het huidige SSA-proces van ruimteschroot onderzocht, inclusief de manier waarop de toestanden (zoals bijvoorbeeld positie en snelheid) van deze objecten worden bepaald en hoe deze informatie wordt gedeeld. De toestanden van ruimteschroot dienen als het begin voor voorspellingsmethoden en zijn dus van grote invloed op de algehele kwaliteit. Met name de bijwerkfrequentie van deze toestanden, de verschillende parameters waaruit ze bestaan en diens nauwkeurigheden, zijn cruciaal voor het maken van goede baanvoorspellingen en worden allen uitgebreid onderzocht.

Gegeven de sensortypes en -locaties binnen het ruimtebewakingnetwerk, is de belangrijkste overweging voor het netwerk het vermogen om regelmatig updates te geven over de toestanden van het grote aantal objecten. Aan de andere kant blijken de beschikbare parameters en hun nauwkeurigheid het meest bepaald te worden door het specifieke formaat waarin de informatie gedeeld wordt. Het two-line element (TLE) formaat is de meest gebruikte openbaar beschikbare vorm voor toestandschattingen van ruimteschroot. De twee belangrijkste beperkingen van TLE's zijn de beperkte nauwkeurigheid en het gebrek aan covariantie-informatie. De nauwkeurigheid wordt inherent gelimiteerd door het Simplified General Perturbations (SGP)-model, welke sinds de jaren 70 beschikbaar is, en gebruikt dient te worden voor voorspelling van TLE's. Echter, inmiddels kunnen er veel nauwkeurigere modellen gebruikt worden, vanwege vooruitgang in gebieden als astrodynamica en informatietechnologie. Desondanks, blijft door overweldigend gebruik het TLE-formaat bestaan. Het gebrek aan covariantie-informatie is het meest verontrustend. De covariantie is een maat voor de nauwkeurigheid van de toestandsschatting. Het is noodzakelijk om deze covariantie specifiek te kennen voor de toestandsschatting, aangezien deze veranderend is over verschillende banen, voor verschillende objecten en over de tijd heen. Voor zinvolle baanvoorspellingen van ruimteschroot is covariantie essentieel. Om dit probleem op te lossen, is een methode ontwikkeld om de initiële covariantie te schatten, gebaseerd op enkel openbaar beschikbare historische TLE-gegevens. De methode is gevalideerd voor een enkele satelliet met behulp van GPS- gegevens en de resultaten komen goed overeen met de verwachte covariantie. Het blijft nodig om TLE's te vervangen door een moderner formaat en model en covariantie op te nemen zoals verkregen uit het schattingsproces. Een dergelijke verandering vereist de medewerking van de regering van de Verenigde Staten, die momenteel verantwoordelijk is voor het produceren van TLE's, of een andere organisatie met vergelijkbare mogelijkheden voor ruimtebewaking en volgen van ruimteschroot, en tevens de begeerte heeft om deze toestanden periodiek en openbaar te publiceren.

Ten tweede worden korte-termijn terugkeervoorspellingen onderzocht. Vooral welke onzekerheden in de toestand, maar ook in de modellering van de dynamische omgeving, de voorspellingskwaliteit bepalen. Als casestudy wordt de terugkeer van de GOCE-satelliet bestudeerd, waarover reeds een aantal studies zijn gepubliceerd en verscheidene relevante datasets beschikbaar zijn. Terugkeervoorspellingen met behulp van openbaar beschikbare TLE's worden vergeleken met voorspellingen op basis van veel nauwkeurigere GPS oplossingen. Voor ruimteschroot zijn in de praktijk GPS-baanbepalingen natuurlijk niet beschikbaar. De nauwkeurigheid van de TLE-positie en -snelheid blijken voldoende voor terugkeervoorspellingen te zijn, echter de schatting van de ballistische coëfficiënt is dat niet. Dit geldt ook wanneer de gerapporteerde ballistische coëfficiënt niet beschouwd wordt en nauwkeurig opnieuw wordt geschat. De best mogelijke schatting van de ballistische coëfficiënt van TLE's is gelimiteerd door de combinatie van een beperkte toestandsnauwkeurigheid en een zeer beperkte tijdsresolutie. De precisie wordt echter voornamelijk beïnvloed door grote onzekerheden in de modellering van de thermosferische dichtheid. Momenteel kunnen de voorspelde en werkelijke dichtheid in deze bovenste lagen van de atmosfeer aanzienlijk verschillen. Op dit moment is het operationele nut van terugkeervoorspellingen beperkt, aangezien het enkel kort voorafgaand (enkele uren) aan de daardwerkelijk terugkeer mogelijk is zinvolle voorspellingen

te doen van betrouwbaarheidsintervallen van de impacttijd en impactlocatie. Om deze voorspellingen te verbeteren is meer onderzoek naar atmosferische dichtheidsmodellering nodig.

Ten derde zijn de modellen voor het richting de toekomst voorspellen van satelliettoestanden onderzocht. Een nieuwe wiskundige formulering wordt bestudeerd van de bewegingsvergelijkingen ter propagatie van toestanden van objecten in de ruimte. Deze formulering, bekend als Dromo, maakt gebruik van regularisatie om de numerieke efficiëntie en nauwkeurigheid aanzienlijk te verhogen. Dromo presteerde reeds zeer gunstig in vergelijking met andere geregulariseerde methoden. In dit onderzoek wordt de methode kwantitatief vergeleken met traditionelere propagatiemethoden. Dromo blijkt vele malen nauwkeuriger te zijn en aanzienlijk minder functie- evaluaties uit te voeren dan de traditionele methoden over een reeks van verschillende ruimteschroot baanproblemen, hierdoor is Dromo zeer geschikt voor toepassingen die een zeer hoge nauwkeurigheid en/of een zeer laag aantal functie-evaluaties vereisen. Een praktische beperking van Dromo is dat tijd een afhankelijke variabele is, waardoor het niet mogelijk is om direct naar een vooraf bepaald moment in de tijd te propageren. Hiervoor wordt een methode voorgesteld om dit probleem op te lossen, welke slechts gering effect heeft op de totale nauwkeurigheid en rekentijd.

Ten slotte wordt Dromo gebruikt voor het probleem van het voorspellen van de toestandsonzekerheid in de toekomst. Deze onzekerheid representeert het volume van mogelijke toestanden van ruimteschroot op een bepaald moment, en ontstaat uit alle fouten ten gevolge van onvolmaakte kennis van de begintoestand, evenals fouten in de dynamische modellen. Een ideaal onzekerheidsvolume bevat (bijna) alle mogelijke oplossingen, zonder al te groot te zijn. Voor toepassingen waarbij geen oplossingen buiten het onzekerheidsvolume acceptabel zijn, bestaan er speciale intervalmethoden die een geverifieerde oplossing bieden die alle fouten omvat. De mogelijkheid om geverifieerde te berekenen, maakt intervalmethodiek zeer krachtig. De toepassing van intervalmethoden op ruimteschrootbanen is bekend problematisch. De primaire complicatie is het interval-explosieprobleem, waarbij het onzekerheidsvolume zo snel groeit dat het al snel onpraktisch grote, fysiek onzinnige en, uiteindelijk, wiskundig onstabiele oplossingen oplevert. In dit onderzoek zijn twee verbeteringen aan geverifieerde propagatie van ruimteschroot voorgesteld: een geregulariseerde intervalformulering en een verbeterde methode voor interval-toestandstransformatie. Deze nieuwe propagator blijkt veel stabieler dan eerder gepubliceerd werk. Hierdoor kan verder in de toekomst voorspeld worden: van eerder enkele uren tot nu enkele weken. Hierdoor wordt praktische toepassing van intervalmethoden voor baanvoorspellingen van ruimteschroot vergroot. Een voortzetting van dit onderzoek naar geverifieerde conjunctie-analyse tussen meerdere ruimte objecten is veelbelovend en aanbevolen.

Deze voorspellingen vallen binnen de grotere context van SSA, één van de vele onderzoeksgebieden naar het probleem van ruimteschroot. Ruimteschroot is een serieus probleem met veel verschillende aspecten. Uiteindelijk moet het probleem van alle kanten tegelijk worden aangepakt. Het gebruik van de ruimte heeft een grote wetenschappelijke, economische en sociologische impact op onze wereld. Om te blijven profiteren en deze impact zelfs te vergroten, is het noodzakelijk om de ruimte als een beperkte natuurlijke hulpbron te behandelen en duurzaam te gebruiken.

1

INTRODUCTION

Launched in 1957 by the former Soviet Union, Sputnik 1 was the first artificial satellite in orbit around Earth. Since then, satellites have become increasingly important to society. Currently, there are nearly 6000 active satellites, fulfilling a range of scientific, commercial and military purposes. The total number of objects in Earth orbit is, however, much larger, at over 25 000 trackable objects [1]. Figure 1.1 shows the historic growth of the number of objects in Earth orbit, broken down into several object classes. This figure tells a history of spaceflight and will be referred to in this introduction. Note, for instance, the steep increases in fragmentation debris between 2005 and 2010 due to anti-satellite (ASAT) weapon tests. Furthermore, note the "hockey stick" exponential curve upwards in active payloads due to the arrival of mega constellations from 2015 to now.

Space exploration and exploitation has brought many benefits and opportunities, but also gives rise to challenges. Among these, space debris is a most severe threat. A sustainable approach to spaceflight and operations is necessary to ensure long-term access to and services in and from space.

The space-debris problem is becoming a familiar term outside the space sector. Section 1.1 defines what the problem is and why it matters. Following, Section 1.2 explains the underlying causes and different solutions. Zooming in, Section 1.3 introduces surveillance and tracking of space debris. Section 1.4 poses the research questions of the thesis. An outline of the research including the topics covered and how the research questions are addressed is given in Section 1.5.

1.1. SPACE-DEBRIS PROBLEM

To better understand the space-debris problem, it is decomposed using the method of risk analysis. Risk analysis can bring a deeper understanding of risks and how to deal with them more effectively. According to the NASA Risk Management Handbook risks need to be described using their three components [1]:

[1] Statistic and figures based on "Raw SATCAT Data" from https://celestrak.com/satcat/boxscore.php, accessed: May 28, 2022

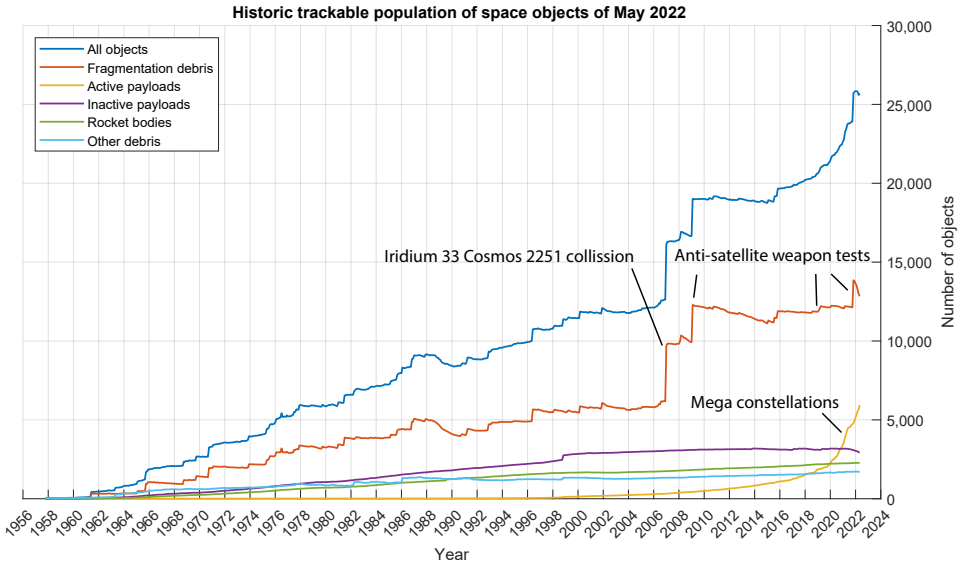

Figure 1.1: Historic growth of the population of catalogued objects in orbit for various object classes [1].

1. the scenario(s) leading to undesirable outcomes;

2. the consequence(s) (or impact) from the scenario(s) occurring, and

3. the likelihood(s) of the scenario(s) occurring.

In risk management, it is determined what, if any, action should be taken to reduce a risk. Mitigation is the taking of a positive action to address a risk, either through prevention or reduction of the likelihood, or reduction of the severity of the consequence [1]. As a result, the severity of the risk is lowered. The key concepts of scenario, outcome, consequences, likelihood, and mitigation are treated and applied to the space-debris problem.

The Kessler syndrome is the most threatening space-debris **scenario** and was popularised in the 2013 movie Gravity. Already in 1978, Donald Kessler envisioned a tipping-point where a positive-feedback loop occurs, which results in an uncontrolled growth of debris causing more collisions, causing more debris *et cetera* [2]. The scenario leads to an **outcome** where access to space is severely limited or even denied. As shown in Figure 1.1, space debris makes up the majority of objects in orbit at around 77 %. So far, only 17 confirmed collision events between space objects have been recorded [2]. Despite this relatively low number, collisions are very worrisome, as they are a major contributor to space debris and difficult or often practically impossible to prevent. Also, a collision involving an active spacecraft can lead to loss of the space mission. As orbits become more congested the risk of collisions is likely to increase.

[2] https://fragmentation.esoc.esa.int/home, accessed: December 14, 2021.

Consequences describe foreseeable and credible negative impacts in a quantitative and/or qualitative way [1]. Loss of space capabilities and access to space would have severe and far-reaching impacts. The consequences can be expected to continue to grow in severity as the usage of space steadily increases. In 2020, a report on the economic impact of the issue of space debris was published by the Organisation for Economic Co-operation and Development (OECD) [3]. The space sector is intricately interwoven in modern society, having many direct and derived impacts on science, technology, and economy [4]. In 2020, the commercial space industry made up 74 % of the space economy, which is around $ 371 billion of revenue in total per year [5]. Communications, finance, navigation, and other industries with a combined revenue of $ 10 trillion employ satellite technology [6]. As the application of space technologies continues to multiply, so will the impacts (direct and derived), but also the potential consequences. Moreover, space activities and exploration are a driver for innovation, culture and inspiration, and means to address global challenges. Ultimately, spaceflight is necessary for the long-term development and survival of humankind as a species [6–8].

Even at the current level of spaceflight activities, space debris is already generating significant additional costs for satellite operators, in the form of protection, mitigation and replacement costs. For instance, space debris poses the need for (additional) manoeuvring capabilities and propellant. Also, more redundancy is required in both the spacecraft and constellation design, for example, through additional spare satellite systems. Moreover, insurance and operations costs are increased. Space debris is also very demanding on space surveillance and tracking, due to the high number of inactive objects (roughly 77 % of the total population) and the relatively small size of most of the debris. Operators of geostationary orbit (GEO) satellites have estimated protective and mitigation costs at 5 % to 10 % of the total mission costs. This aspect has not been investigated for satellites in low-Earth orbit (LEO), but the percentage is expected to be higher [3].

Likelihood is the probability of occurrence of a scenario associated to a risk [1]. At first order, the likelihood of an arbitrary collision occurring is related to object density. The density can be broken down into the number of objects and the distribution (or concentration) of objects in space. As demonstrated by Figure 1.1, the number of objects is increasing over time at an increasing rate. So, next to the consequences, the likelihood too is growing over time and will continue to grow into the future.

To better understand the number of objects and the current and future situation, one can consider a few of the underlying trends. First of all, space usage and satellite technology are rapidly changing. Over the last decades a number of innovative trends, such as miniaturisation, mega constellations, small and reusable launchers, and broadband communications has become reality. Due to advances in technology, smaller and more affordable satellites have made space much more accessible. As a result, the number and type of owners and operators are expanding, and include governments (civil and military), large businesses, start-ups, universities, and even private individuals. Over 80 countries own at least one satellite, and between 2015 and 2019 over 500 small space companies were established [4]. The space economy and the number of satellites is only expected to continue to grow. Figure 1.1 clearly shows an exponential growth in the number of active payloads between 2013 and now. This increase is primarily due to

new (mega) constellations. Such constellations are announced regularly; presently a list of the most notable owners, constellation name, and number of satellites currently in orbit includes: SpaceX (Starlink constellation; 3524 satellites in orbit), Planet (Flock, Dove and SuperDove; together 519 satellites), OneWeb (428), Spire (Lemur; 160), and Swarm Technologies (SpaceBEE; 177) [3]. Still, this is only a fraction of the total number of satellites planned for such constellations. Not all initiatives announced will materialise, but a total of 12 686 satellites are planned when considering constellations that have already one or more (demonstrator) satellite(s) in orbit [1]. Note that there is always a possible mismatch between the number of planned and realised satellites. For instance, Starlink has been granted approval for 12 000 satellites and has requested approval for another 30 000 satellites. Yet, currently, Starlink Generation 1 is expected to consist of 7518 satellites; Starlink Generation 2 is also not included in the total due a lack of active satellites [4]. The recent exponential growth in Figure 1.1 is mostly in the class of active payloads for now. It is too early to understand the sustainability of mega constellations and how this will impact the other object classes.

The likelihood is further affected by the concentration of space objects. Depending on the application, certain orbits are particularly attractive. As a result, satellites are not uniformly distributed in space, but are clustered in a handful of favourable orbits. Figure 1.2 shows the distribution of space objects over orbital period and inclination. A direct relation exists between the orbital period and the altitude of a satellite. High concentrations are apparent from the figure. The highest score, at 14 revolutions per day and around 100° inclination, represents nearly 20 % of the total number of objects. The particular bin covers orbital altitudes from 725 to 1072 km, assuming a circular orbit. This bin coincides with the so-called Sun-synchronous orbits (SSO), which are attractive for Earth-observation purposes. Various other concentrations are visible elsewhere in LEO and in MEO (e.g., at twice-a-day orbital period) and GEO (once-a-day period).

Due to the large number of objects involved and the continuously evolving population, there exist large uncertainties in the scenarios leading to potential collisions. Long-term prediction models aim to forecast the evolution of the space-object population over decades to investigate phenomena, such as the Kessler syndrome. To account for uncertainties, the models are generally run in various scenarios that consider different preconditions and mitigation policies. An Inter-Agency Space Debris Coordination Committee (IADC) modelling study compared various models to assess the debris population stability [9]. All six models consistently predicted a growth in the LEO debris population in a business-as-usual scenario. In the current state, catastrophic collisions are expected to occur every 5 to 9 years. This suggests that strategies are necessary to halt or reverse the debris-population growth, before the tipping point in the Kessler syndrome scenario is reached.

[3] Analysis based on NewSpace Constellations list from https://www.newspace.im/, accessed: November 11, 2022 .

[4] https://en.wikipedia.org/wiki/Starlink#Constellation_design_and_status, accessed: May 28, 2022.

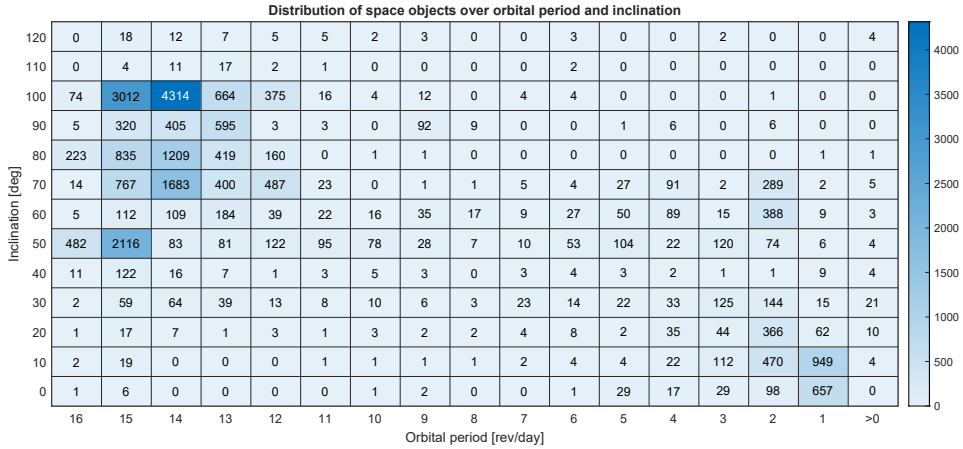

Figure 1.2: Heat map of current trackable space objects as a function of their orbital period and inclination [1].

1.2. CAUSES AND MITIGATION

Debris objects are the major class of objects and can be generated in a number of different ways. It is useful to distinguish debris types by their source. Each source can require different **mitigation** approaches to reduce its number. Debris objects include dysfunctional satellites, natural objects, break-up debris, rocket parts (such as boosters and farings), *et cetera*. Man-made objects almost entirely make up the space debris. They cover a wide range of mass and sizes. Nearly 20 000 debris objects presently in orbit are catalogued. The true population is much greater, though. Roughly, there are 36 500 objects larger than 10 cm, one million objects larger than a cm, and 130 million objects larger than one mm [5].

Larger objects (larger than 10 cm) are generally observed and tracked using ground-based sensors [10]. The smaller objects are estimated through statistical models based on empirical data from specific satellite missions; actual locations are unknown.

Fragmentations of space objects are an important mechanism in the Kessler syndrome. As one object fragments into multiple and sometimes up to thousands of new objects, the likelihood of collisions increases at nearly equal rate. Fragmentation debris already makes up over 50 % of all trackable objects and nearly all untracked objects. Figure 1.3 shows the fragmentation debris broken further into several underlying causes. At a high level it is possible to distinguish between deliberate and accidental fragmentations, and fragmentations involving a single or multiple satellites [6]. Deliberate fragmentation, due to (self-)destruction or a controlled collision, accounts for 32 % of the fragmentation debris currently in orbit. Historically, this number has been 32 %. It is surprising that these numbers are equal given the controversial nature of deliberate fragmentations. The 1967 Outer Space Treaty bans the stationing of weapons of mass de-

[5] https://www.esa.int/Safety_Security/Space_Debris/Space_debris_by_the_numbers, accessed: February 27, 2022.

[6] All data from retrieved from https://fragmentation.esoc.esa.int/home, accessed: December 14, 2021.

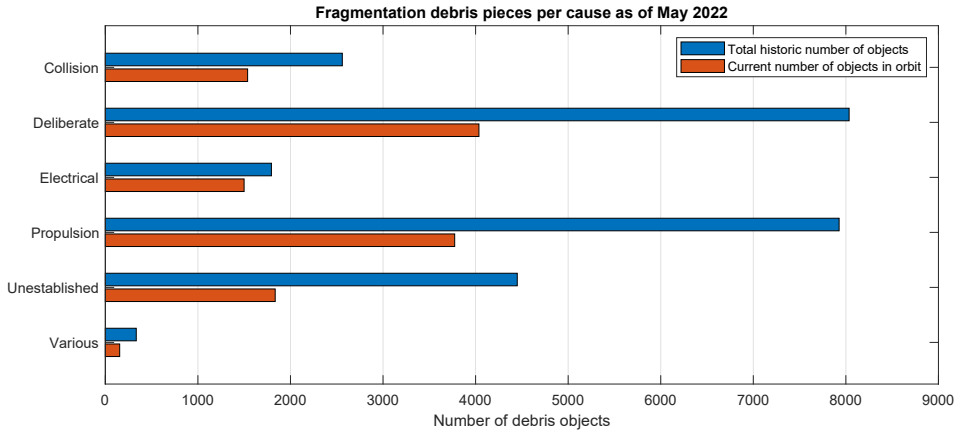

Figure 1.3: Break-up of the number of current and total historic debris objects in the fragmentation debris class into subclasses.

struction and prohibits testing of "any type of weapons" in space [11]. There have been 58 intended fragmentation events to date, of which 47 events happened cold war (44 by the USSR). In the light of current space debris awareness, these events are very controversial. Nevertheless, there have been four intentional fragmentations by four nations as part of anti-satellite (ASAT) tests over the last 15 years. All events were followed by strong international condemnation. In 2007, the Chinese Fengyun 1C polar-orbiting satellite was destroyed. The event created 3519 catalogued fragments and over half a million objects larger than one cm. Due to the high altitude of 865 km, it is expected that 80 % will remain in orbit for at least another century [7]. In 2009, the USA destroyed USA-193 in its orbit at 252 km altitude. The event created 174 pieces of space debris, of which 99 % re-entered within six months. In 2019, India tested an intercept on Microsat-R at 282 km altitude. Similarly, at this low altitude nearly all of the 400 identified objects have since re-entered. As recent as November 2021, during a Russian interceptor test Cosmos-1408 was destroyed in its orbit at 485 km altitude. The destruction resulted in over 1500 trackable fragments and hundreds of thousand suspected smaller pieces [11]. It would seem that the category of deliberate fragmentations is entirely preventable. The solution here lies in international politics and diplomacy [12].

Accidental fragmentation, especially caused by collisions, are difficult to prevent. Residual propellants in rocket bodies and batteries in spacecraft can become unstable and explode over time. Moreover, tanks, reactor cores and batteries can start leaking. These risks can be mitigated through passivation and spacecraft design. Passivation entails the depletion of any system that contains residual energy that might become unstable over a long period, such as batteries and propellant tanks. Mitigation policies that target design and operations are effective in reducing these types of fragmentations.

Orbital collisions can be catastrophic due to the high relative velocity. These events can shatter a satellite into thousands or more pieces. Seventeen collisions, for which

[7] https://celestrak.com/events/asat.php, accessed: December 14, 2021

either one or both objects are known, have been recorded so far. The collision between the Iridium-33 and the inactive Cosmos-2251 satellites in 2009 is by far the most prominent to date [13]. Three years after the collision, 2201 fragments were catalogued, of which only 315 had decayed [8]. Over the last decade another 168 objects have been tracked and confirmed; in total 1419 objects remain in orbit today.

Preventing collisions is an important aspect to limit the growth of space debris. Collision avoidance (COLA) is operationally practiced. However, successful avoidance can only occur if 1) the to-be-colliding objects are detected and tracked, 2) the conjunction is predicted well enough in advance, 3) at least one of the satellites is active, 4) the active satellite is able to manoeuvre 5) the operators act on the warning.

Space Traffic Coordination (STC) entails the coordination of data sharing and actions, such as responses to conjunction warnings, but is still in its infancy. STC is part of the larger effort of Space Traffic Management (STM), which aims for safe and sustainable space operations [14]. Inherently, this requires a high percentage of actively controlled satellites to be effective. At the moment only 23 % of all catalogued objects are active payloads, of which only a fraction has manoeuvring capabilities.

STM alone can not provide a solution to the space-debris problem. Additionally, a balance between the generation and removal of objects needs to be established. Ultimately, a reduction of the number of space-debris objects is required. A reduction of space debris will reduce the likelihood of conjunctions and increase the fraction of active payloads, making STM more effective. Reduction can be achieved by removing existing pieces, especially from densely populated orbits.

Preventing the generation of unnecessary new debris, and removal of the inevitable debris must be part of a long-term solution. End-of-life policies dictate the proper removal of objects from important regions. The IADC has defined two protected regions, namely LEO up to 2000 km and GEO $36\,000 \pm 200$ km, and there is an ongoing discussion to include medium-Earth orbit (MEO) as a protected region [15]. Policies and guidelines dictate how removal from these protected regions can occur. In the case of the Space Debris Mitigation Policy for ESA contractors and the European space industry [16] LEO satellites should clear LEO within 25 years after end-of-life. Recently, the FCC has even adopted a 5-year rule [9].

In LEO, removal of space objects is achieved through various means. Natural decay is the most simple solution. In principle, all Earth-orbiting objects experience atmospheric drag and energy loss as a result. The time it takes for an object to decay and re-enter the Earth's atmosphere depends on the original orbital altitude and satellite design. If natural decay does not occur within the desired period, active removal or accelerating the natural decay is necessary. De-orbiting is done by the satellite using propulsion, drag augmentation or tether systems. For high-LEO (above 1200 km), MEO and GEO satellites de-orbiting requires too much propellant and is not feasible. These satellites typically clear the protected regions by transferring to a so-called graveyard orbit. This graveyard orbit is stable on very long time-scales. Active or passive disposal ensures that spacecraft clear protected orbital regimes at end of life and are often regulated.

[8] https://celestrak.com/events/collision/, accessed: December 14, 2021

[9] https://www.fcc.gov/document/fcc-adopts-new-5-year-rule-deorbiting-satellites-0, accessed November 11, 2022.

Except for natural decay, all methods require the satellite or a subsystem to be active to facilitate its disposal. Satellites that fail or any of the current debris cannot actively comply with the guidelines. This necessitates the concept of active debris removal. Here, another spacecraft or system is used to dispose of debris objects. However, active debris removal is very challenging and expensive to execute. It is therefore only feasible for a small number of objects, such as high-priority targets.

Even small undetectable objects can cause satellite malfunction and fragmentation events. These types of collisions happen much more often, but are also hard to detect and nearly impossible to avoid. Several incidents of collisions between satellites and untracked objects are suspected. The evidence is a sudden unexpected loss of function or a slight change in the satellite's orbit [17]. Collisions with unseen space debris can only be statistically predicted using flux models, such as MASTER (Meteoroid and Space Debris Terrestrial Environment Reference) and ORDEM (Orbital Debris Engineering Model) [18]. The risks are assessed and can only be mitigated during the mission design, for instance by making the satellite more resilient or selecting a safe(r) nominal orbit. The empirical input and validation data for these models is limited. In a few special cases observations have been made during inspection of micro-meteorite impacts on space stations, Space Shuttles, and from satellites. Many experiments were enabled by the Space Shuttle program, such as the Long Duration Exposure Facility (LDEF) in 1990, the servicing of the Hubble Space Telescope in 1993, and the retrieval of European Retrievable Carrier (EuReCa) also in 1993. Several missions have been designed to specifically collect data using in-situ detectors, such as GORID, and DEBIE on board PROBA-1 and DEBIE II on board the ISS [18].

Several aspects of the growing space-debris population and ideas for approach have been presented here. A single strategy is not enough to manage the entire problem, however. For instance, a perfect adherence to end-of-life policies does not prevent accidents within the current population and is susceptible to satellites prematurely failing. Also, traffic coordination and collision avoidance alone cannot prevent the high fraction of non-active satellites from colliding. Instead, all solutions need to contribute and have to be worked on and implemented in parallel.

1.3. SPACE DEBRIS SURVEILLANCE AND TRACKING

Space Surveillance and Tracking (SST) concerns detecting, identification, tracking, and prediction of the orbits of objects. Through detection new objects can be discovered and existing objects can be revisited. Subsequent detections result in tracking with the aim of accurately determining orbital and related parameters. Through correlations with previous and external data, an object can be repeatedly identified and catalogued. Orbit predictions allow for future scheduling of detection opportunities and derived applications, such as conjunction analyses and re-entry predictions.

Space debris presents one of the principle threats to the space infrastructure. The focus of the thesis is space surveillance and tracking of debris objects, and in particular on making predictions. By nature, space-debris objects are non-cooperative and thus require general approaches and methods. SST is a part of the broader domain of Space Situational Awareness (SSA), which also includes space weather and near-Earth objects (NEO) [19].

Monitoring space has been a critical aspect for national security for many countries since the 1960s. Space monitoring arose with the desire to provide early warning of incoming ballistic missiles. The tracking and cataloguing of satellites proved important in preventing false alarms and maintaining an overview of domestic and foreign space assets. With the growth of spaceflight the maintenance and publication of object databases were also realised. These databases are the basis for many space (debris) prediction activities and analyses [20].

The largest database is the Satellite Catalog (SATCAT) and is maintained by the United States Space Command (USSPACECOM). SATCAT contains over 25 000 space objects currently in orbit, as shown in Figure 1.1. Objects in the database are detected and updated by the Space Surveillance Network (SSN). The SATCAT is published online through Space-Track.org and contains both current and historic data [10]. Different websites republish SATCAT data in different formats, most notably CelesTrak [11] and Privateer Wayfinder [12]. Space-Track publishes estimation data in the form of Two-Line Elements (TLEs). TLEs are a compact format of orbital tracking data, containing the estimated ephemeris and related data [21]. Only objects that are large enough to be regularly tracked by the SSN are included in SATCAT. SATCAT continues to be the largest up-to-date public database that covers the largest number of orbiting objects. Only data on unclassified objects are publicly available. Services using TLE data, such as the Satellite Orbital Conjunction Reports Assessing Threatening Encounters in Space (SOCRATES) [22], might, therefore, not have all relevant data available. Satellites vital to US national interest are classified and omitted from the public database. In 2005, the number of classified payloads was about 184. Together with their associated rocket bodies and upper stages and other unreported objects, this resulted in almost 8 % of the total number of tracked objects having their orbital data unavailable [22]. More recent numbers are not available.

The need for accurate and timely SST data continues to grow. There is always a demand for more frequent updates, more accurate ephemeris, and smaller objects to be tracked [19]. In the last few years, several major advances in SST have been realised. Specifically, new electronically-advanced radar systems capable of searching and tracking have become operational. LeoLabs is a new company that has a network of four radars for tracking satellites and debris. Especially the Kiwi space radar (KSR) (operational since 2019) and the Costa Rica space radar (since 2021) are powerful S-band radars that have a large capacity and detect previously unseen space debris. LeoLabs tracks over 20 000 unique objects each month [13]. In March 2020, the new Space Fence System (SFS) radar became operational. The SFS is currently the most advanced space radar for LEO, with a higher capacity and able to detect smaller objects (“marble sized”) than previous SSN systems [14]. Meanwhile, more nations are developing their own national SST capabilities. The new bi-static radar system named GESTRA was completed in October 2020 at the German Space Situational Awareness Centre (GSSAC) [15]. Currently, the Royal Neth-

[10] https://www.space-track.org
[11] https://celestrak.org/NORAD/elements/
[12] https://www.privateer.com/
[13] https://platform.leolabs.space/system_metrics, accessed: May 28, 2022
[14] https://www.lockheedmartin.com/en-us/products/space-fence.html, accessed: May 28, 2022.
[15] https://www.dlr.de/content/en/articles/news/2020/04/20201013_space-radar-gestra-beg

erlands Air Force is replacing its two air surveillance radars with new SMART-L ELR MM system, capable of space surveillance [16]. Many of these national sensor systems can contribute to the SSN, next to their primary and auxiliary tasks.

Tracking of space objects results in orbital ephemeris that describe a satellite state at a certain moment of time. The satellite state can be its explicit position and velocity, or some form of orbital elements. An ephemeris can be used as a point of departure for predicting future and past positions. For instance, when a satellite might pass over a certain location on Earth, or when it is at closest distance to another satellite, *et cetera*. Orbital ephemeris are invariably linked to the dynamics model that is used for generating them, and must also be used for further processing.

Due to the long-term popularity of SATCAT, TLEs have become synonymous with orbital ephemeris to many users. Many tools read and produce the TLE ephemeris format. Consequently, also other data providers publish TLE data [21]. Despite its popularity the TLE format is limited and has become outdated in several respects. To understand the limitations, it is necessary to first understand the history of the format. The development of TLEs and the corresponding dynamics model (the Simplified General Perturbations (SGP)) started in the 1960s, became operational in the early 1970s, and was officially released in 1980 [23, 24].

Since ephemeris are always linked to a dynamics model, the TLEs and the SGP4 model need to be regarded as a pair. Even though a TLE can be converted to many other state representations, it remains at its core a TLE. Even using the same exact version of the model (code compatibility) is important [25]. However, due to the many unofficial versions of the model, lack of new official releases, and no inclusion of the model version in the TLE data, knowing what dynamics model was used, and properly matching of data and model can be difficult. Even the operational code for generating TLEs has changed several times in its history [25, 26].

The accuracy of TLEs is related to the accuracy of the SGP4 model. SGP is a mean motion model. The model allows for propagation for long durations, despite its simple force models, but with limited accuracy at any particular point in the trajectory. A higher accuracy at particular points in the orbit is desired for specific types of analysis such as for computing potential conjunctions and collision probabilities. Another downside of TLEs is the lack of state covariance information. A state covariance is an expression of the uncertainty of a predicted state. This means that although an orbital state is published, there is no indication on how accurate or inaccurate that particular state is. The TLE state uncertainty is significant and can be in the order of a few kilometres [27]. Some form of uncertainty information is necessary for any type of statistical analysis. In conjunction analysis, covariance information is used to compute collision probabilities. Similarly, position covariance can be translated to confidence intervals of re-entry epochs or sensor search areas. Unfortunately, the state covariance is not published along with TLEs in the SATCAT. Methods for retro-actively estimating the state covariance exist. Empirical covariances based on historic data of one or many objects are useful guidelines, but the true covariance of a specific TLE can vary day-to-day and is dependent on many

`in-operation.html`, accessed: December 16, 2021

[16] https://www.defensie.nl/actueel/nieuws/2020/01/17/nieuwe-ogen-voor-luchtgevechtsleiders, accessed: December 14, 2021.

factors, including the sensor system used, quality of the measurements, type of orbit, space weather conditions *et cetera* [21]. Lastly, a TLE also lacks proper satellite parameter estimates. These parameters are specific to each satellite and determine the effect of different perturbations. For instance, solar radiation pressure coefficient and attitude parameters are not modelled in SGP and therefore not provided. Moreover, the TLE contains a drag term (called BSTAR) that provides a measure of the combination of the satellites mass, drag coefficient, and drag area, but is known to be a sensitive and often unreliable parameter in TLEs.

1.4. RESEARCH QUESTIONS

Space debris presents one of the largest threats to spaceflight and poses an enormous risk to modern society. Knowledge of the space-debris population and in particular towards the space surveillance and tracking, and orbit prediction of space-debris objects is at present limited in several key areas. Therefore the aim of this research is:

> **To improve space-debris orbit prediction and analysis, to facilitate reducing the number of potential satellite collisions and improving re-entry and impact location forecasting.**

The research focuses on the major space-debris population that is located in low-Earth orbit. Moreover, the research considers public data and frequently updated data sources.

The primary research question is:

> **What aspects of space-debris trajectory modelling and propagation impact the quality of space-debris orbit predictions?**

Several additional research sub-questions are derived, which focus on particular aspects of the primary research question and aim.

Space surveillance and tracking are instrumental to space situational awareness and understanding. Space surveillance, especially of space debris, requires a very broad scope: frequent observation of many objects of a wide range of sizes and make-up, distributed over a wide range of orbits. This constitutes a very large surveillance effort, reserved for (cooperation between) nations and large (government-funded) commercial entities. To better understand the input into space-debris predictions, it is necessary to understand how orbit ephemeris data of debris objects is constructed. To this end, the following research sub-questions need to be addressed:

> **What space surveillance data sources on space-debris orbits are available, how do they come about, and how are they disseminated?**

> **What are the primary gaps and limitations of these data for performing space-debris analysis and predictions?**

Large orbital ephemeris data sources are necessary, but not always optimised for space-debris investigations. To make available data more suitable for space-debris predictions, it should be investigated whether it is possible to deal with or mitigate these limitations in the modelling and simulation. This leads to the following sub-question:

How can modelling and simulation address the current gaps and limitations in space surveillance and tracking data for the purpose of debris analysis and orbit predictions?

To understand space-debris orbit predictions, it is necessary to look at the entire prediction chain; from the various input data, to environment and spacecraft modelling, uncertainty propagation, and finally predictive analysis. Moreover, it is necessary to not only look at this problem academically, but also to take operational aspects into account.

For this research high-accuracy and high-resolution data on the re-entry campaign of the GOCE satellite was provided by the European Space Agency (ESA). The dataset is valuable for studying short-term re-entry predictions, such as the sensitivity analysis of models, model parameters, and modelling fidelity. Moreover, the re-entry data allows for steps in verification and validation of currently operational trajectory-prediction methods. The following research sub-questions are aimed to address this:

What are the primary drivers of short-term re-entry prediction accuracy? How well do currently operational re-entry predictions perform and how can they be further improved?

The propagation of orbital ephemeris is central to space-debris orbit predictions. Orbital state and uncertainty propagation refers to the process of extrapolating a historically known satellite position, velocity and covariance into the future. For space-debris trajectory propagation in general, the forecasting periods are typically in the order of hours to several days. For a given initial state and covariance, it is important to introduce as little error as possible in the propagation process to obtain the most accurate predictions and/or extend the forecasting window. Moreover, the number of predictions can be significant, depending on the number of space-debris objects under consideration and analysis methods used. For instance, Monte Carlo uncertainty propagation might require thousands of trajectories per single object. Thus, next to the accuracy, also the (numerical) efficiency and robustness of a propagation method should be considered. The following research sub-question addresses these aspects:

How can the propagation of space-debris trajectories be made more efficient and robust?

The problem of propagation of satellite uncertainty over longer forecasting periods is very difficult. Especially when the environment itself is also uncertain. For LEO the motion is highly non-linear and there exist large uncertainties in the dynamics models, especially in the instantaneous atmospheric density. Different error propagation methods exist to transform an initial uncertainty to a desired epoch for further analysis. Verified numerical analysis covers a class of methods that provide a guaranteed uncertainty solution and are common in, for instance, analysis of NEOs. While promising, the application to LEO space debris is still very new. To further investigate its applicability to the problem of space debris, the following sub-question is posed:

How can verified numerical analysis techniques be applied to space-debris propagation? What are the main challenges and how can they be overcome?

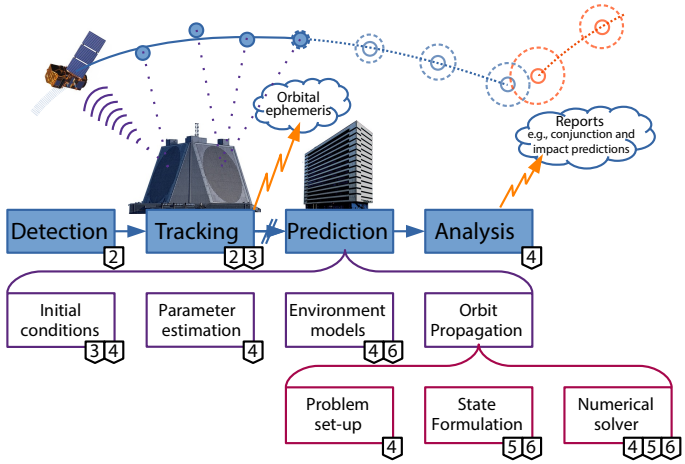

Figure 1.4: Graphic overview of the space-debris surveillance and tracking chain and breakdown into topics covered in this thesis, where the numbers correspond to the respective chapters.

The background of the space-debris problem has been presented. In the area of SST of space debris, one overarching research question and six specific sub-questions have been posed. These questions will be addressed in the remaining chapters of this thesis.

1.5. RESEARCH OUTLINE

Figure 1.4 shows a high-level diagram of the space-debris surveillance, tracking, and prediction chain. The chain consists of many components and those covered in this research have been broken down further. Each component affects the entire chain and, therefore, has the potential to improve the overall quality and contribute towards the research aim. A discontinuity is illustrated between tracking and prediction, to highlight an important split in the activities. At this split, the interface is orbital ephemeris data. The primary focus of this thesis is on space-debris trajectory prediction and specifically on (error) propagation, but with regard to the overall chain. Relevant chapter numbers have been indicated for each component.

Chapter 2 deals with the physical network that is responsible for maintaining SATCAT and the estimation of its individual TLEs. The purpose of this chapter is to provide a sense of the scale of this network, the individual sensors that make it up, and how the network geometry and the addition of sensors influence the entire tracking performance. Chapter 3 provides an analysis of the accuracy of TLEs. The modelling and estimation of TLE errors is investigated. A new method for TLE covariance estimation is presented. This covariance is a crucial aspect of the initial state in space-debris trajectory predictions. A high-fidelity simulation model of the entire short-term re-entry prediction chain is investigated in Chapter 4. Re-entry predictions are performed using uncertain initial conditions and in a stochastic environment. The sensitivity of the prediction to the model parameters is highlighted. The high-fidelity model is used for predicting the re-entry of the GOCE satellite and compared against historic operational predictions.

Orbital-state propagation accuracy and efficiency are examined in Chapter 5. Specifically, regularised orbital elements are compared against (classical) orbital elements and Cartesian coordinates on various orbits. Chapter 6 deals with propagation of uncertain initial conditions through an uncertain environment using verified numerical analysis. The effect of orbital formulation and initial error computation on numerical stability of verified solutions is investigated. Finally, Chapter 7 presents the major conclusions and answers to the research questions, and recommendations from this dissertation.

2

Modelling and Assessment of the Current and Future Space Surveillance Network

Geul, J., Mooij, E. and Noomen, R.

Published [1] in Proceeding of the 7th European Conference on Space Debris, 2017

Two-Line Elements (TLEs) and Tracking and Impact Predictions (TIPs) resulting from the Space Surveillance Network (SSN) are important for many Space Situational Awareness (SSA) activities. The network consists of many different radar and optical stations, contributing in either a dedicated, collateral or contributing fashion. For the majority of objects in low-Earth orbit (LEO) phased-array radar (PAR) stations are essential for maintaining the satellite catalog (SATCAT). A survey of the current state of the SSN and a methodology for simulating the network is presented. The current state is compared to a future scenario with the new Space Fence System (SFS) included. The SSN is simulated as a collection of current and hypothetical dedicated and collateral PARs. The location and coverage of each sensor is investigated and modelled. Observations are generated for a test rocket body in LEO. TLEs are estimated from the simulated measurements using the Simplified General Perturbations (SGP4) model. The sensitivity of the fit residuals and propagated accuracy with respect to eccentricity, inclination, and number of observations and sensors is analysed. The orbit-determination solution is found to be most sensitive to the eccentricity, and number of observations and sensors involved. The new SFS improves the solution, especially for lower inclinations.

[1] Minor modifications have been made for this thesis.

2.1. INTRODUCTION

The Space Surveillance Network (SSN) is responsible for tracking over 18000 objects in the satellite catalog (SATCAT) [2]. Its measurements are used for generating Two-Line Elements (TLEs) and Tracking and Impact Predictions (TIPs). These products are often the only available source for many Space Situational Awareness (SSA) activities, such as conjunction analyses and re-entry predictions. The SSN is the largest network of its kind and consists of optical and radar sensors. The sensors contribute in various degrees, and are classified as either dedicated, collateral or contributing. Most sensors are located on the north-western hemisphere. The new Space Fence System (SFS), with two sites in the Pacific Ocean and Australia, promises improved network geometry and detection capabilities.

To properly assess the current and future configurations of the SSN, the technical capabilities, coverage, roles, and location of individual sensors must be taken into account. Previous surveys of the SSN are a good starting point, but either lack completeness in these aspects or are outdated [10, 28–31].

This chapter presents a survey of the most important sensors, focusing on sensor type, role, coverage, and capabilities. The current network geometry is simulated. A methodology for generating and editing observations will be presented.

For this study the tracking of rocket bodies in low-Earth orbit (LEO) is considered. The focus is on phased-array radars (PARs), as they are primarily used for this purpose. TLEs are estimated from these simulated observations for a test rocket body. The sensitivity of the solutions to several orbital and orbit determination (OD) parameters is investigated. Finally, through the addition of two new sensors, the future network geometry is assessed.

The chapter is outlined as follows. First, the SSN is described in Sec. 2.2. Section 2.3 presents an overview of the simulation set-up. The results are presented and discussed in Sec. 2.4. Finally, conclusions and recommendations are given in Sec. 2.5.

2.2. SPACE SURVEILLANCE NETWORK

The United States Air Force Space Command Space Surveillance Network (US AFSPC SSN) is the largest governmental network. The network was initially developed as a missile-warning network [10]. The network consists of plain radar, optical, and PAR sensors, and can be grouped into dedicated, collateral, and contributing sensors. Dedicated sensors have space surveillance as a primary mission. Collateral sensors are connected directly to the Space Surveillance Center (SSC). These sensors still have primary (or even secondary) missions other than space surveillance. In the case of PARs, usually a dedicated sub-array of elements (also fence) is operated for the detection and tracking of objects. This fence covers only a portion of the total coverage and duty cycle, in parallel to the primary mission. Finally, contributing sensors provide space surveillance only upon request from the Joint Space Operations Center (JSpOC). The following examples give a rough idea of how much these sensors contribute [30]: the Millstone rader contributes 80 hours per week and the Haystack radar about one week every six. All four mechanical radars at Kwajalein contributed a total of 138 hours in 2014. Some sensors

[2] https://www.celestrak.com/satcat/boxscore.asp, retrieved: April 3, 2017

Table 2.1: Overview of PARs sensors in the SSN. The sensor role (R) is either dedicated (D) or collateral (C). The azimuth and elevation of the boresight of the radar face is indicated in degrees. Radar model is AN/FPS-132, unless noted otherwise. Location is USA unless noted otherwise.

Name / location	R	Lat [°]	Lon [°]	Alt [m]	Boresight [°]
Eglin[c]	D	30.572	−86.215	36	180x45
Clear[a]	C	64.300	−149.191	175	6,244x20
Fylingdales, GBR	C	54.362	−0.670	258	5,125,245x20
Thule, GRL	C	76.569	−68.299	424	117,357x20
Beale	C	39.136	−121.351	117	186,246x20
Cape Cod[a]	C	41.752	−70.538	67	47,167x20
Cobra Dane[e], Shemya	C	52.737	174.092	68	319x20
PARCS[f], Cavalier	C	48.725	−97.900	344	8x25
SFS1[b], Kwajalein Atol	D	8.723	167.719	7	0x90
SFS2[b], Exmouth, AUS	D	−21.816	114.165	11	0x90

[a] The upgrades of the Clear and Cape Cod started in 2012 and 2013 and are to be fully certified in 2017 and 2018, respectively [32].

[b] Both are model AN/FSY-3. SFS1 will become operation in 2018, while SFS2 is expected to become operational in 2021 [33].

[c] AN/FPS-85, [d] AN/FPS-108, [e] AN/FPQ-16

are only used exclusively for certain purposes, such as to track launches.

The two radar types currently used in the SSN are mechanical and PARs. Previously, the SSN also included a multi-static radar system (more details below). PARs consist of flat faces containing several thousands of antenna elements. Compared to mechanical radars, PARs use electronic steering by shifting the phase of incoming signals. Due to this, PARs can track numerous targets simultaneously and are suitable for detection [30]. PARs have a limited coverage (if less then three faces are used), narrowing beamwidth away from the face normal, lower operating frequencies, and higher cost.

In the past Several authors have consolidated space-surveillance sensors [10, 28, 30, 31]. Although they provide valuable information, none prove to be a complete and sufficient source for simulating the SSN. The SSN is rapidly changing, so even information a few years old can already be outdated. For example, the Air Force Space Surveillance System (AFSSS) and the Moron Optical Space Surveillance (MOSS) telescope were both closed in 2013, the Antigua radar was relocated to Australia in 2015, and the Ascension radar has become a dedicated sensor. Moreover, a categorisation into dedicated, collateral, and contributing sensors is important. Sensor limitations, such as coverage and range, have a large impact on the simulated observations. Lastly, instrument accuracy, observation rate, tasking, and scheduling should ideally all be taken into account.

The AFSSS formed a major asset for the radar surveillance for LEO satellites. Also known as the space fence, the AFSSS consisted of three continuous transmitter and six receiver stations at 33° latitude, spanning approximately 70° in longitude across the US. The fence was closed in August 2013. Construction of the AN/FSY-3 Space Fence System (SFS) began in 2014. SFS will consist of two sites and use S-band radar (2 GHz to 4 GHz). Traditional PARs operate at around 400 MHz, with the exception of Cobra Dane which has a nominal frequency of 1275 MHz [34]. The first and largest site is located on Kwajalein Atoll in the Pacific Ocean and is expected to be operational in 2018. The second and smaller site is located in Western Australia and is expected to be operational in 2021 [33] [3].The new fence will have a higher accuracy and detection capabilities than current sensors, potentially increasing the number of tracked objects to more than 100 000 [35].

An updated inventory of all SSN sensors is made, including all mechanical radars and optical stations. The closing, relocation, and upgrades of sensors are taken into account. The current role of each sensor is investigated, as well as a preliminary investigation into sensor accuracy. Tab. 2.1 shows a selection of this survey for PARs.

The table reports the azimuth and elevation of the normal of the radar faces (i.e., boresight). The horizontal field of view (FOV) is generally reported to be 120° (thus a full 360° for three faces). For faces with a tilt of 20°, the resulting maximum elevation differs amongst sources, most report either 80° or 85° of maximum elevation. The latter value suggests a vertical FOV of 130°. However, it is assumed that the FOV of all PAR systems is 120° in horizontal and vertical direction per face, as they are roughly square. An exception is SFS, which receiving antenna array is more rectangular and spread in longitudinal direction, for this sensor a FOV of 40° is assumed for the latitudinal direction. The loc-

[3] The main location on Kwajalein Atoll was declared operation in 2020. Near-term funding for the second site in Australia is still uncertain. Current status retrieved from: https://breakingdefense.com/2021/08/near-term-funds-for-second-space-fence-radar-uncertain/, accessed: December 17, 2022.

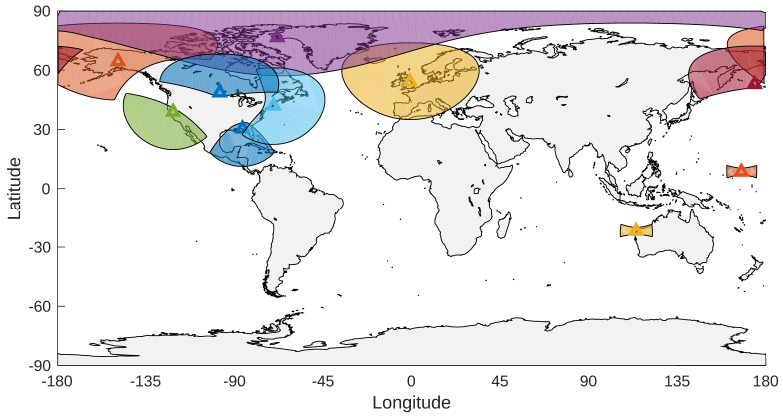

Figure 2.1: Space Surveillance network coverage for an object in a circular 600 km orbit.

ation of SFS1 was estimated from satellite images of the construction site. The location of SFS2 is unknown, but is assumed to be at the Naval Communication Station Harold E. Holt in Exmouth, Western Australia, although this is not confirmed.

The contract for the construction of a new AN/FPS-132 early-warning radar in Qatar was awarded to Raytheon and is expected to be completed in 2021 [36]. Its exact location, number of faces, and possible role in the SSN is not known.

2.3. SIMULATION SET-UP

The SSN is simulated for LEO. First, the configuration of the network is explained. Second, the test object is introduced, including a sampling strategy to randomise the orbits. Third, the set up of the orbit propagator is given. Fourth, the process of simulating observations is detailed. Finally, the orbit determination is explained.

2.3.1. NETWORK CONFIGURATION

The coverage is dependent on the orbit of an object. Due to the FOV, the coverage grows with the range, resulting in longer observation arcs. A coverage map is generated for a test object in a 600 km orbit. The azimuth, elevation, and range is calculated of the test object with respect to each station using the WGS84 reference ellipsoid [4] and coordinates from Tab. 2.1. The observation vectors are then transformed to the local observation plane, as determined by the boresight of each face. Only observations within the FOV are kept.

Fig. 2.1 shows the location and coverage of the dedicated and collateral PARs for a test object in a circular orbit of 600 km. The elevation and azimuth limitations of each sensor have been taken into account. Single-, double-, and triple-face PARs are easily distinguished. The primary mission of many of these sensors is providing ballistic missile warnings, which is obvious from the outward facing coverage of the stations along the US border. The footprint of the two SFS sensors seems small in comparison to the

[4] http://earth-info.nga.mil/GandG/wgs84/index.html, accessed: April 7, 2017

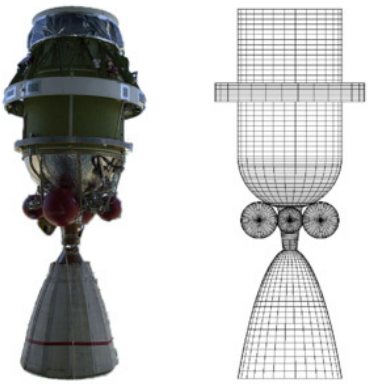

Figure 2.2: True and modelled Delta-K rocket body [37].

other sensors. This is due to projecting the (mostly) vertical coverage on the horizontal plane, reduced latitudinal coverage, and choice of map projection (i.e., a tendency to exaggerate sizes at higher latitudes).

The figure also shows how most PARs are located in North America and northern Europe. In this configuration, the southern and eastern hemisphere are underrepresented. The two SFS sensors will improve geographic coverage.

2.3.2. TEST OBJECT

The Delta-K rocket body is selected as the test object. The object has frequently re-entered and fragments have been previously recovered due to its high-temperature resistant components. The Delta-K was also subject for the 6 degree-of-freedom (6DOF) re-entry simulator in [37]. As the aerodynamic model and databases for the Delta-K were already derived, a 6DOF propagation of the test object is performed. Fig. 2.2 shows the true and modelled Delta-K rocket body.

A nominal state has been derived from 33 re-entered Delta-Ks in the period of 2004 to 2017. For each object the orbital state 30 days prior to re-entry is taken. The variations in semi-major axis, eccentricity, and inclination are shown in Fig. 2.3. A strong correlation between semi-major axis and eccentricity can be observed, related to the circularisation of the orbit due to the aerodynamic drag. Moreover, the objects have either a low or high inclination, depending on the target orbits in which these rockets were launched (i.e., GTO or LEO, respectively). The groups are indicated by the different markers, where the legend indicates the mean and standard deviation of the inclinations found in each group.

Random initial states are sampled from each group equally. The eccentricity is sampled uniformly within the observed bounds. The semi-major axis is obtained through a linear correlation with the eccentricity. Finally, the inclination is sampled from a normal distribution. The right-ascension of the ascending node and argument of perigee are assumed to be uniformly distributed between 0 and 360°, and the initial true anomaly is zero. The initial aerodynamic angles are assumed to be zero, while the rotational rate is

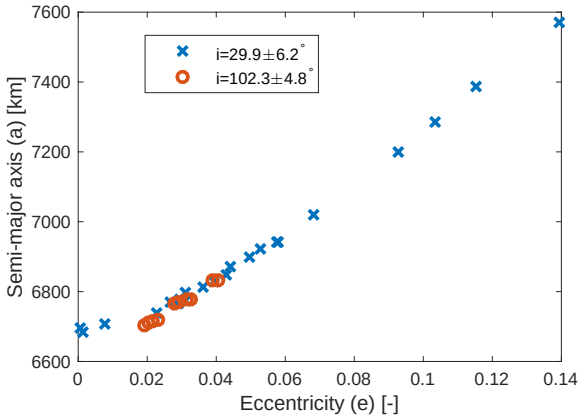

Figure 2.3: Semi-major axis versus eccentricity grouped by inclination of 33 Delta-K rocket bodies.

taken as one revolution per minute about the pitch axis. Finally, variations in the atmospheric density are modelled using a log-normal distribution with parameters $\mu^\star = 1.0$ and $\sigma^\star = 0.12$ [37].

2.3.3. ORBIT PROPAGATION

Observations are generated from numerically propagated orbits for the varying initial conditions. As mentioned previously, both the translational state and rotational state of the object is propagated. The equations of motion are integrated using a Runge-Kutta-Fehlberg 4(5) variable step-size integrator. The tolerance is set to $\epsilon_{rel} = \epsilon_{abs} = 1 \times 10^{-8}$. The step-size is allowed to vary between a minimum and maximum value of 1×10^{-4} and 1×10^{3} s, respectively. The EGM2008 gravity field model is used up to order and degree 5 [5].The atmospheric density is modelled using the NRLMSISE-00 model [38]. These settings provided a good trade-off between accuracy and computational efficiency.

2.3.4. OBSERVATIONS

Realistically, observations are limited by a number of technical and physical constraints, and are subject to numerous error sources. Not properly taking these into account would lead to too many and too idealistic observations. Accurate modelling of individual sensor capabilities, and scheduling is difficult based on the available information, and therefore considered beyond the scope of the current work. The main focus is on modelling the network geometry and coverage.

The observation conditions are taken into account for each sensor, as previously explained in Sec. 2.3.1. An elevation cut-off of 5° is used for all sensors. A measurement rate of 0.1 Hz has been chosen. The measurements are further edited to account for sensor availability, viewing conditions, and other limitations. To introduce a stochastic component in the amount of measurements, probabilities are introduced to discard meas-

[5] http://earth-info.nga.mil/GandG/wgs84/gravitymod/egm2008/egm08_wgs84.html, retrieved: April 7, 2017.

urements and passes. These probabilities are chosen by judgement of the author.An individual observation has a 20 % chance of being rejected, while the probability for discarding an entire pass is 25 % for collateral sensors only.

Measurement noise is simulated to account for sensor capabilities and atmospheric disturbances. The noise is assumed to be unbiased Gaussian noise, with a standard deviation of 1 km in radial direction and 0.1° (1 km at $r = 600$ km) in azimuth and elevation.

2.3.5. ORBIT DETERMINATION

The observations are used to fit TLEs using the Simplified General Perturbations (SGP4) model [39]. Range, azimuth and elevation measurements are generated for each Monte-Carlo (MC) sample for three consecutive days. The fit span consists of the first two days of observations. These are in the form of range, azimuth, and elevation, which are edited and used for orbit fitting. The test span consists of the third and final day and provides unedited observations in inertial Cartesian coordinates, which are used for studying the propagation accuracy of the solution.

2.4. RESULTS

The orbit determination is performed for 1000 randomly initialised orbits. The mean, median, and standard deviation of the fit and test span are collected for each sample.

On average, the object is observed by 4.8 stations over two days, resulting in 1560 observations. The mean fit residual is 1.7 km, while the residuals for test period are on average 5.8 km. The large error growth in the test period is due to the low orbit and resulting atmospheric drag, and in line with actual results for one-day predictions of TLEs [27].

2.4.1. SENSITIVITY

The rank correlation between the median residual and a number of parameters is computed to obtain the sensitivity of the solution. Fig. 2.4 shows the result for the fit and test span for 5 parameters: eccentricity, inclination, density, number of stations, and number of observations, respectively. The results between the fit and test span are very similar. The correlations are slightly larger for the test span, which are enhanced through propagation and the resulting error growth.

The residuals are negatively correlated with the eccentricity and number of observations. Near-circular orbits are more difficult to estimate due to sensitivity of the argument of perigee near its singularity. The reduction of the residuals with the number of observations is obvious. However, there is a strong positive correlation with the number of stations. It is found that the spread of solutions increases significantly with multiple stations. Some solutions are improved, while other are worsened. Improved performance can be achieved by only including observations from sensors, if the fit is improved.

Inside each inclination group the variation has little effect on the solution quality. However, there is a small difference between the two groups, which will be discussed next.

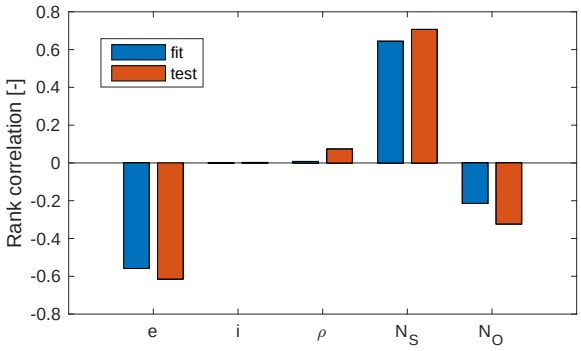

Figure 2.4: Sensitivity of orbit fit and propagation (test interval) to the eccentricity e, inclination i, density ρ, number of stations N_s, and number of observations N_o.

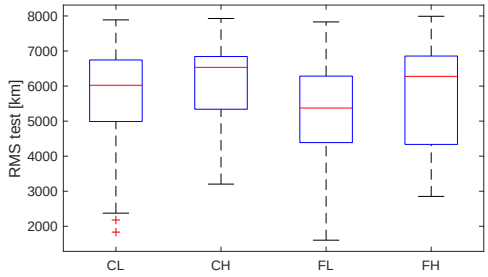

Figure 2.5: Boxplot of the propagated residuals for one day for the current and future network configuration (C and F, respectively) and the low- and high-inclined orbits (L and H, respectively).

2.4.2. SPACE FENCE

Fig. 2.5 shows the residuals of the test span for the two inclination groups (L and H, indicating the lower and higher inclinations, respectively) and two observation scenarios (C and F indicating the current and future scenarios, respectively).

It can be seen that the lower-inclined group has a slightly higher accuracy, but larger spread. The difference is attributed to the larger spread in eccentricity for the lower-inclined group. The additional sensors have a positive effect on the orbit solutions. The mean of the lower-inclined objects is reduced with 650 m, while the higher-inclined mean is reduced by 257 m. The larger difference for the low-inclined group is due to the location of the new sensors closer to the equator.

More detailed modelling of these sensors will likely improve these results further, as the SFS is expected to be more accurate than other PARs [33]. The spread of the solutions is higher, especially for the higher-inclined objects, which is due to the small number of observations resulting from short passes registered by the SFS sensors. The passes are shorter than for traditional PARs due to the vertical boresight and narrow latitudinal width of the fence. For a near-polar orbit the pass duration is only several minutes.

2.5. CONCLUSIONS

The SSN is continuously changing. New sensors are added, as existing ones are relocated, upgraded, or closed. Moreover, the participation of sensors can change over time. An overview of the current configuration was presented for PARs, including the planned SFS. The coverage of each sensor was investigated. Observations for a Delta-K rocket-body reference object were generated for a randomly initialised orbit with varying eccentricity, inclination, and atmospheric density. From the observations the TLEs were estimated.

The residuals of both the fit and test span are highly sensitive to the eccentricity, number of observations, and number of sensors, while the inclination has minor influence.

The two additional SFS sensors provide a reduction of the median error in the solutions, especially for low-inclined orbits. However, due to the shorter observation arcs, the spread in solution quality is increased.

The study only took the network geometry into account. Further improvements can be made by simulating the accuracy of individual sensors to a higher degree. The capabilities are found to differ greatly across sensors. Specifically, the SFS promise a significant improvement in performance over traditional PARs. So the observed benefits are likely very conservative and much higher in reality. However, more details on the sensors are required, and these are often not available.

3

TLE Uncertainty Estimation using Robust Weighted Differencing

Geul, J., Mooij, E. and Noomen, R.

Published [1] in Advances in Space Research, Vol. 59, No. 10, pp. 2522–2535, 2017

Accurate knowledge of satellite orbit errors is essential for many types of analyses. Unfortunately, for two-line elements (TLEs) this is not available. This thesis presents a weighted differencing method using robust least-squares regression for estimating many important error characteristics. The method is applied to both classic and enhanced TLEs, compared to previous implementations, and validated using Global Positioning System (GPS) solutions for the GOCE satellite in Low-Earth Orbit (LEO), prior to its re-entry. The method is found to be more accurate than previous TLE differencing efforts in estimating initial uncertainty, as well as error growth. The method also proves more reliable and requires no data filtering (such as outlier removal). Sensitivity analysis shows a strong relationship between argument of latitude and covariance (standard deviations and correlations), which the method is able to approximate. Overall, the method proves accurate, computationally fast, and robust, and is applicable to any object in the satellite catalog (SATCAT).

3.1. Introduction

The covariance describing the accuracy of a satellite state is an important input for exercises, such as conjunction analysis and re-entry predictions, which are increasingly important for operating in today's space environment. Through error propagation the probability of potential collisions can be calculated and a spread of impact locations

[1] Minor modifications have been made for this thesis.

and times anticipated. These efforts help significantly in managing and mitigating the problem of space debris. As the population of objects in space increases, so does the need to improve the knowledge of their states and associated uncertainty.

Two-line elements (TLEs) present the most comprehensive and up-to-date source of Earth-orbiting objects and are key in many monitoring and analysis activities. Despite their importance, they suffer from major drawbacks: they have limited accuracy, are mistagged, miss manoeuvres, and perhaps most importantly, lack covariance information. Although the TLEs are publicly available, their input observations and/or fit residuals are not.

TLE differencing, amongst other methods, aims to estimate the missing covariance information by propagating TLEs (using the Simplified General Perturbations 4 (SGP4) model) to a common time and comparing them. This method presents a simple, robust and fast way of obtaining an uncertainty estimate. Although this method has been described in literature [40–43], its implementation differs greatly, and, moreover, there is a lack of validation for important orbital regimes and little investigation into the sensitivity to the parameters involved.

This thesis aims to present an extension of the general differencing method, offering improvements to increase its accuracy and robustness. Moreover, the method is demonstrated to work for both classic and enhanced TLEs and is validated for the GOCE satellite using Global Positioning System (GPS) data during its final phase (no orbit control) before re-entry. The demanding environment presented by the very low-Earth orbit (LEO), combined knowledge about GOCE and an increased availability of TLEs make GOCE very interesting for this study.

The chapter is structured as follows. First, the current state of differencing techniques is presented in Section 3.2, followed by the proposed methodology in Section 3.3. Next, Section 3.4 details the analysis. In Section 3.5, the results and validation of the method are presented and discussed. Lastly, the conclusions are given in Section 3.6.

3.2. BACKGROUND

The lack of uncertainty information of TLEs has initiated numerous studies into the accuracy of TLEs, methods for estimating their covariance, and improvements to their accuracy [21]. There is a wide range of methods that allow the uncertainty information to be estimated. These approaches differ greatly in difficulty, accuracy and applicability. However, two classes can be distinguished: methods using only TLEs and methods relying on additional data. Methods relying on external data, such as observations or precise ephemeris (e.g., derived from satellite laser ranging (SLR) or GPS), are not further considered. Unfortunately, such data are not available for the far majority of objects. Moreover, uncertainties derived for a few objects are hard to extrapolate across the population or time, due to their dependency on, amongst others, satellite properties (shape, size, etc.), orbit type (semi-major axis, eccentricity, inclination, etc.), variability of the environment (solar, magnetic flux, etc.), configuration of the Space Surveillance Network (SSN), and the models and determination routines of TLEs.

Changes to SGP4 and how TLEs are estimated have not been made public since the official release of the “Spacetrack Report #3” in 1980, leaving users guessing to the current implementation of SGP4. Since 2013 the way TLEs are generated has changed sig-

nificantly for many objects. TLEs are now fit to pseudo-observations generated from extrapolated higher-order orbital-theory solutions [26], as opposed to observations from the SSN directly. These new TLEs (referred to as enhanced TLEs) are found to differ significantly in terms of errors and behaviour compared to old TLEs (from hereon classic TLEs), as will be demonstrated in Section 3.5. A more obvious distinction between these two types is the argument of latitude (AOL) associated with their state at the TLE epoch. The AOL of classic TLEs is around zero degrees (i.e. at the ascending node) and around 90 degrees for enhanced TLEs.

TLE differencing and TLE fitting only use the TLE data and are thus applicable to any object for any epoch. The former technique propagates TLEs to a common epoch and compares them, while the latter technique treats TLEs as pseudo-observations from which an orbit is estimated, usually using a higher-fidelity special-perturbation (SP) model [44–47]. The benefits of TLE fitting are that an (improved) initial estimate as well as uncertainty information is obtained, which is convenient when further propagation is done using other models than SGP4. Furthermore, it has been demonstrated that both the initial error and error growth of TLE-derived states is significantly reduced compared to original TLE states [44].

TLE differencing methods, on the other hand, are much simpler and faster: they only rely on SGP4 and require no external models and orbit-determination routines. Moreover, with the improved accuracy and propagation stability of enhanced TLEs the need for different propagation methods is reduced. In Ref [40] a covariance generation (COVGEN) approach by differencing multiple preceding TLEs with the most forward one is recommended. In Ref [41] backward propagation is included and mentions several significant features of the errors: a temporal and error bias is noted, as well as an asymmetry of the error in time.

The temporal bias is the shift of the epoch of minimum error, while temporal asymmetry refers to a difference in error growth between forward and backward propagation.

This bias was also demonstrated in Ref [48] (for the CHAMP and GRACE satellites using GPS solutions), showing a clear dependency on the solar cycle and orbital altitude. In Ref [42] a detailed analysis of pairwise differencing and autocorrelation is presented, while in Ref [49] the results against GPS solutions for the Stella satellite (near-circular 800km orbit) is compared. In Ref [50] the COVGEN approach is assessed using TLEs for GPS satellites, which are compared against their known ephemerides. COVGEN provides a good match in overall characteristics, but is insensitive to differences between forward and backward error growth, which is noted in the work. In Refs. [43, 51] the work in Ref [41] is extended, approximating the distribution as a Gaussian mixture. The critical nature of outlier removal is mentioned for data generation and sensitivity of the uncertainty to the AOL. In Ref [27] an analysis for many orbit regimes is presented and it is identified that especially near-circular very low orbits ($h_p = 200 - 300$ km, $e = 0.00 - 0.02$) pose a major challenge, due to the importance of drag. Table 3.1 presents a small subset of the results found during that study, which demonstrates the difficulty of the aforementioned regime. Unfortunately, this regime is critical for (human) spaceflight and re-entering objects.

Despite almost two decades of investigation into TLE-differencing methods, several issues remain. A major problem is that the exact implementation of the differencing al-

h_p [km]	e [-]		
	$0-0.02$	$0.02-0.2$	$0.2-0.7$
$200-300$	30.0	5.4	6.0
$300-400$	3.5	2.8	4.8
$400-500$	2.4	1.2	4.3
$500-600$	1.0	0.6	3.6

Table 3.1: Position errors in kilometres for one-day predictions as function of perigee height (h_p) and eccentricity (e) identified in Ref [27].

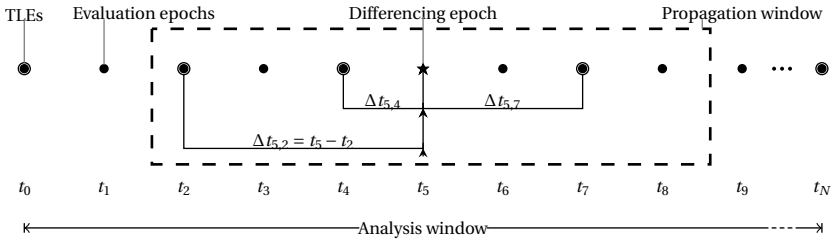

Figure 3.1: Schematic overview of TLE differencing method.

gorithms differs greatly, often without proper justification and comparison against previous implementations. The choice of analysis epoch(s) and the analysis/propagation window are often not properly justified. Moreover, the implementations have been documented using varying detail, making it hard to reproduce results in many cases. Another major shortcoming is the scarcity of validation studies. Especially, the absence of validation for LEO is worrisome, considering its previously mentioned importance and difficulty. Moreover, most implementations only consider forward propagation to a single TLE epoch and do not consider the temporal bias. Furthermore, most studies consider a single TLE (at zero epoch) as reference, but especially the presence of a temporal bias sheds doubt on this practice. Lastly, it has not been investigated how this method is impacted by enhanced TLEs.

3.3. METHODOLOGY

Differencing methods generally propagate states to a common epoch and compare them to derive error samples. These methods are unique, as they only use TLE data and the SGP4 model. By solely relying on publicly available data this method is applicable to any (non-classified) object in the satellite catalog (SATCAT).

Figure 3.1 shows a schematic overview of the differencing process. Commonly a certain number of TLEs within a certain time period are considered at one time (TLEs at t_2, t_4 and t_7 in the example), which is determined by the propagation window (dashed line). The choice of propagation window is discussed in Section 3.3.3. Within this window the TLEs are propagated to a common differencing epoch (usually another TLE). In pairwise differencing, error samples are then obtained by creating pairs of TLEs at the

differencing epoch. The following illustrates this:

$$\epsilon = x_n - x_m \tag{3.1}$$

where ϵ is the error sample created by differencing TLEs n and m, and x is an arbitrary state variable or vector of variables (discussed in Section 3.3.1). Note that n could be any TLE, but often represents the TLE at epoch (not propagated). If n is the TLE at epoch and paired with many m, n is considered the reference state. This assumption will be discussed in more detail in Section 3.3.2. Similarly, m usually represents any of the propagated TLEs.

TLEs can be propagated both forward and backward in time (see Section 3.3.4). In the example the propagation window is symmetric about the differencing epoch (e.g., equal maximum forward and backward propagation time).

To create many error samples, multiple differencing epochs are considered, for instance epochs $t_0, t_1, \ldots, t_N$ as depicted in Figure 3.1. As mentioned before, a common choice is to have the differencing epochs coincide with the TLE epochs. However, all possibilities will be explored in Section 3.3.6.

Next to the value of the ϵ itself, the propagation time is another important property of the error to consider. Throughout the thesis this is referred to as the propagation time or age of the example.

The process is illustrated in Figure 3.1 and will be explained in further detail in the coming sections.

3.3.1. REFERENCE FRAME

The reference frame for comparison is the RSW frame, composed of the radial, along-track and cross-track directions. The RSW frame is a local frame and intuitive for astrodynamics applications. In this frame, the difference in position and velocity are computed.

It is important to consider that RSW is a local frame, as the transformation between the Earth-centered inertial and RSW-frame depends on the inertial state itself. Equation (3.1) can be rewritten to

$$\epsilon_{RSW} = \mathbb{T}(x_t)x_n - \mathbb{T}(x_t)x_m \tag{3.2}$$

where $\mathbb{T}(x_t)$ is the transformation matrix between the inertial and RSW frame, which is a function of the inertial state x_t. x_t can be any state (either n, m, or some other state), but it needs to be the same for both matrices in Equation (3.2). It is intuitive to choose the TLE with highest (expected) accuracy, but, considering the temporal bias, it might not be as straightforward as choosing the nearest TLE.

3.3.2. MINIMUM ERROR AND REFERENCE

The consideration of the reference state in differencing is difficult, but important. The choice of the reference state influences the results of the method: directly (the state x_n) and indirectly (through the transformation matrix x_t). Previous studies consider the TLE at epoch to be the reference. This can be generalised to: the TLE that is closest to the epoch of interest is considered as reference. Although this is perhaps an intuitive

strategy, it is not always the best. In Ref [41] it is already demonstrated that the epoch of minimum error does not coincide with the TLE epoch (i.e., there is a temporal bias $\Delta t^\star$).

Typical values for $\Delta t^\star$ are in the order of 4-5 hours for orbital altitudes of 200−300 km (as will be demonstrated) and 1.5-2.5 days for 400 − 500 km [48]. Considering the similar or higher update frequency of TLEs, this can have a significant affect on any type of analysis.

A proper consideration of a reference epoch must thus account for this effect. It is proposed that the reference state is derived as the weighted mean of multiple states simultaneously. This method is named weighted differencing (WD) as opposed to pairwise differencing (PD). Further, an inversly-quadratic relation of the weights with the time since the epoch of minimum error is proposed.

$$w_i = \frac{1}{(t_i^\star - t_{0_i} - t)^2} \tag{3.3}$$

$$\bar{w}_i = \frac{w_i}{\sum\limits_{i \in P} w_i} \tag{3.4}$$

where $\bar{w}_i$ is the normalised weight of TLE$_i$, $t_i^\star$ is the epoch of minimum error (which is unknown), t_{0_i} the epoch of the ith TLE, and t the propagation time since t_{0_i}. The weights are normalised, such that the sum of all weights equals one for evaluation at each single epoch. The set P contains all TLEs under consideration, represented by the propagation window in Figure 3.1.

As the epoch of minimum error of each individual TLE is unknown, it is assumed that all TLEs share the same offset (or shift), such that:

$$\Delta t_i^\star = t_i^\star - t_{0_i} \approx \Delta t^\star \, \forall \, i \tag{3.5}$$

Due to this simplification Equation 3.3 becomes:

$$w_i = \frac{1}{(\Delta_t^\star - t)^2} \tag{3.6}$$

The value of $\Delta t^\star$ is dependent mostly on the orbit determination process (fit length, etc.), which differs across orbital regimes and space-weather conditions [48]. It is expected that the assumption is valid within the analysis window.

The reference state and $\Delta t^\star$ are mutually dependent: $\Delta t^\star$ determines the weights and in turn the reference state, from which error samples are computed, which determine $\Delta t^\star$. This problem has to be solved iteratively. The initial guess $\Delta t^\star = 0$ is proposed as a starting point. The level of convergence for $\Delta t^\star$ determines the accuracy of the method. A converging solution was obtained in all cases. Moreover, solutions were found to converge within three iterations to below a relative tolerance of $\epsilon < 0.01$, which is the criterion used throughout this study.

The weighted reference state can be found using:

$$x_{ref} = \sum_{i \in P} \bar{w}_i x_i \tag{3.7}$$

where P includes *all* states within the current propagation window. The weighted reference state is then used as reference in the generation of both the samples and transformation matrices ($x_t = x_n = x_{ref}$), such that Equation (3.2) becomes:

$$\epsilon_{RSW} = \mathbb{T}(x_{ref})x_{ref} - \mathbb{T}(x_{ref})x_m \tag{3.8}$$

3.3.3. ANALYSIS AND PROPAGATION WINDOW

The analysis window, as depicted in Figure 3.1, is the period from which the statistical properties are determined. The size of the window presents a trade-off. On one hand, the window should be large enough to allow for enough data for statistical significance, while on the other hand, it should be small enough to minimise the influence of longer-term effects, such as changes due to space weather (solar cycle) and orbit degradation.

The propagation window is a moving window within the analysis window. The differencing epoch resides within it. All TLEs that lie within the propagation window are propagated to the differencing epoch and compared. The size of the propagation window again presents a trade-off, depending on the application and object under consideration. For instance, for LEO objects a much shorter propagation window should be considered than for spacecraft at higher altitudes. Also the size of the propagation window can be influenced by manoeuvres. In previous studies windows up to 40 days have been considered. For very low-Earth orbits that are heavily influenced by atmospheric drag, the window could be as short as 4 days.

3.3.4. FORWARD/BACKWARD PROPAGATION

If the differencing epoch coincides with the upper bound of the propagation window, all considered TLEs precede the epoch, resulting in only forward propagation.

In general, both forward and backward propagation should be used. Forward propagation paints only half of the uncertainty picture. In Ref [50] this is rightfully noted in the assessment of the COVGEN method. Nonetheless, many previous studies have not looked at backward propagation. Not including both directions wrongly assumes a temporal symmetry (lack of bias and equal growth) of the error. This is false, as the epoch of minimum error does not coincide with the TLE epoch and the rate of error growth can differ significantly between backward and forward direction. It is therefore recommended to choose the differencing epoch at the centre of the propagation window.

3.3.5. MODELLING ERROR GROWTH

Regression, rather than data binning, is proposed for the estimation of the error growth from the samples. In previous studies binning was used. In binning, samples are collected based on their propagation time. The mean of the bin is then computed. The size of the bins is dependent on the number of samples and propagation-window size. Binning assumes no a-priori shape of the error-growth pattern. Data binning, however, is not recommended for continuous problems, as it removes information from the problem. Moreover, the method is sensitive to the bin size and outliers. As will be shown, the shape of the error growth can be easily modelled, so non-parametric methods are not necessary at this point.

The most common fitting technique is least-squares regression, of which many variants exist. Essentially, a model is fit through the data and the sum of squared residuals is minimised. Unfortunately, least squares also suffer from outliers. Outlier removal can be employed to edit the data for fitting or binning. A common test uses the (dimensionless) studentized residual:

$$r_i = \frac{|\epsilon_i - \mu_\epsilon|}{\sigma_\epsilon} \tag{3.9}$$

where μ_ϵ and σ_ϵ are the mean and standard deviation of the error samples, respectively. A sample ϵ_i is discarded if the studentized residual is larger than a certain value r_{max} (discussed below). The mean μ_ϵ is included to account for any bias present. Note that μ_ϵ and σ_ϵ were determined using all data including the outliers. After eliminating the outliers, these properties need to re-evaluated and the data retested, until no further outliers are detected.

A typical value of r_{max} is between 3 and 6 for normal-distributed data. Moreover, the recommended value of r_{max} depends on how far away outliers are expected to lie from the valid data. Ideally, the value of r_{max} should become smaller for each subsequent outlier-removal iteration, as the furthest outliers are removed first. Overal, the determination of outliers is troublesome and is sensitive to the choice of r_{max}.

Instead a robust least squares (RLSQ) method is proposed that is able to handle data with outliers directly. RLSQ is a form of weighted least-squares (specifically: iteratively reweighted least squares), where the weights of the data depend on their residuals. The residuals are obtained from the fit and are not affected by a bias. Also this method is iterative, as the residuals determine the weight, the weight determines the fit, and the residuals result from the fit. The weighting scheme used is the bi-square weight function [52]:

$$v_i = \begin{cases} \left[1 - \left(\frac{\epsilon_i}{k}\right)^2\right]^2 & \text{for } |\epsilon_i| \leq k \\ 0 & \text{otherwise} \end{cases} \tag{3.10}$$

where v_i and ϵ_i are the weight and residual of sample i, respectively. The parameter k is commonly a function of the standard deviation of the data σ. For normal distributed errors $k = 4.685\sigma$ is recommended [52].

3.3.6. DIFFERENCING EPOCH

The choice of differencing epoch has a big influence on the resulting estimation of the uncertainty. Previously, mostly TLE epochs have been considered. This is an obvious choice, especially when considering the TLE state at epoch as reference. However, this strategy results in only a limited number of differencing epochs (as the TLEs within the analysis window are usually few). Especially, if the propagation window is also short, the number of TLEs for comparison will be small. Moreover, TLEs are usually periodic, meaning that there will be gaps in the error samples. Lastly, the choice of the TLE epoch as differencing epoch seems very arbitrary when considering the temporal bias.

Therefore, intermediate differencing epochs are generated, in the case of Figure 3.1 epochs t_1, t_3, t_5, t_6, t_7, t_9. The inclusion of intermediate differencing epochs will result in more samples and a more evenly spaced distribution of errors.

The choice and spacing of differencing epochs, however, should be made with care. In Ref [51] a dependence of the error on the AOL u is noted. As TLE states commonly share a similar AOL u_c, additional differencing epochs are conservatively chosen at this same AOL too, such that:

$$u_k = u_c + 2\pi k \tag{3.11}$$

where k is such that $t_0 < t_k < t_f$ and u_c is the common AOL of the TLEs within the analysis window $[t_0, t_f]$.

The effect of the choice of AOL will be demonstrated in Section 3.5.6. However, for now it is assumed that matching of the AOL to the (majority) of TLEs is the proper choice.

The differencing epoch t_k can be derived from the AOL u_k. However, here another issue arises with respect to the consideration of reference epoch and state. As the AOL is dependent on the state itself, many states propagated to the same epoch will slightly disagree on the exact AOL. Similarly, all TLEs within the propagation window propagated to have the exact same AOL, will slightly disagree about the current epoch t_i. Therefore, the true differencing epoch t_k is obtained as a weighted mean of all epochs t_i at the AOL u_k:

$$t_k = \sum_{i \in P} \bar{w}_i t_i \tag{3.12}$$

Practically, this results in the AOL becoming the independent variable for this exercise and time dependent. However, as the SGP4 propagator takes time steps as an argument, a simple bisection rootfinding scheme is employed to find $t_k = f(u_k)$.

The result of this is a series of differencing epochs, for a given analysis period and desired AOL. For a typical LEO satellite, this results in about 16 differencing epochs each day, as opposed to only 1-2 epochs per day without TLE propagation.

3.4. EXPERIMENTAL SET-UP

In this section the details of the analysis are discussed. First, the proposed object of interest is introduced, followed by the periods considered and windows chosen. Next, statistical techniques and metrics are discussed. Finally, the analysis cases are introduced.

3.4.1. OBJECT

For the analysis ESA's Gravity field and steady-state Ocean Circulation Explorer (GOCE) is considered. GOCE was a geodynamics and geodetic mission launched on 17 March 2009 and re-entered on 11 November 2013 [2]. This object is interesting for many reasons.

GOCE's orbit is unique: it was in a very low near-circular orbit of only $h_p = 227\,\text{km}$ and $e = 9 \times 10^{-4}$. Therefore, the orbit was heavily influenced by atmospheric and gravitational disturbances. The satellite achieves a "drag-free" orbit by counterbalancing the drag using electric propulsion. Even within the LEO regime, this orbit can be considered an extreme case, as illustrated by Table 3.1.

[2] http://www.esa.int/Our_Activities/Observing_the_Earth/GOCE/Facts_and_figures, accessed: August, 17, 2016

Second, precise orbits derived from GPS observations are widely available throughout the mission, against which the method can be validated.

Third, because of GOCE's high interest, it was tracked frequently during its mission. During the re-entry phase, the release frequency of TLEs even doubled from ~2 to ~4 per day.

3.4.2. ANALYSIS WINDOW

GOCE low altitude orbit was maintained using a continuous-thrust ion-propulsion system, enabling a "drag-free" operational mode. The decay of the satellite started when the Xenon fuel was depleted early in the morning of October, 21, 2013[3]. The TLEs of the decay phase to re-entry are analysed: from October, 21, 2013 to November, 11, 2013. The analysis window is thus 21 days. A moving propagation window of four days ($\pm 2d$) is assumed.

TLEs are propagated to the argument of latitude (AOL) corresponding to the TLE set, such that samples are created every orbit.

3.4.3. STATISTICAL TECHNIQUES

Different estimation techniques for the error growth are compared. The traditional binning technique is compared to regression techniques. Several regression models and techniques are used. Unfiltered and filtered data (with outliers removed) are used to highlight differences between regular and robust methods.

The binning method is used to group together TLEs of a similar propagation time. The propagation window is subdivided into 15 bins of 6.4 hours (or roughly 4 orbits). Polynomials are used as models of the errors and uncertainty:

$$p(\epsilon) = \sum_{n=0}^{k} c_n \epsilon^n \tag{3.13}$$

where k is the degree of the polynomial.

The errors in the RSW frame are modelled as a multi-variate (correlated) normal distribution (MVN). Moreover, even through propagation the errors are assumed to remain MVN within the propagation window considered. Such a distribution is fully defined by the covariance matrix. For very high levels of uncertainty (e.g., resulting from long propagation times), the errors tend to exhibit a banana shape distribution instead of a spheroid. It is therefore important to properly evaluate the validity of the MVN assumption.

Correlation matrices are reported instead of covariance matrices. Although covariances are often reported in literature and are a common format for analyses, it can be difficult to infer the strength of a dependency when the magnitudes and units of variances of the respective variables differ.

The joint distributions are also graphed, to fully assess the assumption of linearly-correlated multi-variate normal distributions. Margins will be plotted using Kernel density estimation, providing a continuous, but non-parametric model for distributions.

[3] https://directory.eoportal.org/web/eoportal/satellite-missions/g/goce, accessed: August 17, 2016

3.4.4. CASES

The analyses is divided into a number of test cases, to demonstrate/benchmark (various) aspects of the methods, provide validation, and analyse the sensitivity of the method. Each test case is represented by a separate subsection in Section 3.5. A brief overview of the different cases with a short description and rationale is given below.

1. Overview of data: general overview of the TLE data. Analysing frequency, count, and epochs of TLEs for the analysis window and dates prior. Providing insight into relationship between TLEs and AOLs.

2. Error growth and minimum error: demonstrating temporal bias/asymmetry of TLE error growth using the absolute position error. The error data are constructed from comparison with GPS states. These data are estimated, to benchmark different statistical techniques. Robust regression is compared to binning and traditional regression methods.

3. Error growth in RSW components: robust regression is applied to each of position and velocity components, to demonstrate a good fit for all components and different model orders necessary.

4. Weighted differencing: weighted differencing is compared against pairwise differencing in terms of accuracy using GPS data for both enhanced and classic TLEs. Several (sub)tests are performed. First, the initial uncertainty is estimated. Second, the error and uncertainty growth are estimated. Third, the temporal bias is estimated.

5. Correlations: next to the uncertainty of various components, the correlations between them are important. The correlations are estimated using the robust weighted differencing technique and compared with GPS. Together with Case 3, the covariance matrix is now fully defined.

6. Covariance sensitivity: the sensitivity of the covariance (standard deviations and correlations) to the AOL is investigated to gain insight into TLE uncertainty and the importance of the choice of differencing epoch.

3.5. RESULTS AND DISCUSSION

The results of the analysis for each of the different cases are presented in the following sections.

3.5.1. OVERVIEW OF DATA

The map in Figure 3.2 gives an overview of the TLEs as a function of latitude and longitude at the TLE epoch for a period of 42 days: 21 days for analysis and 21 days prior. The color of each marker corresponds to the date.

The bar plot shows the number of TLEs for each day, the bars simultaneously function as a colorbar, relating the color of the markers to the date. The begin of the analysis window is marked by the vertical blue line. Bars that are (partly) outlined in black indicate the portion of TLEs associated with the ascending node (latitude $\sim 0°$).

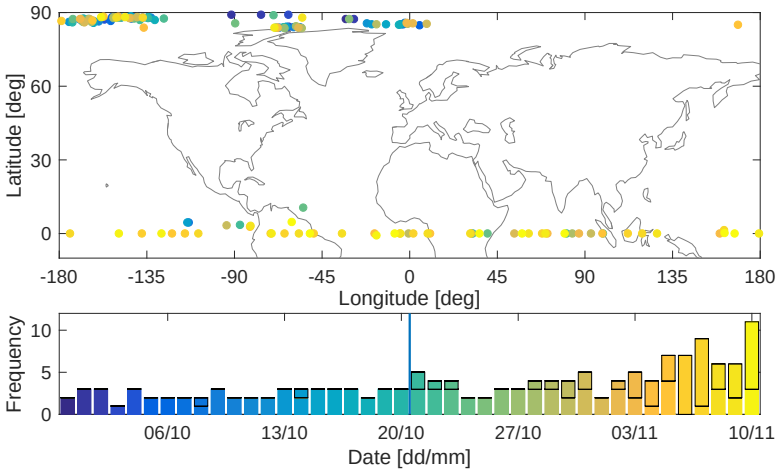

Figure 3.2: (top) Overview of TLEs as a function of longitude and latitude (top) and frequency of TLEs per day (bottom), where the portion of TLEs associated to an argument of latitude close to the equator are indicated by an outline of (part of the) bars.

The first thing to note is that the analysis window contains almost twice the number of TLEs (101 versus 52). Second, it can be seen that almost all TLEs prior to October, 21, 2013 have a high latitude ($\sim 90^\circ$), after which there is an equal mix of TLEs associated with $u \approx 0^\circ$ and $u \approx 90^\circ$ (50 versus 51, respectively).

As the number of TLEs is nearly doubled during the analyses window, compared to the reference window, and mixed in latitude, three assumptions are made. First, the additional TLEs are a result of additional tracking by Joint Space Operation Center (JSpOC) of GOCE during the re-entry phase. Second, this additional tracking results in TLEs with a distinct AOL. Third, the additional TLEs are of the classic type.

The latter suggests a mix of 50 classic TLEs and 51 enhanced TLEs for this period. This presents a unique opportunity to analyse these two types simultaneously for the same period.

3.5.2. ERROR GROWTH AND MINIMUM ERROR

The analysis of error growth provides a number of interesting insights: it can be used to demonstrate the presence of temporal bias and asymmetry, but also practically indicate when the TLE is on average the most accurate and, lastly, provide insight into the orbit determination process.

Figure 3.3 shows the position errors of propagated TLEs with respect to GPS solutions as a function of the propagation time as scattered data (blue markers). For this result only the enhanced TLEs (eTLE) are shown. It is remarkable that the minimum error is shifted ahead of the TLE epoch. The same analysis for classic TLEs (cTLEs) shows an opposite backward shift (as will be shown in Section 3.5.4), which is consistent with results from previous studies. This further confirms the difference between the two types.

The forward shift of the minimum (temporal bias) can be explained by the orbit-determination process of eTLEs, where future pseudo-observations are generated from

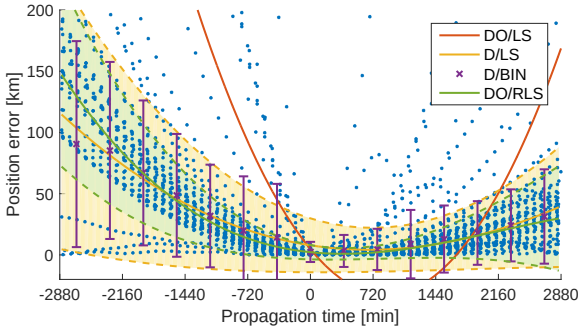

Figure 3.3: Benchmark of different methods for estimating the error and (3σ) uncertainty of the TLE propagation errors during the reference period. Methods shown include least squars (LS, robust LS (RLS) and binning (BIN). Two datasets were used, data with outliers removed (D) and all data, including the outliers (DO).

using SP orbit determination and propagation.

It can further be seen that the forward error grows much more gradual than backwards growth. This peculiar shape can also be explained by the fitting process. Like for cTLES, a quadratic error growth is expected. However, (part of) the pseudo-observations are derived from propagated states, which themselves are subject to error growth (due to limited predictive abilities). As a result the point of minimum error is actually shifted backwards (while remaining positive) from where one would expect it. This, perhaps counter-intuitively, results in a more gradual forward slope, as the error growth is a superposition of the uncertainty resulting from two separate sources.

The different estimation models are plotted as solid lines. A data/method naming scheme is used to differentiate the combinations. The data is split into data with outliers removed (D) (criterion $r_{max} = 3$) and data with outliers (DO). Therefore, methods starting with DO use unedited data. The methods used are (robust) least-squares regression (R)LS and data binning (BIN). The uncertainty bounds are also estimated using the different techniques and shown as the solid filled areas enclosed by dashed lines of the same color.

The DO/LS serves as a benchmark for other methods and clearly performs worst. Only the error fit is shown, the resulting uncertainty was not plotted as it would fill the entire window. Data binning without outliers (not shown), similarly performs badly. This confirms the importance of data filtering for this type of analysis, as noted in Ref [43].

Next, the two methods using filtered data D/LS and D/BIN provide comparable results. D/LS produces a more smooth result and shows better behavior at the boundaries. Not only does it produce a continuous solution, but the solution is also more smooth, whereas D/BIN commonly suffers from jumps between adjacent bins.

The effectiveness of the robust variant is demonstrated when comparing D/LS and DO/RLS. It is expected that with careful tuning the D/LS (D/BIN) results can be improved. However, this is undesirable as it is very sensitive and dependent on the data.

Note that the orbit under consideration is very demanding, especially during the orbit decay phase. Moreover, data outside the main band clearly forms streaks, which is due to a few bad TLE solutions. Another approach would therefore be to first identify

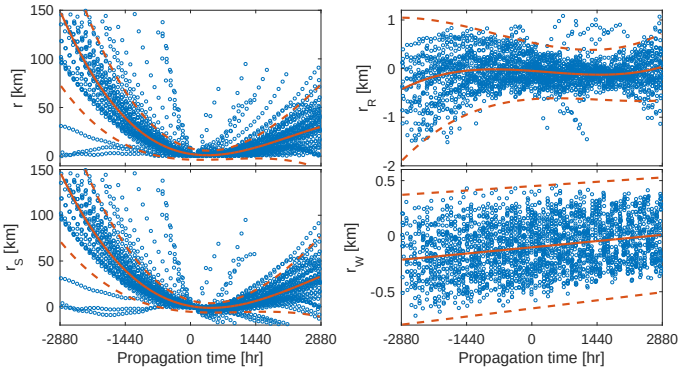

Figure 3.4: Robust regression of the position errors, as the mean and (3σ) uncertainty bounds on the total Euclidean error and as decomposed in the RSW frame.

and remove outlying TLEs. Doing so however, requires more statistical tests and tuning of parameters.

Overall, a number of observations stand out:

- a temporal bias shifts the epoch of maximum accuracy either forward or backward from the TLE epoch;
- the temporal asymmetry is much more pronounced for the enhanced TLEs, reducing the backward propagation stability significantly;
- the above effects are present in both classic and enhanced TLEs, but opposite/different in nature;
- robust least-squares regression using the polynomial models is able to capture the growth well, requiring no outlier removal of error samples and/or TLEs.

3.5.3. ERROR GROWTH OF RSW COMPONENTS

In the previous section the modelling of the absolute position error was investigated. Commonly, both the position and velocity error are analyzed in their radial, along-track and cross-track components. The absolute position and velocity errors are dominated by the along-track position and radial velocity error, respectively. Due to the strong linear relationship between these two components, the errors in these components and the absolute errors will be very comparable. Therefore, a good fit is expected for these components. However, the goodness of fit of the remaining components remains to be demonstrated.

Figures 3.4 and 3.5 show the results of the regression fit using the TLE errors with respect to the GPS reference states in all components.

It can be seen that the behavior is significantly different per component. The top-left plots show the absolute position and velocity, respectively.

The contributions by the along-track position (bottom left) and radial velocity (top right) are evident. Moreover, the similarity between these two and the absolute errors

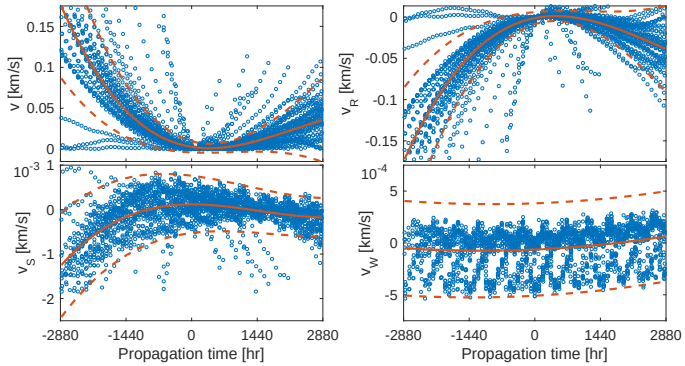

Figure 3.5: Robust regression of the velocity errors, as the mean and (3σ) uncertainty bounds on the total Euclidean velocity error and as decomposed in the RSW frame.

are evident. These components also show the strongest growth in error. Therefore, these component should receive the highest priority in assessing the performance of the method. There is great similarity between these two (their correlation is discussed later) and the total position error, so previous conclusions apply here too.

The radial position and along-track velocity errors are also comparable and show a complex curvature and a minimum uncertainty beyond the minimum total error. Although error growth is visible, it is not nearly as strong as for the previously discussed components.

The cross-track error of both position and velocity demonstrates a near-constant uncertainty and follow a simple mean trend (linear and quadratic, respectively). There is hardly any growth on this time scale.

It was assumed that the uncertainty bounds of the error are symmetric about the mean (e.g., equal distance of the lower and upper bound to the mean). It can be seen that this assumption is reasonable, except for the cross-track velocity error. The errors are clearly more concentrated above the mean. The exception is ignored due to the resulting overestimation of the upperbound and minor influence of this component on the overall error.

From these results it is obvious that the degree of the regression model of each component has to be carefully selected. As a general rule-of-thumb, the error uncertainty is modelled as an order less than the error trend. Table 3.2 gives an overview of the degree of the regression models used.

Note that a third-degree fit is enough to model all errors. It was found that for classic TLEs for some components the degree could be reduced further. However, this minimum degree was not further looked into.

Overall, the method is also able to accurately estimate the error and uncertainty growth of the individual RSW components. The following additional conclusions can be drawn:

- the error trend and growth are completely dominated by the along-track position and radial velocity components;

	Degree			Degree	
	Error	Residual		Error	Residual
r	3	2	v	3	2
r_R	3	2	v_R	3	2
r_S	3	2	v_S	3	2
r_W	1	1	v_W	2	1

Table 3.2: Overview of error regression modelling degree.

	σ_{r_R} [km]	σ_{r_S} [km]	σ_{r_W} [km]	σ_{v_R} [$\mathrm{m\,s^{-1}}$]	σ_{v_S} [$\mathrm{m\,s^{-1}}$]	σ_{v_W} [$\mathrm{m\,s^{-1}}$]
Enhanced						
G	0.19	2.1	0.18	2.4	0.21	0.15
P	0.068	1.6	0.028	1.9	0.08	0.036
W	0.089	2.4	0.033	2.9	0.11	0.018
Classic						
G	0.39	4.4	0.19	5.3	0.44	0.25
P	0.44	6.6	0.22	8.0	0.39	0.20
W	0.46	6.2	0.14	7.6	0.46	0.13

Table 3.3: Initial standard deviation of errors at TLE epoch, derived from GPS (G), pairwise (P), and weighted (W) differencing.

- varying orders of polynomial regression models are able to estimate error trends and growth for all components.

Next, the ability of the method to estimate this from differenced TLE data is investigated.

3.5.4. WEIGHTED DIFFERENCING

Table 3.3 shows the standard deviation of the error at the TLE epoch. It can be seen that both methods are fairly close to the truth. The largest differences are in the uncertainty in the cross-track state. This confirms findings in Ref [50] in estimating the error (growth) in this component. Fortunately, the error is smallest and most stable in this direction. Differences in r_W and v_W will therefore not be discussed further.

For the remaining components, the next largest difference is in the radial position and along-track velocity for eTLEs. These two components are underestimated by about 50 %. In both cases WD performs about 25 % better. Still the difference with the GPS results is not small. Nonetheless, the error in these components are still quite small compared to the absolute error (about 8 %). For cTLEs the results are closer and more favorable. The radial position uncertainty is 12 – 15% overestimated, while the along-track velocity is underestimated by 10 % only by PD.

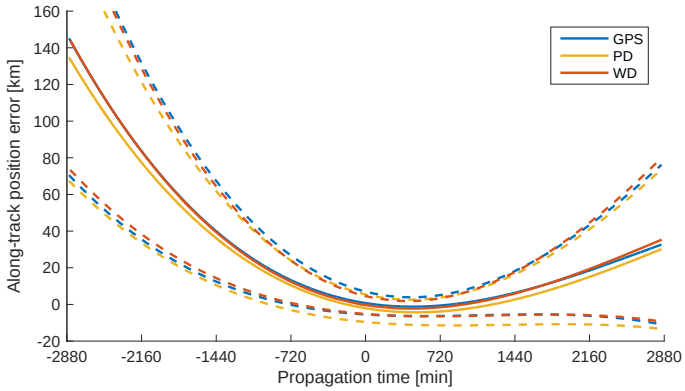

Figure 3.6: Comparison of fit of the along-track position error and uncertainty for enhanced TLEs.

The two major components (along-track position and radial velocity) show better results. Especially for WD, which conservatively overestimates each component for each type of TLE. PD on the other hand underestimates the errors for eTLEs by 25 %, while overestimating (more than WD) for cTLEs. Overall, the results can be considered acceptable, but not exact, depending on the analysis. It has to be restated that the data is very noisy. Better results are expected for different orbital regimes, where the SGP4 model provides a better match with the perturbations present.

Figures 3.6 and 3.7 show the error growth of the along-track position, estimated using the previously selected robust regression method for GPS and the standard (PD) and improved (WD) estimation methods for enhanced and classic TLEs, respectively. The error is plotted as the solid line, while the uncertainty (lower and upper) is shown using dashed lines of the same color. PD, here, should not be confused with previous implementations (which used binning), as regression was applied to all data sets in this comparison. The difference between binning and regression was previously demonstrated. Moreover, recall that the absolute position, absolute velocity, along-track position, and radial velocity produce nearly identical results.

The figure highlights the similarity between PD and WD, and the good match with GPS data. This further demonstrates the capabilities of the RLS regression method. For enhanced TLEs, the error and bounds of GPS and WD match almost exactly. For classic TLEs the bounds of WD lie outside the GPS bounds, which is of course favorable.

Moreover, it can be seen that both methods are able to estimate the temporal bias well. Table 3.4 gives an overview of the exact figures of the temporal bias as obtained from the minimum absolute position error. As RLS provides a continuous parametric solution, the minimum point is easily found through differentiation. The magnitudes of the bias are more than 6 and 4 hours for eTLEs and cTLEs, respectively. Considering the update frequency of several times per day this is quite significant. Especially in the case of eTLEs it is thus common for older TLEs to be more accurate now when propagated than more recently released TLEs. It has to be noted that for the majority of objects and also the period preceding re-entry, the update frequency is lower (e.g., twice per day).

Both WD and PD are able to estimate the sign and magnitude satisfactory. Especially

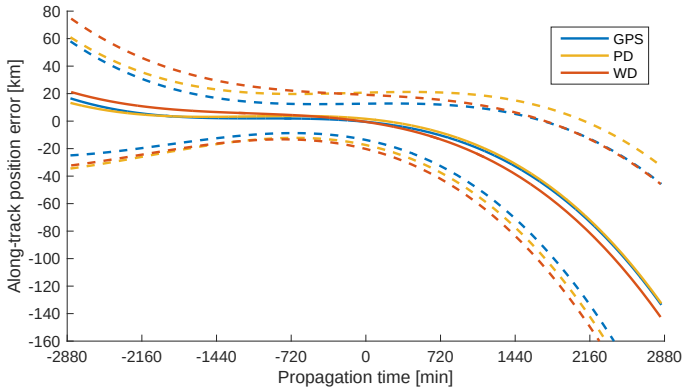

Figure 3.7: Comparison of fit of the along-track position error and uncertainty for classic TLEs.

	GPS [min]	PD [min]	WD [min]
Enhanced	375.3	314.2	372.1
Classic	−258.8	−292.2	−251.3

Table 3.4: Temporal bias estimates using different methods.

WD is almost spot on for eTLes and off by about 3 % for cTLEs.

Comparing enhanced and classical TLEs, it can be seen (Table 3.3) that overal the enhanced TLEs are much more accurate, having an uncertainty of roughly half across all components. Moreover, the uncertainty growth in forward propagation is reduced significantly. This clearly demonstrates the improved process of generation of enhanced TLEs. Their reduced accuracy and sharp growth in backwards propagation should be minded for applications that rely on this, such as splicing, where a (near) continuous state solution is created by combining the results from a series of TLEs.

This shows that:

- both methods are able to estimate the error uncertainty at TLE epoch reasonably well;
- WD perform better and tends to overestimate the uncertainty for the most important components;
- the error growth is much better approximated than the instantaneous uncertainty;
- the temporal bias is of the same order as the mean update interval;
- WD is able to very accurately estimate the temporal bias.

Next, the correlations between the components are analyzed.

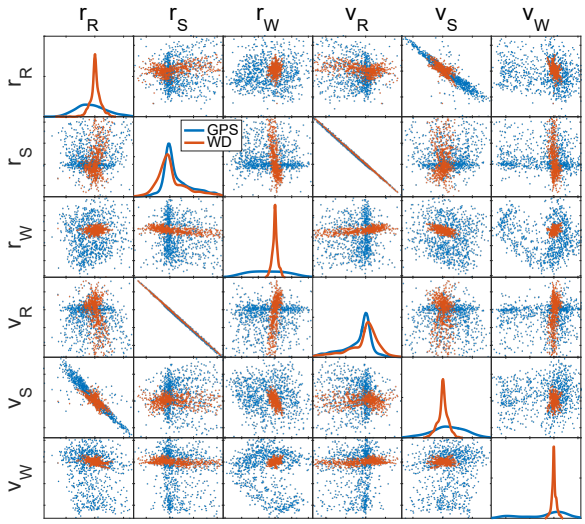

Figure 3.8: Correlation estimation using weighted differences (WD) compared to GPS of enhanced TLEs.

3.5.5. CORRELATIONS

Thus far only the errors and uncertainty have been analysed for all position and velocity components. However, these components are highly related. Such a strong correlation was demonstrated (in Figures 3.4 and 3.5) between the along-track position and radial velocity, and radial position and along-track velocity. To complete the uncertainty model, the correlations have to be taken into account. For analyses, like error propagation and sampling, these relations can have a significant influence on the outcome.

Figures 3.8 and 3.9 show joint and marginal distributions of the MVN distribution for enhanced and classic TLEs respectively. The marginal distributions are shown on the diagonal and are visualized using kernel density estimation. The joint distributions are shown as scattered data at the non-diagonal positions. The GPS and WD results are shown in blue and red, respectively. Note that each joint distribution is shown twice, as it remains identical when axes are switched. Thus only the joint distributions on one side of the diagonal need to be considered.

The first thing to note is that WD is able to estimate correlations for both TLE types. Visually it can be argued that for classic TLEs the best overlap with the GPS data is obtained. However, this does necessarily hold true, as will be demonstrated shortly. For enhanced TLEs the WD results show narrower bands overlapping the GPS results for most combinations. This, however, does not affect the correlations. The cause is attributed to narrow margins, which indicate underestimation of the radial position, along-track velocity and both cross-track components (diagonal positions 1, 3, 5 and 6). Moreover, the margins of the along-track position and radial velocity (diagonal positions 2 and 4) are properly estimated. This again confirms the results of the standard deviations as presented in Table 3.3.

The strong correlations between the along-track position and radial velocity, and ra-

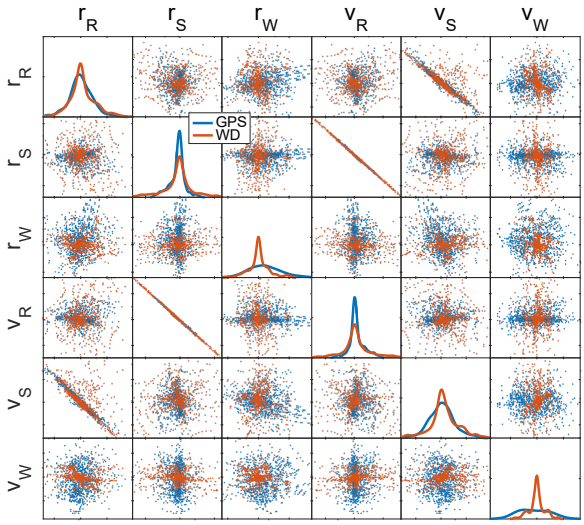

Figure 3.9: Correlation estimation using weighted differences (WD) compared to GPS of classic TLEs.

dial position and along-track velocity, are approximated well for both TLE types. They present the only strong correlations present in both GPS- and weighted-differenced data.

Lastly, the WD distributions tend to have stronger central peaks in the marginals, but nonetheless the distributions appear somewhat symmetric and approximately Gaussian.

The actual values of the estimated and true correlation matrices are shown in Tables 3.5 and 3.6. The top half presents the correlation matrix obtained using GPS differenced TLEs, while the bottom half presents the correlations found through weighted TLE differencing.

For enhanced TLEs, looking at Table 3.5, it can be seen that the variables that are only very weakly correlated (values below ± 0.10), the correlations tend to be overestimated on average by a factor 3-4. At the same time the relationship between the radial position and along-track velocity is underestimated by 30 %. The inverse relationship between the along-track position and radial velocity, however, is spot on. Lastly, although the magnitudes could be estimated better, it is important to note that the sign of the correlation is always estimated correctly (with the exception of ρ_{r_W,v_W}). This seems to indicate that correlation information could be potentially recovered from TLE data alone.

For classic TLEs, looking at Table 3.6, similar conclusions can be drawn. The magnitudes of (weak) correlations are overestimated, while the very large ρ_{r_R,v_S} is underestimated significantly. It is likely that propagation affects the correlations. Unlike previously, the signs of the weaker correlations are not even estimated correctly.

From this it has to be concluded that:

- correlations are difficult to estimate, where eTLEs show better behavior than cTLEs;
- no very strong (false) correlations were introduced nor correlations present ig-

GPS	r_R	r_S	r_W	v_R	v_S	v_W
r_R	1.00	0.08	0.06	-0.11	-0.93	-0.16
r_S	0.08	1.00	-0.09	-1.00	0.05	-0.08
r_W	0.06	-0.09	1.00	0.08	-0.11	-0.17
v_R	-0.11	-1.00	0.08	1.00	-0.03	0.10
v_S	-0.93	0.05	-0.11	-0.03	1.00	0.14
v_W	-0.16	-0.08	-0.17	0.10	0.14	1.00
WD	r_R	r_S	r_W	v_R	v_S	v_W
r_R	1.00	0.33	0.05	-0.34	-0.67	-0.49
r_S	0.33	1.00	-0.56	-1.00	0.01	-0.34
r_W	0.05	-0.56	1.00	0.56	-0.58	0.27
v_R	-0.34	-1.00	0.56	1.00	-0.01	0.35
v_S	-0.67	0.01	-0.58	-0.01	1.00	0.07
v_W	-0.49	-0.34	0.27	0.35	0.07	1.00

Table 3.5: GPS (top) and weighted (bottom) differenced (WD) derived correlation matrices for enhanced TLEs.

GPS	r_R	r_S	r_W	v_R	v_S	v_W
r_R	1.00	0.04	0.25	-0.02	-0.98	0.06
r_S	0.04	1.00	0.04	-1.00	-0.09	-0.11
r_W	0.25	0.04	1.00	-0.04	-0.30	0.00
v_R	-0.02	-1.00	-0.04	1.00	0.07	0.12
v_S	-0.98	-0.09	-0.30	0.07	1.00	-0.03
v_W	0.06	-0.11	0.00	0.12	-0.03	1.00
WD	r_R	r_S	r_W	v_R	v_S	v_W
r_R	1.00	-0.06	-0.13	0.06	-0.63	-0.22
r_S	-0.06	1.00	0.12	-1.00	0.01	-0.12
r_W	-0.13	0.12	1.00	-0.13	0.13	-0.07
v_R	0.06	-1.00	-0.13	1.00	-0.01	0.13
v_S	-0.63	0.01	0.13	-0.01	1.00	0.16
v_W	-0.22	-0.12	-0.07	0.13	0.16	1.00

Table 3.6: GPS (top) and weighted (bottom) differenced (WD) derived correlation matrices for classic TLEs.

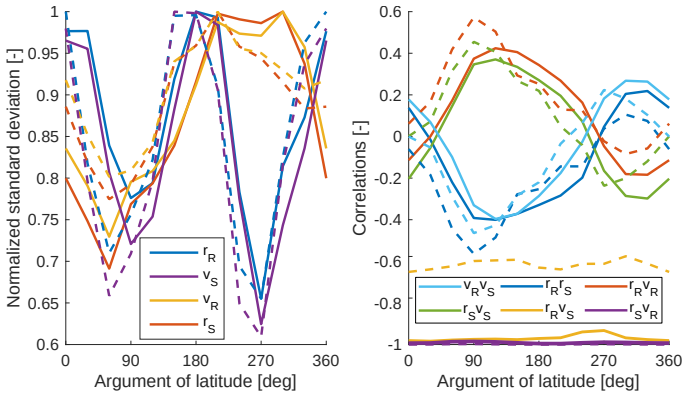

Figure 3.10: Uncertainty and correlation of classic TLEs as a function of AOL for GPS (solid lines) and weighted differenced (dashed lines) results. Legend entries are sorted to corresponding value at AOL = 0°.

nored by the method.

Combining Tables 3.3, 3.5, and 3.6, the covariance matrix is now fully defined. This information is important input to many types of error analyses, such as collision avoidance (COLA) and entry-point predictions [37]. Note that also for the uncertainty the estimation at epoch proved slightly worse than the estimation of the growth. This clearly indicates a sensitivity at the TLE epoch, where values are small and switch sign. Therefore, the sensitivity of the correlations is investigated further in the next section.

3.5.6. COVARIANCE SENSITIVITY

Intermediate propagation epochs were introduced to create a more evenly distributed set of error samples. It was chosen to generate samples at fixed positions in the orbit, rather than a fixed time interval, to eliminate any effect this might have on the error. In this section the sensitivity of the error as a function of AOL is investigated.

Figure 3.10 shows the standard deviation of the position and velocity samples in the RSW components and their correlation coefficients. This analysis has been performed for both types and results were found to be similar. Previously, the classic TLEs showed worst results for the estimation of the correlation coefficients. Hence the results for this type are shown. The standard deviations are normalised with their maximum magnitude for each component. The plot shows both GPS (solid lines) and weighted TLE differenced (dashed lines) solutions. The cross-track components are not shown. As for previous exercises, TLE differencing could not be used to obtain satisfactory approximations of these components.

First, the amount of variation of both correlation and uncertainty is quite striking. A variation in uncertainty of more than 35 % can be observed in the radial position and along-track velocity. Similarly, the along-track position and radial velocity vary significantly in uncertainty throughout the orbit.

For the correlation the case is perhaps even more variable. Correlations between most variables change from moderately correlated to uncorrelated and even switch sign,

depending on the position in the orbit. These (estimated) correlations should be used with caution.

Secondly, these trends and extrema are captured relatively well using WD. The most notable deviation is the correlation between radial position and along-track velocity. The true correlation (almost 1) is underestimated by almost 35 %, as already demonstrated by Table 3.6. Although the match between GPS and WD seemed very poor judging from this table, the right plot of Figure 3.10 tells a different story.

Again, the patterns are likely linked to the SGP4 propagation model, which captures the mean motion, and throughout an orbit creates predictable points of fluctuating errors in the state components. As also the direction of error of the components are predictable, the errors are also correlated.

A clear distinction between weakly and strongly correlated variables is present. The first class seems to vary significantly, change sign and average out over one orbit. The strongly correlated variables are almost invariant to the AOL.

Lastly, it is interesting to note that the enhanced TLEs are commonly reported at around the ascending node. The uncertainty in the components is much lower there. Detailed analysis between enhanced and classic TLEs should take this into account.

Overall, the following can be concluded:

- uncertainty and correlations vary greatly throughout the orbit;
- the trend of the correlations is captured rather well, despite the poor instantaneous estimation;
- the correlation between radial position and along-track velocity is underestimated, regardless of argument of latitude.

3.6. CONCLUSIONS

Enhanced TLEs offer improved uncertainty and error-growth properties. Even after the switch to enhanced TLEs the classic type remain in use, likely for additional tracking purposes. It is, however, simple to distinguish between the two in the presence of a mix by looking at the AOL.

The presence of a temporal bias was demonstrated and found to be of the order of the TLE update interval. Moreover, an asymmetry between forward and backward propagation was demonstrated. Both effects can have great influence on the propagation errors. This holds true especially considering their complete opposite nature in classic and enhanced TLEs. It is paramount to take these effects into account for any application relying on propagation of TLEs using SGP4, such as stitching TLEs for creating a continuous state-time solution.

Even for applications that employ the state at TLE epoch, it can be beneficial to consider the temporal bias and evaluate the state at the epoch of minimum mean error instead.

Robust least-squares regression was proposed as an alternative to data binning. This method has been shown to provide a continuous solution. This allows easy evaluation of the temporal bias. Moreover, it handles unedited data very well, reducing the need for

TLE and data pruning and tuning of parameters. Furthermore, component-error analysis has shown that this approach extends well for all position and velocity components.

TLE differencing can accurately estimate important error characteristics, like the temporal bias, error uncertainty and growth. Even correlations can be estimated to some degree. The correlations seem very sensitive to variations in argument of latitude. This is likely true for other parameters. Nonetheless, there is a clear distinction between strong and weakly correlated variables. The former vary and average out over one orbit, while the latter remain invariant.

Weighted differencing was compared against pairwise differencing. WD uses temporal bias information to determine the reference state. It has been shown to perform better than PD on all exercises. Especially the consistent (marginal) overestimation of major error components makes the technique favorable.

In conclusion, weighted differencing method using robust least-squares regression was proposed to improve previous TLE differencing methods. The proposed method was shown to be superior on all tests, consistently providing better approximations of the GPS differenced solutions.

The method is validated for the GOCE satellite during the period of investigation. Due to the low orbital altitude and increased TLE-update frequency further investigation is necessary in order to extend these conclusions to LEO in general. However, even for lower TLE-update rates, the method is expected to still perform satisfactorily, due to the intermediate evaluation epochs and the resulting near-continuous error data in time. Also, considering that the orbit considered presents a limit case in many respects, it is expected that the method will perform well in orbits in which errors are less and the SGP4 model provides a better fit.

The method is useful for the error analysis of a set of TLEs itself and in providing uncertainty input for other types of analysis. The method is computationally fast, can be applied to any object in the SATCAT, and deals well with noisy data. It is thus very suitable for demanding applications, such as conjunction analysis, that require frequent and fast processing for a large number of objects.

4

Analysis of Uncertainties and Modeling in Short-Term Re-Entry Predictions

Geul, J., Mooij, E. and Noomen, R.

Published [1] in Advances in Space Research, Vol. 61, No. 1, pp. 167–181, 2018

Satellite reentry predictions are used to determine the time and location of impacts of decaying objects. These predictions are complicated by uncertainties in the initial state and environment models, and the complex evolution of the attitude. Typically, the aerodynamic and error propagation are done in a simplistic fashion. Full six-degrees-of-freedom modeling and attitude control is proposed for studying the historic reentry case of the Gravity field and steady-state Ocean Circulation Explorer satellite. Improved error modeling and estimation of the initial state and atmospheric density are introduced for both global positioning system and two-line elements states. A sensitivity analysis is performed to identify the driving parameters for several models and epochs. The predictions are compared against tracking and impact predictions, and predictions by the European Space Agency Space Debris Office. The performed predictions are consistently closer to the true decay epoch for several starting epochs, while providing narrower windows than other predictions with higher confidence.

Nomenclature

a	=	acceleration, m/s^2
C_D, C_S, C_L	=	aerodynamic drag, side, lift force coefficient

[1] Minor modifications have been made for this thesis.

D_{max} = Kolmogorov-Smirnov test statistic
d = dummy sensitivity parameter
d_p = particle collision diameter, m
$\mathscr{E}$ = specific orbital energy, m^2/s^2
F = cumulative distribution function
F_K = ballistic coefficient scaling factor
$\hat{F}$ = sample cumulative distribution function
f_C = aerodynamic bridging function
$\mathbf{I}$ = inertia tensor, $kg\,m^2$
i = orbital inclination, rad
$\mathbf{K}$ = control gain matrix
K = ballistic coefficient, m^2/kg
Kn = Knudsen number, $kg\,m^2$
k = number of uncertainty parameters
L = characteristic flowfield dimension, m
m = mass, kg
N = total number of samples
N_S = number of search curve samples
$N_\subset$ = sample size of subset
N_R = number of sub-sampling repeats
n = mean motion, rad/s
P = specific work, J/(kg s)
p, q, r = roll, pitch, and yaw rates, rad/s
$\mathbf{Q}$ = state weighting matrix, various
$\mathbf{R}$ = control weighting matrix, $1/(N\,m^2)$
r = position, m
S_{ref} = reference area, m^2
S_i = first-order sensitivity index
S_{Ti} = total-order sensitivity index
T = control torque, N m
$\mathbf{u}$ = control vector, N m
v = velocity, m/s
$\mathbf{x}_0$ = nominal state vector
$\mathbf{x}_{com}$ = location of the center of mass, m
α_a = angle of attack, rad
β_a = side-slip angle, rad
$\beta^\star$ = TLE BSTAR drag term
ϵ = tolerance
$\dot{\theta}$ = Earth's rotational rate, rad/s
λ = mean molecular free path length, m
μ = normal mean
$\mu^\star$ = log-normal mean
ρ = atmospheric density, kg/m^3
σ_a = bank angle, rad
σ = normal standard deviation

$\sigma^\star$ = log-normal standard deviation

4.1. INTRODUCTION

Reentry predictions are important for determining the impact locations and times of decaying objects. Fragments often survive reentry and impact Earth, especially in case of large spacecraft with high-temperature resistant components. These predictions can be distinguished by their forecasting period into long term to medium term, short term, and break-up and survival predictions. For each type the tools, underlying methods, and analyses are distinct [29].

Short-term predictions range from several days to hours before reentry, starting from around 200 until 80 km altitude, when break-up commonly occurs. Tracking and Impact Predictions (TIPs), publicly released by the Joint Space Operations Center (JSpOC) [2], are the most common type, but short-term predictions are regularly performed by various actors [53–56]. Short-term predictions commonly report the expected decay epoch and the associated uncertainty as a percentage of the remaining orbital lifetime (for TIPs generally ±20 % or more). The uncertainty in remaining time can be used to compute the potential footprint along the satellite ground-track. Short-term reentry predictions are invaluable for many activities, such as tracking, informing relevant authorities, avoiding false detection by missile-warning systems, attributing liability resulting from impact, etc. [57]

Despite their importance, there is little research into these types of predictions, despite many promising developments in related fields. Areas of potential improvement are identified as spacecraft and aerodynamic modeling, statistical uncertainty propagation, and atmospheric modeling. The former two areas are the main focus of this chapter and explained in more detail below. The influence of atmosphere modeling is highlighted in the chapter and uncertainty estimation techniques for the atmospheric density are investigated. Improvements in thermospheric density and wind modeling [48, 58–60] and new and better forecasting of space-weather proxies [61] can benefit reentry predictions significantly, but are not further treated.

Improving the spacecraft and aerodynamic modeling can provide more accurate results, while reducing the number of assumptions. Commonly, the object is modelled as point-mass under the influence of aerodynamic drag deceleration, neglecting lift and side-force contributions [29]. Performing these predictions is far from straight-forward. The drag coefficient should account for changes in the flight environment [62, 63], which is either not included [53, 55] or through simplified analytic relations [54]. Likewise, changes in attitude orientation and motion should be accounted for, but it is difficult to predict all possible modes. This especially holds for slender bodies, where stable and tumbling modes create a myriad of different drag (and lift) scenarios. Finally, it is important to account for the relative likelihood of the possible modes to fully assess the final probability distribution.

All these effects can be accurately modelled in full six-degrees-of-freedom (6DOF) simulations, improving the fidelity of the simulations, while reducing the number of

[2] https://www.space-track.org/#/decay, retrieved: August 8, 2017

assumptions on the evolution of the satellite's attitude. 6DOF simulations are already employed in spacecraft-oriented break-up and survival analysis, such as Spacecraft Atmospheric Reentry and Aerothermal Breakup (SCARAB) by the European Space Agency (ESA) [64], and dispersion analysis of planetary entry vehicles [65]. Statistical 6DOF reentry simulations have been previously applied to reentry predictions of Delta-K rocket bodies [37]. Compared to point-mass predictions, the 6DOF simulations are more computationally expensive and require the object's shape, mass, and inertia properties to be known in greater detail.

The modeling and quantification of the uncertainties present in the state and models, and subsequent propagation of these uncertainties, can further improve the accuracy of predictions. Many methods assume a static symmetric uncertainty of ±20 % on the predicted decay epoch [54, 66]. Little research has been performed into the validity of these assumptions for a statistically significant number of objects over a long period. One study found that the true empirical confidence of the TIP window was dependent on the time to decay (TTD) and varied from 93 % to 98 % for 180 objects between 1987 and 1990 [57]. A study of reentry campaigns for 15 objects found that 5 % of the predictions fell outside the ±20 % window used by ESA [54]. The true dispersion boundaries and asymmetry are most sensitive to the atmospheric density and the initial rotational state [37], which can vary significantly per reentry. Statistical methods, such as Monte-Carlo (MC) propagation, transform the initial uncertainty under the influence of stochastic models to obtain a final desired distribution, providing more accurate intervals and insight into the shape of the distribution [37, 66]. The drawback is that performing these statistical predictions is considerably more computationally expensive. Several promising techniques offer more efficient error propagation [67–69] and sampling strategies [70], but are not further investigated at this stage.

This thesis aims to investigate the effect of uncertainties in short-term reentry predictions by studying the past reentry of ESA's Gravity field and steady-state Ocean Circulation Explorer (GOCE) satellite using statistical error propagation and improved spacecraft and uncertainty modeling. GOCE was a geodynamics and geodetic mission launched on 17 March, 2009 and re-entered on 11 November, 2013 [3]. The attitude of GOCE was controlled with magnetorquers. However, the reentry of GOCE is not considered a controlled de-orbit, which involves targeting low-risk impact zones. GOCE's reentry took significantly longer than initially predicted, due to its aerodynamic shape and controlled attitude, and much lower atmospheric densities than predicted. The reentry was previously studied by the ESA/ESOC Space Debris Office (SDO) [71] and Japan Aerospace Exploration Agency (JAXA) [56]. Furthermore, the reentry of GOCE is particularly interesting, because of the availability of many different measurements, such as TLEs, additional tracking by JSpOC, dedicated radar trackings, GPS solutions, and accurate solutions for the attitude. All these data allow for benchmarking the models and approaches.

For the reentry of GOCE, SDO implemented a number of improvements to their prediction method, including an asymmetric uncertainty window and by accounting for the transition from controlled to uncontrolled attitude motion. The latter was simulated by changing the drag coefficient after the attitude controller was assumed to be saturated,

[3] http://www.esa.int/Our_Activities/Observing_the_Earth/GOCE/Facts_and_figures, retrieved: August 8, 2017

effectively using two values of the drag coefficient. For controlled and stable motion the drag coefficient was estimated from GPS and ground station tracking data, while the drag coefficient for uncontrolled motion was obtained as the mean value from 6DOF simulations using SCARAB [71]. The latter drag coefficient was held constant. It is not clear whether the systematic errors in the atmospheric density at the time of reentry and the dependency on the flight regime were properly accounted for. The atmosphere models are generally not unbiased for the lower regions [38, 72] and especially not during the period of GOCE's reentry.

This thesis proposes statistical reentry predictions of GOCE using an improved version of the 6DOF reentry simulator as described in [37]. The simulator is extended by modeling the attitude controller. Further improvements are made to uncertainty models and estimation techniques for the initial translational state and atmospheric density. Initial conditions (both state and uncertainty parameters) are derived from both Global Positioning System (GPS) data and Two-Line Elements (TLEs). A sensitivity analysis is performed to identify the driving uncertainty parameters and their time dependency. Finally, the predictions are benchmarked against TIPs and SDO predictions.

The chapter is structured as follows. First, the trajectory simulator, including propagation, spacecraft, and environment models, is detailed in Sec. 4.2. The error propagation and the process of uncertainty modeling and estimation for both GPS-derived and TLE-derived states is presented in Sec. 4.3. In Sec. 4.4, the results of several reentry prediction cases and sensitivity analysis are presented and discussed. Lastly, the conclusions are given in Sec. 4.5.

4.2. SPACECRAFT PROPAGATION AND MODELING

The explanation of the complete reentry prediction simulator is split up into the (deterministic) propagation of a single trajectory (this section), and the modeling, estimation, and propagation of errors (Sec. 4.3).

4.2.1. EQUATIONS OF MOTION

The reentry simulator consists of a 6DOF trajectory propagator. The translational and rotational state are propagated using a numerical integrator. The complete state is represented by 13 state variables: the position and velocity in inertial Cartesian coordinates, the attitude quaternion, and the rotational rate in the body frame.

The equations of motion are integrated using a Runge-Kutta-Fehlberg 4(5) variable step-size integrator. The tolerance is set to $\epsilon_{rel} = \epsilon_{abs} = 1 \times 10^{-8}$. The step-size is allowed to vary between a minimum and maximum value of 1×10^{-4} and 1×10^{3} s, respectively. The EGM2008 gravity field model is used up to order and degree 5 [4]. Due to a desire to perform sensitivity analysis of many input parameters a simulation involving Monte-Carlo propagation of uncertainty, the computational cost a an individual run needs to be limited. The chosen settings were found to provide a good trade-off between accuracy and computational efficiency. Finally, the aerodynamic accelerations are modelled using:

[4] http://earth-info.nga.mil/GandG/wgs84/gravitymod/egm2008/egm08_wgs84.html, retrieved: August 8, 2017.

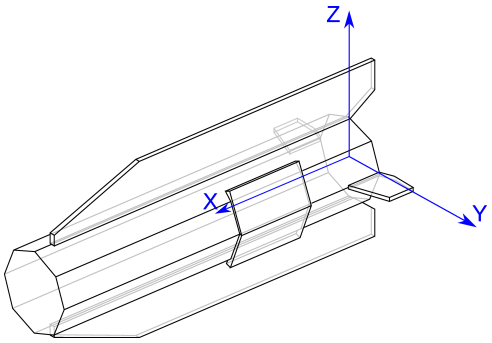

Figure 4.1: Schematic of the 44-panel GOCE aerodynamic model, which includes the origin and principal axes of the satellite physical coordinate frame (SPCF).

Table 4.1: GOCE satellite properties as of October 28, 2013.

Symbol	Value	Unit
$\mathbf{x}_{com}$	[2.536, 0.004, 0.001]	m
m	1002.152	kg
$\mathbf{I}$	$\begin{bmatrix} 173.0 & 20.2 & -1.7 \\ 20.2 & 2750.5 & -1.1 \\ -1.7 & -1.1 & 2723.2 \end{bmatrix}$	$\mathrm{kg\,m^2}$

$$\mathbf{a}_A = -\frac{1}{2}\begin{pmatrix} C_D \\ C_S \\ C_L \end{pmatrix}\frac{S_{ref}}{m}\rho v_A^2 \tag{4.1}$$

where C_D, C_S and C_L are the aerodynamic force coefficients, which will be defined in Sec. 4.2.3. S_{ref} is the reference area of the satellite, normalized as a unit area of $1\,\mathrm{m}^2$ in both the generation of the coefficients and Eq. (4.1). The spacecraft mass m is given in Sec. 4.2.2. Lastly, v_A is the velocity with respect to the atmosphere and ρ the atmospheric density, modelled using the NRLMSISE-00 model [38].

4.2.2. Spacecraft Model

GOCE is modelled as a combination of 44 flat panels, as illustrated in Fig. 4.1. The mass, center of mass, and inertia properties of GOCE are provided by ESA for the entire mission duration [5].These properties remained constant after October 28, 2013, and are used for the simulation. The position of the center of mass $\mathbf{x}_{com}$, the mass m, and the inertia tensor $\mathbf{I}$ in the satellite physical coordinate frame (SPCF) are shown in Table 4.1.

[5] https://earth.esa.int/web/guest/-/goce-mass-property-file-8276, retrieved: August 8, 2017.

Table 4.2: Summary of aerodynamic regimes and flow theories.

Regime	Knudsen number (Kn)	Theory
Free molecular	$Kn \geq 10$	Diffuse reflection
Transitional	$0.001 \leq Kn < 10$	Bridged
Continuum	$Kn < 0.001$	Mod. Newtonian

4.2.3. AERODYNAMIC MODEL

Throughout the decay and reentry the aerodynamic forces and moments need to be accurately modelled. To this end an aerodynamic database is constructed that relates aerodynamic force and moment coefficients to the spacecraft attitude (in terms of angle of attack α_a and side-slip angle β_a) and the Mach number, M.

However, as the spacecraft re-enters Earth's atmosphere, the atmospheric properties (reflected by the Knudsen number), and therefore the aerodynamic behavior, change substantially. In space (> 100 km) the atmospheric density is low and interaction between the gas molecules is rare, while at lower altitudes inter-molecular collisions start playing an important role. Different aerodynamic theories are thus required to model the aerodynamics. To accommodate this, three separate flow regimes are considered. The transitional regime provides a bridging between the free-molecular and continuum regimes.

These three regimes are distinguished by the Knudsen number:

$$Kn = \frac{\lambda}{L} = \frac{m_p}{\sqrt{2}\pi d_p^2 \rho L} = \frac{M}{N_A \sqrt{2}\pi d_p^2 \rho L} \tag{4.2}$$

$$Kn \approx \frac{\bar{M}}{N_A \sqrt{2}\pi \bar{d}_p^2 \rho L} \tag{4.3}$$

where λ is the mean molecular free path length and L the characteristic flowfield dimension. λ can be expressed as a function of the density, ρ, particle collision diameter, d_p, and particle mass, m_p. In turn, m_p can be expressed as the ratio of the molar mass M and Avogradro's number, N_A. The formula is simplified by assuming the mean values $\bar{M} = 28.9\,\mathrm{kg\,kmol^{-1}}$ and $\bar{d}_p = 367\,\mathrm{pm}$ [37].

The aerodynamic coefficients can then be generated and used depending on the regime. This approach is summarized in Table 4.2. For the free-molecular flow, a diffuse reflection model is used to describe the molecule-surface interaction [73]. The continuum flow is modelled using the modified-Newtonian theory, a local-inclination method suitable for hypersonic aerodynamics [37, 74]. A routine is implemented to derive coefficients for both free-molecular and continuum regimes. A coefficients database for the free-molecular flow was previously derived for GOCE and used to verify the implementation [75]. Note that shadowing is not taken into account, as its effects are considered negligible for the GOCE panel model. A selection of the coefficients is shown in Fig. 4.2.

The drag and lift force, and pitch-moment coefficients (Figs. 4.2a-b, c-d, and e-f, respectively) are shown as a function of the angles of attack and sideslip (Figs. 4.2a, c, e, and b, d, f, respectively). FM_V indicates the free-molecular solution obtained by an external source [75]. The figure highlights the differences between the free-molecular and

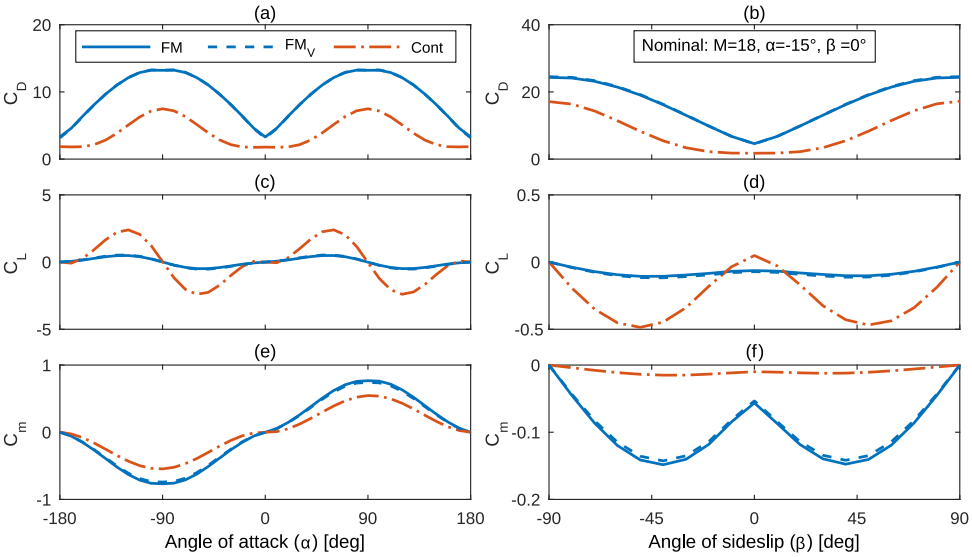

Figure 4.2: Selection of aerodynamic force and moment coefficients for GOCE for the free-molecular (FM) regime and continuum (Cont) regime, including an externally produced source FM_V for verification.

continuum-flow regimes. It can be seen that the drag coefficient is almost half for the continuum flow regime, while the lift coefficient is substantially higher. The two free-molecular solutions (FM and FM_V in the figure) show good agreement, demonstrating correct implementation of the coefficient database generator.

The intermediate transitional regime is modelled using a bridging function between the coefficients of the other regimes. Any force or moment coefficient C_X can be found using the following relation [76]:

$$C_X = f_C(Kn)(C_{X_{FM}} - C_{X_{cont}}) + C_{X_{cont}} \tag{4.4}$$

$$f_C(Kn) = \sin^2\left(\pi \frac{3 + \log_{10} Kn}{8}\right) \tag{4.5}$$

where $f_C(Kn)$ is the bridging function, and has a value of 0 at $Kn = 0.001$, 1 at $Kn = 10$, and in between zero and one for $Kn \in (0.001, 10)$.

This particular bridging function is often referred to as the "Shuttle" bridging function and was deduced from Space Shuttle data [76]. A "universal" bridging function does not exist and differs per object. The sine-squared form of Eq. (4.5) is a common choice, as it provides a smooth transition between the free-molecular and continuum-flow regimes. Moreover, it is preferred over the *erf-log* form, which approaches the bridging coefficients of zero and one asymptotically, making the sine-squared form more computationally efficient. The function is typically tuned by its two parameters, in this case $a_1 = 3/8$ and $a_2 = 1/8$, which are typical values found for the Shuttle, but also in line with other (blunt) bodies [77].

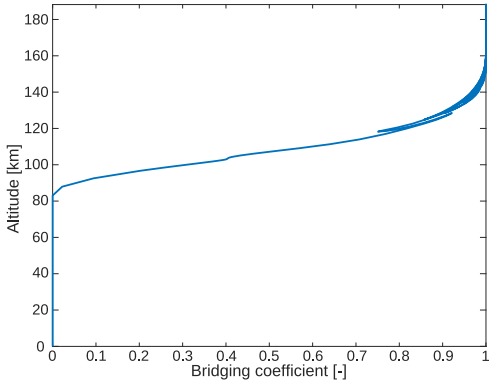

Figure 4.3: Example of the bridging function value for a typical reentry trajectory of GOCE.

Figure 4.3 shows the value of the bridging function throughout a typical reentry for GOCE. It can be seen that between 160 and 80 km the spacecraft is in the transitional regime. The altitude is not strictly decreasing, due to the oblate surface model. The decay epoch is achieved at 80 km, so the trajectory is not simulated into the continuum regime. Nevertheless, the continuum coefficients are important for the transitional regime.

4.2.4. CONTROLLER

GOCE was equipped with magnetorquers to stabilize its attitude. These torquers continued to function throughout the reentry. For a slender body like GOCE, a stable attitude has significant impact on the reentry predictions.

In Fig. 4.2 it can be seen that the drag coefficient for $\alpha_a = \beta_a = 0°$ is 3.15, compared to $C_D = 13.24$ for $\alpha_a = 90°$. For a constantly tumbling motion around the pitch axis the effective mean drag coefficient would be 9.41, almost three times higher than in a stable configuration. Not accounting for the controlled attitude would result in predictions that significantly underestimate the reentry epoch.

The maximum step size of the integrator needs to be limited to the control frequency to ensure proper response. The total number of integration steps is therefore increased, causing additional round-off errors and computational cost. Nevertheless, a control frequency of 10 Hz is chosen. The frequency was empirically found to provide a reasonable trade-off between control stability and computational cost.

A simple linear-quadratic regulator is implemented to simulate the torque control of GOCE. The input to the controller is the deviation from the nominal rotational state $\Delta\mathbf{x}$:

$$\Delta\mathbf{x} = [\Delta p, \Delta q, \Delta r, \Delta\alpha_a, \Delta\beta_a, \Delta\sigma_a]^\mathsf{T} \tag{4.6}$$

representing full-state feedback. Note that the attitude is represented here by the aerodynamic angles α_a, β_a, and σ_a. For propagation, however, quaternions are used instead.

The nominal state at epoch is assumed as follows:

$$\mathbf{x}_0 = [0, -n, 0, 0, 0, 0] \tag{4.7}$$

Table 4.3: Diagonal elements of the controller input and output weighting matrices **Q** and **R**.

Elements	Value	Unit
$[q_{11}, q_{22}, q_{33}]$	$[0.2^{-2}, 0.03^{-2}, 0.02^{-2}]$	$\mathrm{nrad}^{-2}\,\mathrm{s}^2$
$[q_{44}, q_{55}, q_{66}]$	$[0.15^{-2}, 0.06^{-2}, 0.15^{-2}]$	rad^{-2}
$[r_{11}, r_{22}, r_{33}]$	$[20^{-2}, 40^{-2}, 20^{-2}]$	$\mathrm{nN}^{-2}\,\mathrm{m}^{-2}$

Table 4.4: Gains for the LQR controller.

	p	q	r	α_a	β_a	σ_a
x	1.00×10^{1}	0	0	0	3.92×10^{-3}	-1.60×10^{-2}
y	0	1.33×10^{2}	0	2.67×10^{-2}	0	0
z	0	0	1.00×10^{2}	0	-3.17×10^{-1}	3.92×10^{-2}

where the only non-zero value is the pitch rate with respect to the inertial frame, assumed to be equal to the mean motion, n. The control outputs are torques around the body-frame axes. The control response **u** is defined as a function of the deviation multiplied by the control gains:

$$\Delta\mathbf{u} = [T_x, T_y, T_z] = -\mathbf{K}\Delta\mathbf{x} \tag{4.8}$$

where **K** is the control gain matrix, which needs to be determined.

The sensitivity of the controller is determined by input and output weighting matrices **Q** and **R**, respectively. Only the diagonals of the matrices are non-zero, the values are derived from maximum values observed during normal operational modes for GOCE and drag-free mode specifications are given in Table 4.3 [78].

Linearized equations of motion are used, and longitudinal and lateral control are decoupled [79]. The control gain matrix **K** is obtained by numerically solving the matrix Riccati equation using **Q** and **R** along a nominal 3DOF reentry trajectory.

The optimal gains remain nearly constant throughout the trajectory. Only for lower altitudes (< 60 km) there is some variation in the optimal gains. As the reentry simulations are stopped at 80 km, the gains are assumed to stay constant throughout the trajectory. Table 4.4 lists the control gains obtained.

4.3. ERROR MODELING, ESTIMATION, AND PROPAGATION

Error propagation is central to performing statistical reentry predictions. Error propagation, much like regular propagation, solves an initial-value problem, represented by the non-linear transformation of an initial uncertainty under the influence of a stochastic environment over time.

There are different error sources. A distinction can be made between state and model uncertainties. The initial state is uncertain due to uncertainties in the original observations, the imperfect models that relate observations to state variables, and approximations made in the orbit determination process. The environment and acceleration models are inherently deficient, and are further affected by errors in model inputs. For

reentry predictions the uncertainty in atmospheric density outweighs all other model contributions [80]. It is therefore the only model uncertainty considered.

4.3.1. ERROR PROPAGATION

The final decay-time distribution is the uncertainty of main interest. The initial uncertainty is propagated to obtain a final uncertainty using MC. The uncertainties are modelled as a deviation on top of the nominal state and sampled using a pseudo random-number generator (PRNG). The final probability density function (PDF) is estimated using kernel-density estimation to obtain a non-parametric solution of the decay-time distribution.

The convergence of the final distribution is investigated. A simulation with 10000 samples is performed starting at 48 hours prior to the reentry. Six different sub-sample sizes $N_{\subset}$ are defined as test cases, where $N_{\subset}$ =100, 200, 400, 1000, 2000, 4000 samples. For each value of N_s a random sub-sampling of the total number is done to obtain an estimate of the final PDF using kernel-density estimation (KDE). Depending on the sub-sample size $N_{\subset}$, the sub-sampling is repeated N_r times: N_r =3200, 1600, 800, 320, 160, 96, respectively. These values were empirically derived and found to provide a sufficient convergence on the test statistic.

To investigate the convergence of the simulation as a function of the number of samples, a two-sample Kolmogorov-Smirnov (KS) test has been performed. The KS test is a non-parametric statistical test to assess whether two sample sets are of the same continuous distribution, by comparing the cumulative distribution function (CDF) of each set. The KS test statistic is computed as the maximum absolute difference between the CDFs:

$$D_{max} = \max_x(|\hat{F}(x) - F(x)|) \tag{4.9}$$

where D_{max} is the test statistic, and $\hat{F}$ and F present the CDF of the sub-sample and full set, respectively.

The KS test statistic D_{max} is a measure of how well a subset approaches the full set. For each sub-sampling a different $\hat{F}$ is obtained. Therefore, for each sub-sample size $N_{\subset}$ the test can be performed N_r times, providing an estimate of the D_{max} value. Figure 4.4 shows boxplots of D_{max} as a function of $N_{\subset}$. As expected, the variability and mean go down with increasing number of samples. These values asymptotically approach zero, as the number of samples goes to infinity. The trend suggests that an exponentially increasing number of samples is required for a linear increase in accuracy.

A 5 % error in the CDF would result in a maximum error of 45 minutes or 1.7 % of TTD near the median. At this stage the width of high-probability confidence interval is such that in relation the error is considered acceptable. $N_{\subset}$ = 1000 exceeds the maximum error exactly once (D_{max} = 5.5% in all 320 comparisons). The median error for 1000 samples is merely 2.6 % (or 24 minutes in median shift, less than 0.9 % of TTD).

4.3.2. UNCERTAINTY IN THE TRANSLATIONAL STATE

The translational uncertainty is modelled as a six-dimensional multi-variate normal distribution (MVN), expressed in the orbital frame as the radial, along-track, and cross-

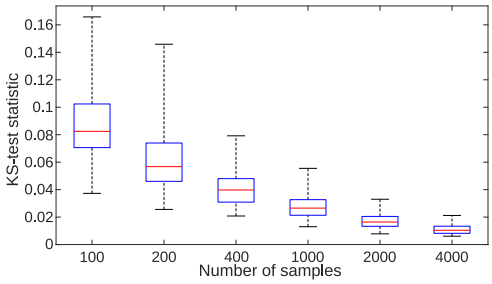

Figure 4.4: Range of Kolmogorov-Smirnov (KS) test values for MC sample size.

Table 4.5: Initial standard deviation of errors of GPS-derived state.

σ_{r_R} cm	σ_{r_S} cm	σ_{r_W} cm	σ_{v_R} $\mathrm{mm\,s^{-1}}$	σ_{v_S} $\mathrm{mm\,s^{-1}}$	σ_{v_W} $\mathrm{mm\,s^{-1}}$
1.03	12.7	1.31	0.15	0.009	0.016

track position and velocity. The orbital frame is a local frame, in which the errors behave quasi-normal. Standard deviations and means are considered for each dimension, as well as correlations between parameters. The MVN is defined by the mean vector and covariance matrix. These values and how they are estimated is different for GPS-derived and TLE-derived initial states and treated separately next.

GPS-Derived Initial Uncertainty

For the GPS-derived state, an estimate of the uncertainty is obtained from the orbit determination residuals. The orbit determination was performed in Ref. [81]. The corresponding residuals of November 9, 2013 were taken to obtain the standard deviations and correlations as reported in Tables 4.5 and 4.6, respectively.

TLE-Derived Initial Uncertainty

The process of estimating uncertainty from TLEs is different. For TLEs, observations or residual information is not publicly available. Fortunately, there are several methods to estimate this uncertainty [21]. Methods that rely on external data (e.g., raw observations

Table 4.6: Correlation matrix for initial state obtained through POD from GPS.

Component	r_R	r_S	r_W	v_R	v_S	v_W
r_R	1.00	0.80	-0.03	-0.80	-0.93	-0.06
r_S	0.80	1.00	-0.00	-1.00	-0.54	-0.05
r_W	-0.03	-0.00	1.00	0.00	0.04	0.02
v_R	-0.80	-1.00	0.00	1.00	0.55	0.05
v_S	-0.93	-0.54	0.04	0.55	1.00	0.06
v_W	-0.06	-0.05	0.02	0.05	0.06	1.00

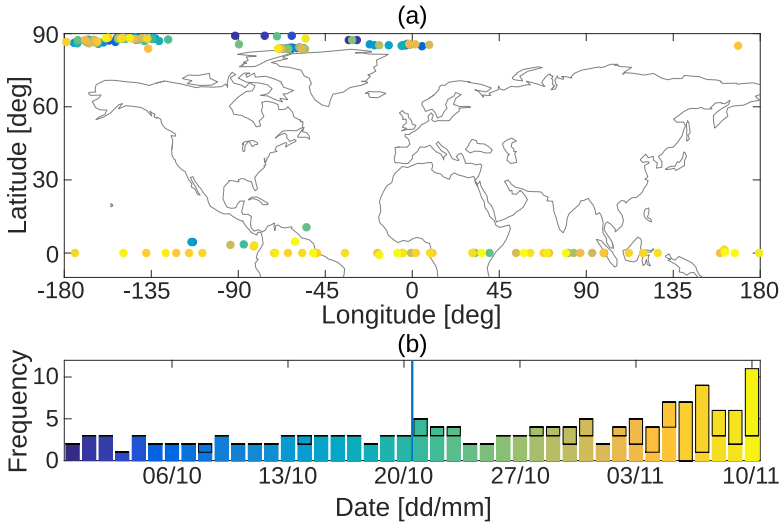

Figure 4.5: Overview of TLEs as a function of longitude and latitude (a) and frequency of TLEs per day (b), where the portion of cTLEs are outlined.

or GPS/SLR solutions) are not considered, as these data are not available for many objects.

For this study a newly developed robust weighted differencing (WD) method is used, as presented in Chapter 3 [82]. It differs from traditional differencing methods in that the TLE at epoch is not considered as truth. Instead, a weighted truth is estimated using multiple TLEs. The method is also robust, removing the need for outlier removal and filter tuning. Moreover, the method only requires TLEs and Simplified General Perturbations (SGP4) model for propagation, so it is generally applicable to any object in the satellite catalog (SATCAT).

Figure 4.5a gives an overview of the TLEs as a function of latitude and longitude at the TLE epoch for a period of 42 days prior to reentry, which is a reproduction of Fig. 3.2 [82]. The color of each marker corresponds to the bars in Fig. 4.5b.

The bar plot in Fig. 4.5b shows the number of TLEs for each day. Bars that are (partly) outlined indicate the portion of TLEs associated with the ascending node (latitude $\sim 0°$).

The period after October 21, 2013 is considered as the reentry period. It has almost twice the number of TLEs (101 versus 52) and an equal mix of TLEs associated with a latitude of $\approx 0°$ and $\approx 90°$ (50 versus 51, respectively). The additional TLEs are assumed to result from additional tracking by JSpOC. It is shown that these are, in fact, classic TLEs and enhanced TLEs, respectively, which exhibit significantly different error characteristics, as described in Chapter 3. Therefore, they will be treated separately.

Table 4.7 shows the standard deviation of the error at the TLE epoch as obtained by the WD method. Comparing the two TLE types, it can be seen that the uncertainty in eTLEs is roughly half that of cTLEs.

Table 4.7: Initial standard deviation of errors at TLE epoch, derived using the weighted differencing technique from Chapter 3.

Types	σ_{r_R} km	σ_{r_S} km	σ_{r_W} km	σ_{v_R} $\mathrm{m\,s^{-1}}$	σ_{v_S} $\mathrm{m\,s^{-1}}$	σ_{v_W} $\mathrm{m\,s^{-1}}$
eTLE	0.089	2.4	0.033	2.9	0.11	0.018
cTLE	0.46	6.2	0.14	7.6	0.46	0.13

Table 4.8: Bounds on uniform rotational uncertainty [78].

Type	Unit	Roll	Pitch	Yaw
Attitude	rad	±0.15	±0.06	±0.15
Rates	$\mathrm{mrad\,s^{-1}}$	±0.20	±0.03	±0.20

4

4.3.3. Uncertainty in the Rotational State

The uncertainty in the rotational state is not estimated separately for GPS and TLEs. Rather, the rotational state is assumed to be distributed uniformly within the maximum values for the drag-free mode and given in Table 4.8 [78].

As the angles are very small it is acceptable to sample uniformly directly within the reported bounds. However, for larger bounds direct uniform sampling of the angles becomes invalid. As sampling in spherical coordinates causes roughly an equal number of samples per elevation, the samples will tend to get more concentrated towards the poles. In such a case the samples should be drawn uniformly over a sphere, as described in Ref. [37].

4.3.4. Uncertainty in the Atmospheric Density

The atmospheric density is modelled using the NRLMSISE-00 model. The atmospheric density has a log-normal uncertainty. The mean and variance depend on the altitude and space-weather conditions. The uncertainty for the $120-200$ km altitude range was derived in Ref. [37] and found to be $\mu^\star = 0.98$ and $\sigma^\star = 1.13$. The uncertainty for the $200-400$ km altitude range is $\mu^\star = 0.93$ and $\sigma^\star = 1.17$ [38].

Note that the mean here is an average mean and can vary significantly depending on space-weather conditions. In Ref. [72] several atmospheric models are compared for altitudes ranging from 150-240 km. It is found that the mean is typically given within ±10 % and a standard deviation around 15 %.

To sample the uncertainty in the atmospheric density, the values of $\mu^\star$ and $\sigma^\star$ need to be determined. As with the initial translational state uncertainty, there are several ways of determining these values. In Ref. [37], values from literature were used. However, these values are conservative, as they are derived for many different objects and conditions simultaneously. Determining the true parameters on a per-object, or per-reentry basis, will provide more narrow and tailored uncertainty distributions. For this, object-specific data are required.

The mean density error $\mu^\star$ is estimated for each starting epoch and each input set

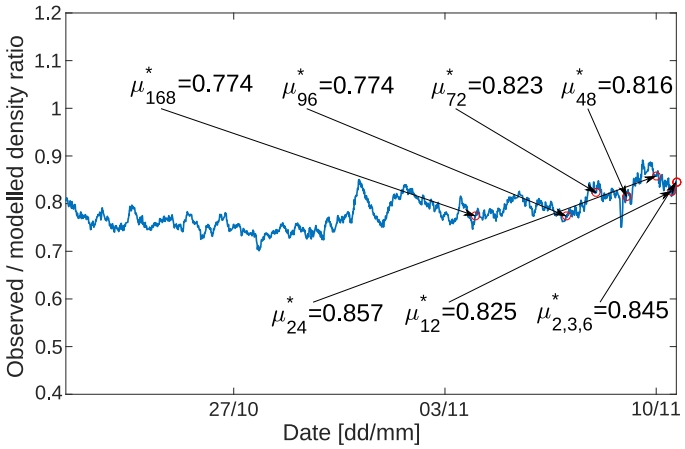

Figure 4.6: Estimated mean density error $\mu^\star$ for GPS-based density estimates.

separately. The atmospheric bias is sampled at the start of the simulation and remains fixed throughout a single simulation. The atmospheric uncertainty $\sigma^\star$ is assumed to be 1.082 for GPS and derived from analysing the GPS-derived accelerations in the next section. Due to the limited temporal resolution of TLE-derived density ratios (see Sec. 4.3.4), $\sigma^\star$ is assumed to be 1.13, in accordance with the uncertainty found for several test-objects [37].

GPS-DERIVED DENSITY ESTIMATES

To estimate the atmospheric density uncertainty parameters, GPS-derived non-gravitational accelerations are used, as obtained in Ref. [81]. These accelerations are assumed to primarily consist of the aerodynamic contribution. Modelled aerodynamic accelerations are computed using attitude solutions, the NRLMSISE-00 atmospheric model, and the aerodynamic database. The differences between the modelled and observed accelerations are explained by (i) random errors in the density modeling, (ii) systematic errors in density models, and (iii) systematic errors in the aerodynamic models. The contributions of (ii) and (iii) are coupled through Eq. (4.1) and estimated jointly as the mean density error $\mu^\star$. The contribution of (i) is estimated as $\sigma^\star$.

Figure 4.6 shows the 10-minute averaged density ratios. The estimate of $\sigma^\star$ is obtained by subtracting the 10-minute averaged signal from the 10 Hz signal. The value for the entire analysis period is used and estimated to be 1.082, as mentioned earlier. It is assumed that it is representative for the reentry period as well.

For the estimates of $\mu^\star$ the average over one orbital revolution was taken at several epochs prior to reentry: 168, 96, 72, 48, 24, 12, 6, 3, and 2 hours. These values are indicated in Fig. 4.6. The method allows for very accurate predictions of the atmospheric uncertainty.

TLE-DERIVED DENSITY ESTIMATES

The drawback of the GPS-derived density estimates is that it relies on accurate and frequent GPS solutions. GPS data are generally not available or existent for most objects in

the SATCAT.

For TLE states the ratio of the observed and modelled ballistic coefficients is derived instead, which is similar to the ratio of observed and modelled aerodynamic accelerations, and can be used to estimate the mean density error $\mu^\star$. The density variability $\sigma^\star$, however, cannot be estimated using this method, due to the low frequency of the TLEs (in the order of two per day). This value needs to be taken from literature instead. Moreover, the mean density-error obtained using TLEs is considered less accurate, as it presents the average over a longer period.

The ballistic coefficient is already reported as $\beta^\star$ as part of the TLEs. During orbit determination, the estimate of $\beta^\star$ includes the difference between the true and predicted atmospheric density by the simple exponential density model of SGP4, as well as other modeling deficiencies. Estimates of $\beta^\star$ often have large spikes and negative values, and are therefore not used in this study.

Instead the ballistic coefficient is obtained through retrofitting. A history of the semi-major axis is used to determine the rate of change of the orbital energy. The energy and semi-major axis are related through the following equation for an unperturbed two-body problem:

$$\mathscr{E} = \frac{v^2}{2} - \frac{\mu}{r} = -\frac{\mu}{2a} \tag{4.10}$$

where $\mathscr{E}$ is the energy per unit mass. The work done by the atmosphere can be approximated by [83]:

$$P_A = \mathbf{v} \cdot \mathbf{a}_A = -\frac{1}{2} K \rho n^3 r^3 \left(1 - 2\frac{\dot{\theta}}{n}\cos i\right) \tag{4.11}$$

where K is the ballistic coefficient, P is the work, a the acceleration, $\dot{\theta}$ the Earth's rotational rate, i the inclination, and n the mean motion.

The energy at each state is computed and numerically differentiated to compute the rate-of-change of the energy, $\dot{\mathscr{E}}$. By assuming that the atmospheric drag dominates other non-conservative perturbations, Eq. (4.11) can be equated to $\dot{\mathscr{E}}$, from which an estimate of K can be obtained.

Figure 4.7 shows the result of the ballistic coefficient retrofitting for both TLE types (solid lines), as well as the ballistic coefficients reported by the TLEs (dashed lines). The $\beta^\star$ from the TLEs was related to the ballistic coefficient K using the following formula [6]:

$$\beta^\star = \frac{\rho_0 K}{2} \tag{4.12}$$

Discrepancies between ballistic coefficients obtained using retrofitting and those reported by the TLEs originate from errors absorbed by $\beta^\star$ during the orbit determination, and differences between NRLMSISE-00 and the atmospheric model of SGP4. Overall, eTLE solutions appear to be much more consistent and stable. For cTLEs, a similar trend (with a clear bias) between c$\beta^\star$ and cRF can be observed until November 5, 2013. For the remaining period this difference diverges, due to increasing differences between the two

[6] http://celestrak.com/columns/v04n03/, FAQs: Two-line Element Set Format, retrieved: August 8, 2017.

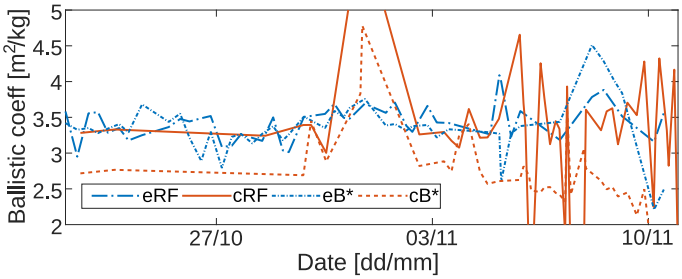

Figure 4.7: Ballistic coefficients for both TLE types: enhanced (e) and classic (c). For each type, the coefficients are obtained from two sources: as estimated using retrofitting (RF) and as reported in the TLEs (B).

atmosphere models. For the same (final) period the retrofit is seen to fluctuate greatly, due to increasing variations in TLE accuracy. The mean, however, remains stable. Especially for cTLEs, it is recommended to use smoothing to obtain a better estimate of the ballistic coefficient at the cost of further reducing the temporal resolution.

The modelled ballistic coefficients are obtained from the aerodynamic model for the same period, and evaluated at the TLE epochs. A constant attitude $\alpha_a = \beta_a = 0°$ is assumed, while the speed ratio is derived from the TLE states. The ratio of the retrofit and modelled ballistic coefficients is used to estimate $\mu^\star$. The value has to be obtained by smoothing the results over several TLEs, resulting in $\mu^\star = 0.810$ for the entire reentry period under consideration.

4.4. RESULTS

First, the effect of the controller and atmospheric modeling is investigated in Sec. 4.4.1. Second, the differences between the GPS-based and TLE-based reentry predictions are explored in Sec. 4.4.2. Third, the statistical uncertainty propagation is compared against simplified uncertainty propagation methods in Sec. 4.4.3. For these first three studies, GPS-based predictions starting at 48 hours prior to reentry are used as a baseline with 1000 samples. Fourth, the sensitivity of the predictions to the uncertainty parameters for various models and starting epoch is investigated in Sec. 4.4.4. Fifth, GPS-based predictions are made at several epochs prior to the true decay epoch. These predictions are compared with the multiple historical TIP messages and SDO predictions in Sec. 4.4.5.

4.4.1. CONTROLLER AND ATMOSPHERIC MODELING

To investigate the effect that the modeling has on the simulation results several cases are ran and compared. These cases focus on the comparison of modelled, ideal, and no control (Cases A-C), and the effect of the atmospheric uncertainty (Case A and D-E). Table 4.9 gives an overview of the different settings for each case.

Note that Case A presents the baseline, with all models implemented, and translational and rotational motion simulated. The logarithmic standard deviation of atmospheric uncertainty $\sigma^\star$ as reported in literature is used, to highlight the proportionality of this uncertainty in general, compared to other error sources.

The results are shown in Fig. 4.8. The decay-time distributions are shown as the prob-

Table 4.9: Overview of simulation cases for different modeling scenarios.

Case	DOF	Attitude control	$\mu^\star$	$\sigma^\star$
A	6	Yes	0.816	1.13
B	3	Ideal	0.816	1.13
C	6	No	0.816	1.13
D	6	Yes	0.980	1.13
E	6	Yes	0.816	1.06

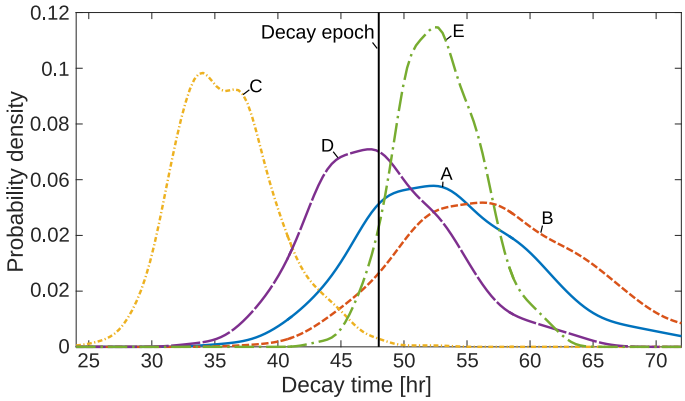

Figure 4.8: Decay-time distributions for different modeling scenarios, compared to the true reentry epoch. An overview the scenarios is given in Tab. 4.9

ability density as a function of the simulation time. Note that the simulation start epoch was exactly 48 hours before the decay epoch.

Case A overestimates the true decay time, having a mean of 53 hours (10 % more). The width of the distribution is rather large, i.e., 40 hours (3σ bounds), covering over 26 orbits.

Case B presents several simplifications: only translational motion (3DOF) and the influence of the drag is simulated, reducing the state vector from 13 to 6 variables. The major advantage of 3DOF is that the computational efficiency is much higher, as the variable step-size integrator is not limited by the control frequency. Because the aerodynamic angles of $\alpha_a = \beta_a = 0°$ have been fixed, the drag coefficient only varies with Mach number. The same aerodynamic database of the 6DOF simulation is used for the computation of C_D for the 3DOF simulation. As can be seen, the resulting decay-time distribution for this case is shifted towards the right by 4.3 hours, overshooting the true decay time by almost 10 hours. This case represents an overly idealized attitude-control scenario. Small aerodynamic angles of the order of the rotational uncertainty during controlled motion, the aerodynamic lift contribution, and uncontrolled motion after controller saturation are not accounted for. The width of the distribution is about 10 % wider than for Case A, which is caused by the shift in median.

Table 4.10: Overview of simulation cases for different modeling scenarios.

Case	Source	State	Atmosphere
A	GPS	OD residuals	Accelerations
F	eTLE	Differencing	RF, literature
G	cTLE	Differencing	RF, literature

Case C illustrates the effect of an uncontrolled attitude. The controller, together with the aerodynamic shape of GOCE, makes the reentry unique and difficult to predict. Compared to stable motion the drag of tumbling motion is nearly 3 times higher, shortening the reentry significantly. The results show that the inclusion of a controller is crucial for the proper reentry simulation of GOCE and by extension other controlled satellites. The median is situated at 36 hours. The spread is similar to before at 25 hours, or 70 %.

Cases B and C present limit cases for the controlled reentry. Underestimation of the maximum control torques will result in impact predictions between Cases C and A, while overestimation of the maximum torques will result in predictions within Case A and B.

Case D illustrates the effect of not accounting for the bias in the atmospheric density. Such a case presents itself when the mean density error cannot be estimated due to insufficient knowledge of the attitude and/or spacecraft mass and geometry. In this case values from literature have to be used, as was done by in Ref. [37]. The result shows that for GOCE the density would be overestimated, causing a faster reentry than in reality. Together with Case C, the atmospheric-density bias presents the major driver in prediction accuracy. Clearly, estimating the bias improves the results significantly, and should be applied whenever possible.

Case E presents what would happen if the atmospheric uncertainty were halved. Ongoing research into atmospheric models show great potential for reducing the atmospheric uncertainty. The PDF in this case is much narrower, reducing the width of the PDF to 25 hours (at 3σ bounds). The large difference highlights the importance of reducing the atmospheric uncertainty. Moreover, the averaged density bias used for case D, as derived in Ref. [37], is likely too close to one and should in reality be smaller. Especially, considering the mean bias of $\mu^\star = 0.93$ obtained using the Jacchia dataset for the $200-400$ km range, as presented in [38]. Unfortunately, data to accurately assess the uncertainty of atmosphere models in the $120-200$ km range are extremely limited.

4.4.2. GPS-BASED VERSUS TLE-BASED PREDICTIONS

Different uncertainty estimation methods were derived and presented in Secs. 4.3.2 and 4.3.4. Based on the availability of GPS solutions, a more accurate initial state and better atmospheric uncertainty parameters can be obtained. The GPS-based reentry predictions are compared against the more general TLE-based predictions. For TLEs a distinction is made between enhanced and classic TLEs.

Figure 4.9 shows the result of Cases F and G compared to Case A. Cases F and G show the results for the enhanced and classic TLEs, respectively. The enhanced TLEs were shown to have better accuracy and reduced error-growth for forward propagation.

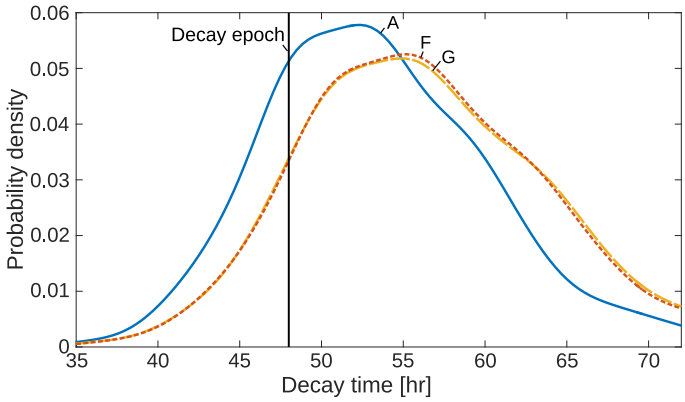

Figure 4.9: Decay-time distributions for TLE-derived states and uncertainty parameters, compared to GPS baseline prediction and the true reentry epoch.

The improved propagation stability of enhanced TLEs is limited to SGP4 and does not necessarily improve the prediction ability. The improved accuracy at epoch, however, causes a small, but positive difference.

Compared to Case A both decay-time distributions are wider, which is to be expected due to increased uncertainty in the initial state. The 3σ width is 54 and 56 hours for enhanced and classic TLEs, respectively. TLE-based predictions are found to be about 35 % wider than the GPS-based predictions. Moreover, a shift towards the right can be observed for both TLE predictions, due to the slightly lower estimated atmospheric-density bias as a result of the smoothing process.

However, considering that the positional accuracy is on the order of decimetres for GPS and kilometres for TLEs, the difference in reentry prediction uncertainty is not that large. In contrast to the atmospheric-density bias, the positional uncertainty has only a moderate effect on the final decay-time distributions. By extension, the differences between Case F and G are even less. Enhanced TLEs were found to be twice as accurate, but this only results in a 4 % reduction of the final uncertainty window.

4.4.3. Simplified Error Propagation

Commonly, simplified strategies are employed to propagate the error in time. Benefits of such strategies are low computational cost and a reduced (uncertainty) modeling effort. Two common approaches are investigated further and compared to statistical error propagation. In both approaches only the nominal state of the spacecraft is propagated to obtain the median of the final decay-time distribution. The uncertainty window is then derived, either by placing an empirical uncertainty on the nominal state or by performing two additional propagations to obtain the bounds.

In the case of empirical uncertainty bounds, generally the uncertainty is assumed to be ±20 % of the remaining orbital lifetime on top of the nominal decay time. These bounds are derived by studying historic re-entries. Reference [57] shows that confidence intervals of TIPs range from 93 % to 98 %, for orbital lifetimes ranging from seven days to three hours, respectively. The assumption that the uncertainty window width is al-

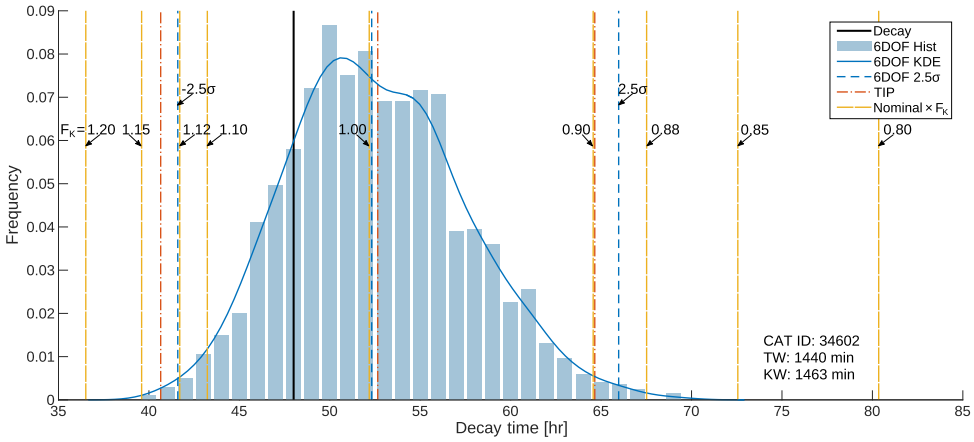

Figure 4.10: Statistical error propagation (6DOF) compared to simplified error propagation strategies (TIP and factored nominal) for performing reentry predictions of GOCE 48 hours prior to reentry.

ways ±20 % provides a good rule of thumb for estimating 2σ bounds. This assumption, however, is population based, and does not necessarily extend well to individual (future) cases. In the case of propagating additional samples to obtain the bounds, commonly the ballistic coefficient is varied ±20 % to obtain samples for the lower and upper limit of the uncertainty.

Both approaches assume that the nominal state represents the uncertainty median. Furthermore, the first approach assumes that the uncertainty is symmetrical about the assumed median, while the second approach assumes a symmetrical uncertainty in the product of the atmospheric and aerodynamic uncertainty, yielding an asymmetric distribution in time.

To investigate these two approaches further, their results are compared against the statistical reentry predictor. The starting epoch is chosen to be 48 hours prior to the actual decay. At this epoch both 6DOF and TIP predictions were found to be close to each other, but overestimating the true decay time significantly.

Figure 4.10 shows the reentry predictions. The true impact is indicated using the solid black vertical line at 48 hours. For the 6DOF statistical reentry predictions, the obtained uncertainty distribution is visualized using a histogram (using 1 hour bins) and kernel-density estimation. Moreover, the 2.5σ (98.758 %) confidence interval is indicated using the dashed lines. This value represents the upper limit of the TIP confidence. The actual TIP results are plotted as the three dash-dotted lines, to demonstrate the empirical uncertainty bounds. Lastly, the approach using varying values of the ballistic coefficient is shown using the long-dashed lines. The different variations are indicated by their F_K value, where $F_K = 1 \pm 0.20$ represents the ±20 % case described above. In total nine different values for F_K were chosen (including the nominal case $F_K = 1$), to illustrate the effect of using different values.

The median of the statistical error propagation is comparable to the TIP prediction for this epoch. The nominal single propagation corresponding to $F_K = 1$ also lies very close to the median of the statistical propagation. Such agreement only occurs when the

uncertainties of the translational and rotational state of the distributions are relatively symmetrical and unbiased. For this case a good estimate of the median of the decay-time uncertainty can be obtained using a single propagation of the nominal state. Note that this only holds for a nominal 6DOF propagation and not a single 3DOF propagation. It was previously demonstrated that the nominal 3DOF propagation would overshoot the true decay time even further.

As can be seen, the uncertainty distribution is asymmetrical. The upper limit is further away from the median than the lower limit, which is a characteristic of reentry distributions. Both the TIP window (TW) and the 2.5σ window of the KDE (KW) are of comparable width: 1440 and 1463 minutes, respectively. However, by default the uncertainty of the TIP is symmetrical in time. The lower bound of the TIP overestimates the uncertainty, while the upper bound fails to capture the full width of the uncertainty.

Looking at the four pairs of equal variation to the ballistic coefficient, $F_K = 1 \pm (0.10, 0.12, 0.15, 0.20)$, it can be seen that resulting windows are indeed asymmetric in time. These windows are, however, much more asymmetric than the uncertainty distribution obtained using the statistical approach. The lower bound of $F_K = 0.88$ shows good agreement with the statistical window, but its corresponding upper bound of $F_K = 1.12$ overshoots by more than an hour. The propagation $F_K = 0.88, 1.00, 1.11$ would likely result in the best agreement with the statistical method in this case. The earlier described $F_K = 1 \pm 0.20$ results in too conservative estimates. It is apparent that the bounds are very sensitive to the choice of F_K. Considering the results of this study, the choice of F_K depends highly on the satellite under consideration, the remaining orbital lifetime, and the propagation set-up.

4.4.4. Sensitivity Analysis

Introduction

The full uncertainty model is 13-dimensional. To investigate which parameters drive the uncertainty, a sensitivity analysis is performed. The sensitivities of the reentry simulation with respect to the uncertainty parameters are computed for various degrees of modeling and for several starting epochs

For the sensitivity analysis the extended Fourier amplitude sensitivity test (eFAST) method is used [84, 85]. eFAST is suitable for analysing the sensitivities of non-linear systems. The method varies the input parameters along a sinusoidal search curve of a particular frequency, causing a variation in simulation output. eFAST decomposes the variance of the output to the input parameters by Fourier analysis. The search curve has to be sampled with enough fidelity to recover the search-curve frequencies in the Fourier analysis. The minimum recommended number of samples, N_S, is 65. Moreover, the curves are re-sampled N_R times. The total number of samples is thus $N = N_S N_R k$, where k is the number of uncertainty parameters.

The primary outputs of the eFAST method for the analysis are the first-order and total-order sensitivity indices. Both indices assume values between 0 and 1, where 0 indicates no influence and 1 indicates complete dependence. The first-order sensitivity index is the variance of the output at the parameter's particular frequency divided by the total output variance. The total-order sensitivity index is calculated as the remaining variance after the contribution of all other parameters is removed, and includes non-

linear and correlated effects.

An additional uncertainty parameter is introduced, which is not used in the reentry simulator. This parameter is referred to as the dummy parameter and has no influence on the output. Ideally, the sensitivity indices of the dummy parameter should be zero. However, due to the stochastic nature the indices will be non-zero. The sensitivity to the dummy is used to test for significance of the other sensitivities. Parameters with a sensitivity index of less than or equal to the dummy sensitivity should be considered not significantly different from zero.

The sensitivity analysis is performed for three different simulation set-ups: 3DOF, controlled 6DOF, and uncontrolled 6DOF. Moreover, for most time-dependent models the sensitivity of the output to its parameters is also time dependent. To investigate this dependency further the sensitivity indices are computed for simulations starting at several values of the remaining orbital lifetime.

The number of search curves per parameter is chosen to be 5 with 260 samples per curve. Previous trials were conducted with $N_S = 65$ and $N_S = 130$, but resulted in high sensitivity indices for the dummy parameter. As the atmospheric uncertainty is the primary contributor to the total uncertainty, the other parameters are relatively small in comparison. Including the dummy parameter and with the chosen settings for the search curves, this results in $N = 18\,200$ samples for 6DOF and $N = 10\,400$ for 3DOF per analysis.

The sensitivity indices were found to be severely affected by outliers in the data. A routine was therefore implemented to check for outliers in the results. The studentized residuals of the samples of each search curve were calculated separately. Samples with a residual of higher than 4 were labelled as outliers. Figure 4.11 shows an example of the simulation output along a single search curve with outliers. Two types of outliers are present in the figure: a null result (caused by a crash in the simulation) and an unrealistic reentry time. These spikes cause interference in the Fourier analysis and can throw off the resulting indices significantly. The values of the outliers are replaced by a linearly interpolation of neighboring samples. The occurrence of outliers was found to be well below 1 %.

MODEL SENSITIVITY

Figure 4.12 shows the result of the eFAST analysis for all three simulation set-ups at two different starting epochs. The starting epochs chosen for this visualisation are 12 hours and 2 hours of remaining orbital lifetime. The epochs were selected close to reentry, yet significantly far apart in time. The model was found to be more sensitive to other uncertainty parameters close to reentry, except the atmospheric uncertainty, resulting in higher values for the sensitivities in general and values further outside the dummy's range. The time dependency and sensitivities at earlier epochs will be analysed in more detail in the next section.

Figure 4.12 shows the first-order and total-order sensitivity indices for each parameter and each set-up. The different set-ups are distinct by the different colors, where the first-order sensitivity index is hatched. Moreover, by default the total-order sensitivity index is always equal or greater than the first-order sensitivity.

It is immediately clear from Fig. 4.12 that for any set-up at any starting epoch, the simulation is most sensitive to the atmospheric density, ρ. For this reason the bars of

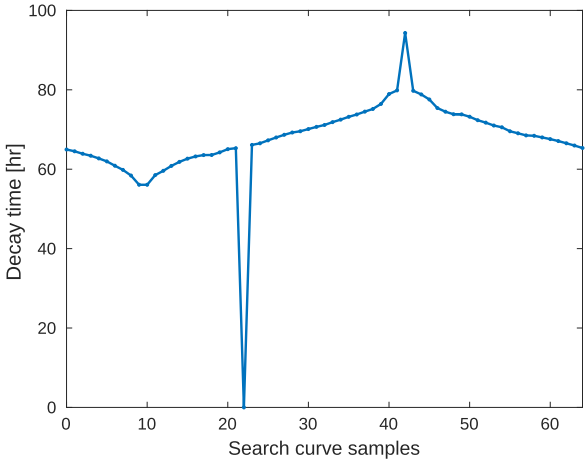

Figure 4.11: Example of two types of outliers in the simulation output results along a single search curve for the radial velocity.

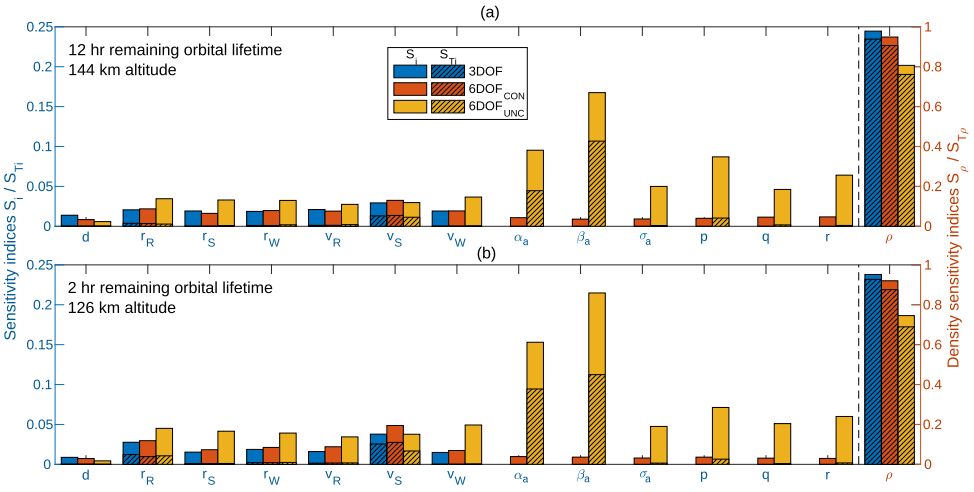

Figure 4.12: Sensitivity indices of the uncertainty parameters for various simulation set-ups at two different starting epochs: 12 hours (a) and 2 hours (b) remaining orbital lifetime.

the remaining parameters are shown on a scale that is four times smaller. Two factors diminish the sensitivity of the predictions to the atmospheric density: the remaining orbital lifetime (less time is spent in the atmosphere) and the growing influence of other parameters. The atmospheric density sensitivity is almost completely made up of the first-order sensitivity index, confirming that the atmospheric density has a very direct contribution to the reentry predictions.

The sensitivity of the dummy parameter is indicated as d in the figure. Using the increased number of samples, false first-order sensitivities were reduced to negligible values. Increasing the number of samples does not significantly reduce the total-order sensitivity, but primarily affects its precision. At the selected number of samples the sensitivity indices of the dummy parameter were consistently $S_d < 0.0005$ and $S_{T_d} < 0.01$. Convergence of these values was further confirmed by performing t-tests on the indices. Moreover, it was found that values of dummy sensitivities tend to decrease with the introduction of additional parameters and shorter propagation times. This can be seen in the figure, where the S_{T_d} for the uncontrolled 6DOF set up at 2 hours is smallest.

Amongst the translational parameters, the along-track velocity component is consistently found to be the primary first-order driver of the final uncertainty. The radial-position component is the second most influential translational parameter. Although these two parameters are known to be highly correlated, their sensitivities differ due to the magnitude and bias of their uncertainty. The sensitivity indices of both parameters also increase closer to reentry and will be further investigated in the next section.

For the rotational parameters of the controlled reentry, the first-order sensitivity indices are negligible and the total-order indices are at the threshold of the dummy parameter's level. Therefore, these sensitivities should be considered non-significant from zero. The insignificance of the rotational parameter is caused by their small initial uncertainties and the rotational control. Regarding the other parameters, the sensitivities of the controlled 6DOF and 3DOF set-ups are very similar.

For the uncontrolled 6DOF set-up the aerodynamic angles α_a and β_a were found to be the most influential parameters. The lesser significance of σ_a can be explained by the high-degree of rotational symmetry GOCE around the X-axis. The larger influence of β_a is due to the slightly larger projected area in the XZ-plane, compared to the XY-plane. The minor first-order sensitivity to the initial pitch and yaw rates (q and r, respectively), can be attributed to their small initial values and aerodynamic stability of GOCE. Conversely, the roll has a significant first-order sensitivity and the highest total-order of the rotational rates.

From the uncontrolled case it can also be seen that introduction of additional significant parameters yields an increase in the total-order sensitivity of parameters with weak first-order sensitivities. It is difficult to assign the true significance to such parameters and this primarily demonstrates the inter-dependency of translational and rotational state.

TIME DEPENDENCY

Previously, it was already shown that the sensitivity indices at 12 hours and 2 hours of remaining orbital lifetime are slightly different. To investigate the time dependency of these parameters in more detail the analysis is repeated for other starting epochs,

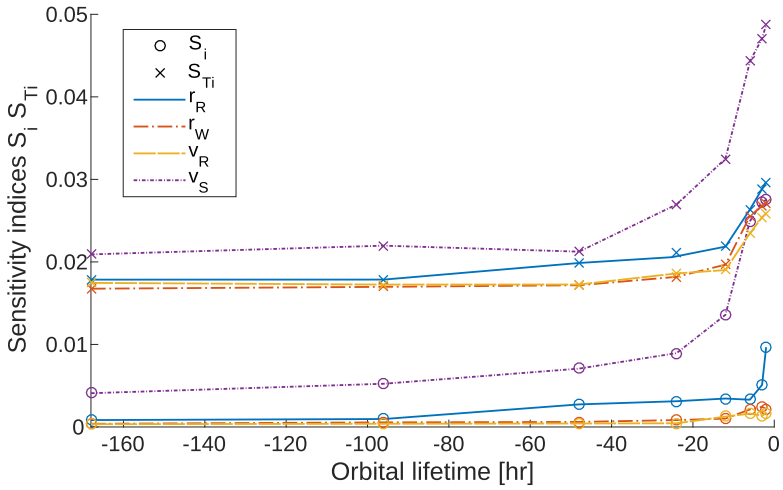

Figure 4.13: Sensitivity of all non-significant translational parameters of the controlled 6DOF model with respect to time.

namely at 168, 96, 72, 48, 24, 12, 6, 3, and 2 hours of remaining orbital lifetime. Figure 4.13 shows the time evolution of the sensitivity indices. Only the parameters with non-significant sensitivities are shown. The sensitivity indices of the atmospheric density are not shown in the figure. Its sensitivity indices slowly decrease as the others increase, starting at $S_\rho = 0.9563$ and $S_{T\rho} = 0.9967$ at 168 hours.

Figure 4.13 confirms the importance of the along-track velocity component, followed by the radial position. The radial position, however, converges to the other uncertainties (the cross-track position and radial velocity) for increased orbital lifetime, while the along-track velocity remains clearly the dominant parameter in this model at all epochs.

Overall, the sensitivity (both first and total order) of the predictions grows sharply as the orbital lifetime decreases. In practice, this effect is expected to be only larger, as the magnitude of the uncertainty in these parameters also increases close to reentry, due to the growing influence of disturbances (such as the atmospheric density) on the orbit determination.

4.4.5. Prediction Comparison

Apart from the final decay message, seven TIP messages were released for GOCE at various epochs prior to reentry. The SDO has similarly performed several predictions prior to reentry. SDO predictions started on October 23, 2013, with the assumption that the attitude controller would fail for a 20 mN drag threshold, resulting in tumbling motion. These early predictions placed the reentry at around November 6. From November 1, 2013, the threshold was raised to 50 mN. Later, the case where the attitude controllers would fail only very late into the reentry was considered [71]. Only the predictions resulting from this latter case are compared.

For the 6DOF predictions, it is chosen to start the reentry predictions at common TIP moments prior to the true reentry epoch; these are 2h, 3h, 6h, 12h, 1d, 2d, 3d, 4d, and

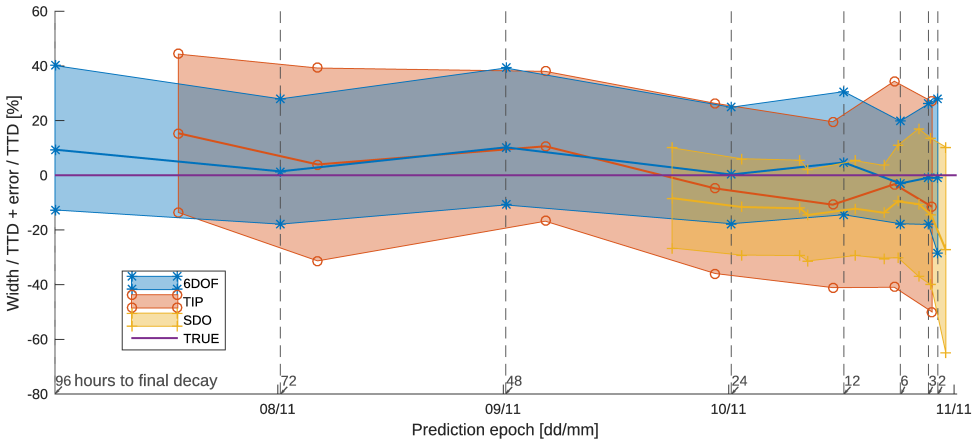

Figure 4.14: Comparison of 6DOF with TIPs and SDO reentry predictions for several prediction epochs.

7d prior to the true decay epoch. The decay-time distribution was estimated using KDE. A 2.5σ confidence interval was used to estimate the bounds. This value was chosen for comparison against TIPs and SDO predictions. Reference [57] shows that TIPs range from 93 % to 98 % confidence, depending on the orbital lifetime. Similarly, the SDO windows have 2σ confidence based on multiple predictions over only 15 reentry campaigns [54]. Using 2σ bounds would likely be too optimistic, while 3σ is not comparable to the confidence associated with the other predictions.

Figure 4.14 compares the resulting predictions. The horizontal axis corresponds to date of prediction, and the vertical axis to the prediction error as a percentage of TTD. For each prediction the confidence interval and median is indicated. As a general trend the relative prediction window (as a percentage of the TTD) remains roughly constant. The 6DOF, TIP, and SDO intervals are on average 46 %, 65 %, and 43 % wide, respectively. All are thus wider than the 40 % rule of thumb.

The windows for the TIPs were on average 41 % wider than for 6DOF. A true comparison with the TIP window, of course, depends on the confidence level of the windows, for which only empirical values are available from literature. As the width of the TIP is significantly more than the 40 % described in those studies, it is assumed that the method for determining the window has changed. A true comparison is therefore very hard to make. Nonetheless, the confidence level chosen for the 6DOF windows is likely higher than TIPs and SDO predictions, while providing windows of the same order or much less. These relatively small widths, while providing higher confidence for statistical 6DOF can be attributed to the attitude controller and improved atmospheric uncertainty modeling.

For all predictions the median of the 6DOF is found to be closer to the true reentry epoch, compared to the TIP midpoints and SDO's medians. For the 6DOF predictions the distributions are slightly asymmetric, where the median is on average located at 7 3 % (in terms of the total distribution width) from the midpoint towards the lower bound. The asymmetry is found to be characteristic for decay-time distributions, where long re-

entries are statistically more likely than short re-entries.

Except for the final three predictions (starting at 6, 3, and 2h, respectively), the median overshoots the true decay epoch. A maximum of 10 % (about 5 hours) is observed for the prediction made at 48 hours prior. This offset was already observed in the previous results presented. The median of all SDO predictions seems to be earlier than the true reentry epoch. The earlier medians can be explained by the modeling of the uncontrolled motion using the drag coefficient obtained from SCARAB, without accounting for the lower atmospheric densities.

4.5. CONCLUSIONS

The decay-time distribution accuracy for the Gravity field and steady-state Ocean Circulation Explorer (GOCE) satellite is dominated primarily by systematic errors in atmospheric density and attitude control, while its precision is dominated by the atmospheric uncertainty. To a lesser degree, the precision is also affected by the initial translational uncertainty.

The study proposed an uncertainty model for the atmospheric density to account for (systematic) modeling errors in the atmospheric and aerodynamic models. Subsequently, two different uncertainty estimation methods were presented for Global Positioning System (GPS) and Two-line Elements (TLE) derived states. The resulting approach produces accurate results for dealing with a biased atmosphere and/or aerodynamic model. By analysing the density-modeling error from GPS-derived non-gravitational accelerations, a better estimate of the density uncertainty could be obtained. For TLEs similar results could be obtained, albeit at a much coarser temporal resolution. Considering the importance of the atmospheric uncertainty, additional modeling (especially of its evolution) should improve results even further.

The attitude control is found to significantly affect the median of the reentry predictions. The predicted median for a remaining orbital lifetime of 48 hours was found to lie anywhere between 17 and 55 hours depending on when the controller was assumed to be saturated. Therefore, it is important to properly account for this control. By modeling the attitude control and motion in six degrees-of-freedom (6DOF) simulator, it is not necessary to assume a constant drag coefficient and introduce any discontinuities to this value. The assumptions on controller saturation could be reduced to maximum torques, which were sourced from literature. Finally, systematic errors and uncertainties in the atmospheric density were included throughout the simulation.

The effect of atmospheric uncertainty on the reentry prediction uncertainty for GOCE is found to outweigh all other contributions in the uncertainty modeling effort. Halving the atmospheric uncertainty results in a halving of the final decay-time uncertainty. Moreover, the difference between TLE-derived and GPS-derived initial translational uncertainty results in a 35 % improvement, despite GPS being up to four orders of magnitude more precise. In previous studies the initial rotational uncertainty was found to be another main driver for the precision, but the attitude control mostly negated this influence.

Two simplified error propagation strategies were examined. Propagating only the translational motion of a single nominal trajectory resulted in significant overshooting of the decay epoch, even for such a strongly attitude controlled satellite as GOCE. A single

6DOF propagated nominal state, however, showed good agreement with the median of the uncertainty distribution for GOCE. This agreement is due to the relatively unbiased and symmetrical initial uncertainty distributions. The empirical uncertainty window, as used by the Tracking and Impact Predictions (TIPs), does not capture the asymmetry of the uncertainty distribution. Moreover, the window width is not a constant factor of the remaining orbital lifetime. Although these effects can be included in an empirical approach, it needs to be stressed that it remains based on populations of historic re-entries and does not necessarily correspond to individual future cases. Approaching the lower and upper limits of the uncertainty distribution by varying the ballistic coefficient, produced better bounds. Varying the ballistic coefficient by ±12 % produces limits with the best agreement to the statistical distributions. The case of ±20 % produced far too conservative results. The approach showed clear asymmetry, although slightly too much, resulting in a too conservative upper bound. This suggests that perhaps different percentages should be used for the lower and upper bounds. The bounds were found to be very sensitive to these values. Selecting the best value(s) is unfortunately not straightforward and likely depends on the satellite, modeling, and also the orbital lifetime. The approach is only recommended when using a high-fidelity (6DOF) propagation model and when many samples are infeasible.

The sensitivity analysis further demonstrates that the atmospheric uncertainty is the primary driver of the decay-time distribution. For the controlled reentry the along-track velocity and radial position are of secondary importance. The first-order and total-order sensitivity of these parameters is on the order of 0.01-0.03 and 0.03-0.05, respectively. The significance of these parameters is non-neglible for performing accurate reentry predictions. Moreover, the sensitivity indices increase sharply as a function of the remaining orbital lifetime. In addition, the estimation error of these parameters also grows close to the reentry epoch.

From the sensitivity analysis of the controlled 6DOF set-up it can be concluded that the dimensions of the uncertainty model can be greatly reduced, at no significant loss of accuracy. The entire rotational uncertainty and several position and velocity components can be ignored. This should improve the performance of the reentry simulations significantly. It is, however, not possible to extend these conclusions for reentry simulations in general. Especially not on the importance of rotational uncertainty.

For the uncontrolled reentry set-up it was shown that the rotational parameters were more influential than the translational parameters. In this study, the angles of attack and sideslip were found to be the dominant rotational parameters. The ranking of the rotational parameters and absolute values of the sensitivity indices is highly dependent on the initial rotational uncertainty and the aerodynamic characteristics of the satellite. The rotational uncertainty is expected to play an even larger role for other bodies, considering GOCE's unique aerodynamic shape and the very small initial rotational uncertainty. To improve the efficiency of the MC error propagation in general a more intelligent sampling strategy should be employed that takes into account the sensitivity of the uncertainty parameters.

For the 6DOF reentry predictions of GOCE, the median was found consistently closer to the true decay epoch than neighboring TIPs and predictions by the Space Debris Office (SDO) of the European Space Agency. Moreover, the statistically obtained windows

are on average41 % narrower than the TIP windows. The 6DOF and SDO predictions are found to be of comparable relative width. A true comparison on the width is difficult as the associated confidence can only be empirically determined, for which not enough cases have been studied. Nonetheless, statistical 6DOF predictions provide smaller or equal windows with a high confidence for GOCE. For non-controlled slender bodies, such as rocket bodies, the windows at the same confidence level will likely be much wider.

The results demonstrate that by modeling the uncertainties per object and performing proper error propagation, the resulting distributions are tailored specifically to the reentry under consideration. It is recommended to perform statistical 6DOF reentry predictions for objects for which aerodynamic models are available or can be easily constructed.

5

REGULARISED METHODS FOR HIGH-EFFICIENCY PROPAGATION

Geul, J., Mooij, E. and Noomen, R.

Published [1] in Proceedings of the AAS/AIAA Astrodynamics Specialist Conference, Vol. 156, No. 1, August 9-13, 2015, Vail (CO), USA, Paper AAS 15-697, pp. 4105–4124, 2016

Although regularised propagation methods have a good performance (accuracy versus evaluations), they suffer from a number of practical difficulties, such as propagation to a fixed time, making them ill-suited for practical applications. Several methods that address these limitations are proposed, thoroughly discussed, and analysed on diverse test cases. Dromo outperforms the conventional propagation methods significantly. It is shown that regularised methods, through some adaptations, can be successfully applied to different orbit problems. The proposed method is recommended especially for computationally demanding problems.

5.1. INTRODUCTION

Numerical integration has become the standard for solving problems in orbital mechanics, in favour of analytical and semi-analytical techniques [86]. Cowell's method, however, has the major drawback of being far less efficient, due to the many computations at intermediate time steps. Regularised propagation methods offer a significant reduction in steps for the same numerical accuracy [87, 88]. Through the transformation of the independent variable and equations of motion (EOMs), the numerical and dynamical stability is improved.

Research in satellite orbit propagation is mainly focused on the modelling of different perturbations. These models present the dominant contribution in terms of ac-

[1] Minor modifications have been made for this thesis.

curacy. However, these more advanced models come at a computational price. Especially when the propagation of a large catalogue of objects is concerned, the computational efficiency becomes crucial. Recently, regularisation methods have regained momentum [89–96].

Regularised methods, nonetheless, have only been scarcely adopted for solving real orbit problems. This can likely be attributed to the more difficult implementation and practical issues that arise from the transformations of the independent variable (*i.e.,* time) and the EOMs. Especially, propagating to a fixed time presents a major practical challenge for such methods, as time has become a dependent variable through the time transformation. Several solutions are proposed, thoroughly discussed, and analysed. The proposed solution are implemented for Dromo [95], a specific regularised propagation method. Dromo features only eight EOMs (formulated as variations of parameters (VOP) elements) and a separate treatment of perturbations that can and cannot be derived from a potential. Dromo with the proposed adaptations is compared against two (standard) propagation methods, namely Cowell's method and Modified Equinoctial Elements (MEEs) [97]. The methods are compared for a number of representative test cases.

The aim of the thesis is to analyse how regularised methods compare to conventional methods, when their practical limitations have been addressed, and to identify uses for regularised methods. The focus is mainly on efficiency, defined as computational cost over accuracy.

First, regularisation and the formulation of Dromo are first explained. Second, the methodology of the proposed solutions is given. Third, the experimental set-up is explained, including the test approach, problems, and cases. Fourth, the results are presented and discussed. Finally, the main conclusions and recommendations are given.

5.2. BACKGROUND

The theory of regularised propagation is introduced, after which the theory of Dromo is given.

5.2.1. REGULARISED PROPAGATION

Regularisation aims to remove singularities and dynamical instability from the EOMs, leading to less integration errors and more efficient integration. It commonly follows a two-step approach. First, a transformation of the independent variable is introduced. The general form of this transformation is known as the Sundman transformation, as given by Equation 5.1. The relationship between the fictitious time s and physical time t is chosen such that for a constant step size $h = \Delta s$, $t \to 0$ as $r^m \to 0$. Considering a highly eccentric orbit, the step size will become very small at pericentre and very large at apocentre. Analytic step-size regulation is achieved when the truncation becomes uniform at each time step. Second, the EOMs are transformed into a more suitable set of parameters for describing orbital motion, further improving the numerical properties [98].

$$\mathrm{d}s = A\frac{\mathrm{d}t}{r^m} \tag{5.1}$$

where A is a scaling factor and m the order of the time transformation. The optimal

combination of m and A will depend on the type of orbit, integrator, and perturbations.

Additionally, the regularised EOMs can be reformulated through the theory of VOP. The transformed parameters, referred to as (orbital) elements, are chosen such that they are constant for idealised motion (e.g., two body). As the elements are constant (or linear) for idealised motion, only the perturbations have to be integrated.

5.2.2. DROMO AND COMPARISON OF REGULARISED METHODS

Many different regularised methods exist. The most popular classical methods are Kustaanheimo-Stiefel (KS) [99] and Sperling-Burdet (SB) [100]. Recently, there has been development towards leaner methods that take advantage of quaternions [89–96]. In particular, Dromo seems very interesting and is a VOP method derived from the Burdet-Ferrándiz [101] regularization. Dromo employs only eight EOMs, which is close to non-regularised methods (often six) and less than other regularised methods: Sperling-Burdet and Kustaanheimo-Stiefel feature 12 and 10 differential equations, respectively [102]. Other important advantages include: non-degenerate quaternions, perturbing accelerations in the orbital frame, unique formulation for all perturbed conics, and a separate treatment of perturbing forces which are partially or fully derivable from a potential [95].

A number of classical and modern methods are compared in Table 5.1. The orbit is highly eccentric eccentric ($e = 0.95$ and $r_p = 6800\,\text{km}$) and is often used as a benchmarking problem in literature [88, 103]. Stiefel-Scheifele (SS) represents the benchmark for this problem. The table reports the final position (x, y, and z) after 288.127 689 41 mean solar days (roughly 50 revolutions), the number of steps per revolution (steps/rev), and the absolute error with respect to the benchmark. Additional results for Dromo, MEEs, and Cowell were obtained. The unified state model (USM) [103, 104] uses only seven ODEs (which can be reduced to six) based on the velocity hodograph and quaternions.

It can be seen that on the test problem, all regularised methods (SB, KS, and Dromo) perform much better than the others. This is not at all surprising as the orbit is highly eccentric. Dromo is found to be a bit more expensive than KS on this problem. This is confirmed in Ref. [96], which further shows that Dromo is superior over the other methods for problems with lower eccentricities ($e = 0, 0.3, 0.7$).

5.2.3. DROMO FORMULATION

Dromo (derived from Greek, meaning: a running or race) was initially developed in Ref. [93]. In Ref. [95], the method for a separate treatment of perturbing forces which are derivable from a potential is extended. A time element was finally introduced in Ref. [96].

Dromo employs eight elements: three for orbital shape and motion in the orbital plane ζ_{1-3}, four to describe the orientation ζ_{4-7}, and one related to time ζ_0.

Note that all quantities in Dromo are non-dimensional, by introducing units for time and length as n_0^{-1} and R_0, respectively. Here R_0 is the initial radius and n_0 the initial circular mean motion (i.e., $n_0 = n(a = R_0) = \sqrt{\mu / R_0^3}$).

The perturbations are expressed in the orbital frame. This is convenient for many perturbations (e.g., drag, thrust, etc.). Moreover, perturbations derivable and non-derivable from a potential are treated separately, allowing for propagation that is consistent

Table 5.1: Comparison of several methods for the oblate Earth plus Moon after 288.12768941 days.

	SS [88]	SB [88]	KS [88]	Cowell[a] [88]
x [km]	−24219.050	−24218.818	−24219.002	−24182.152
y [km]	227962.106	227961.915	227962.429	227943.989
z [km]	129753.442	129753.343	129753.822	129744.270
Steps/rev	500	62	62	240
Error [km]		0.318	0.501	42.5

	Dromo	Cowell[b]	MEE	USM [103]
x [km]	−24218.829	−24256.391	−24256.980	−24219.049
y [km]	227961.980	227980.068	227979.117	227962.106
z [km]	129753.414	129762.509	129761.798	129753.442
Steps/rev	113	453	188	372
Error [km]	0.256	42.4	42.4	42.1

[a] Note that Cowell's method here indicates the formulation in Ref. [105], which uses the total energy as an independent parameter.
[b] Note that Cowell's method here indicates the Cartesian formulation.

with total energy. The total perturbing acceleration $\mathbf{f}$ is given by:

$$\mathbf{f} = \mathbf{P} + \nabla R = \mathbf{P} - \frac{\partial R(t,\zeta)}{\partial \mathbf{r}_{orb}} \tag{5.2}$$

where $\mathbf{P}$ is the sum of all non-potential accelerations, R the total perturbing potential, ∇ the gradient operator, and $\mathbf{r}_{orb}$ represents the orthonormal basis $\{\hat{\mathbf{i}}, \hat{\mathbf{j}}, \hat{\mathbf{k}}\}$, given by $\{\frac{\mathbf{r}}{r}, \hat{\mathbf{k}} \times \hat{\mathbf{i}}, \frac{\mathbf{h}}{h}\}$, where the angular momentum is $\mathbf{h} = \mathbf{r} \times \mathbf{v}$. Similarly, the perturbing accelerations $\mathbf{f}$ and $\mathbf{P}$ are composed of the radial, transverse, and normal components.

TIME TRANSFORMATION

The time is transformed from physical time t to fictitious time ϕ, using a Sundmann time transformation of order two:

$$\frac{\mathrm{d}t}{\mathrm{d}\phi} = \frac{r^2}{\tilde{h}} = \frac{1}{\zeta_3 s^2} \tag{5.3}$$

where $A = \tilde{h}$ and $m = 2$. ζ_3 and s will be defined in the next section. The pseudo-angular momentum $\tilde{h}$ is defined as

$$\tilde{h} = r\sqrt{2\left(\mathscr{E} + \frac{1}{r}\right) - \left(\frac{\mathrm{d}r}{\mathrm{d}t}\right)^2} \tag{5.4}$$

where $\mathscr{E}$ is the total orbital energy and the relation between $\tilde{h}$ and h is $\tilde{h} = \sqrt{h^2 + 2r^2 R}$.

The independent variable ϕ can be considered as a perturbed version of the true anomaly ν, and is, therefore, also referred to as the pseudo true-anomaly. ϕ varies linearly with ν with an additional angular drift γ, such that $\Delta\phi = \Delta\nu + \gamma$. γ is defined as:

$$\gamma = \Delta\omega + \int_{\Omega_0}^{\Omega} \cos i \, \mathrm{d}\Omega + 2\int_0^t \frac{R}{\tilde{h}+h}\mathrm{d}t \tag{5.5}$$

The numerical solution can be further improved by removing time t also from the EOMs. Looking at Equation 5.3 it can be seen that even for unperturbed motion the physical time does not necessarily vary linearly with respect to ϕ. Due to the time transformation, the problem has been partly moved to EOMs, giving rise to a number of complications. First, the integration of physical time leads to errors in approximating time itself. Second, large variations of the time derivative can present a bottleneck, driving the integration accuracy of the entire state. Lastly, the time accuracy directly influences the state accuracy when the state at a certain epoch is desired.

Two different alternative time formulations are possible: the linear and constant time elements [96]. In total this gives three options for the expression of time. These options will from hereon be referred to as non-dimensional physical time t, linear time element ζ_{0_l}, and constant time element ζ_{0_c}.The relations between time t and the time elements ζ_{0_l} and ζ_{0_c} are given by:

$$\zeta_{0_l} = t - \frac{V_r}{2\mathscr{E}\zeta_3 s} - \frac{1}{\mathscr{E}\sqrt{-2\mathscr{E}}}\arctan\left(\frac{V_r}{s+\sqrt{-2\mathscr{E}}}\right) \tag{5.6}$$

$$\zeta_{0_c} = \zeta_{0_l} - a^{3/2}\phi \tag{5.7}$$

where V_r is the radial velocity, s the pseudo-transverse velocity, and ζ_3 the inverse pseudo angular-momentum, to be introduced in the next section. The differential equations are:

$$\frac{\mathrm{d}\zeta_{0_l}}{\mathrm{d}\phi} = a^{3/2}\left[1 + \frac{\mathrm{d}\mathscr{E}}{\mathrm{d}\phi}\left(6a\arctan\left(\frac{V_r}{k_4+k_3}\right)+k_1\right) + \left(\frac{f_r}{\zeta_3 s} - 2R\right)k_2\right] \tag{5.8}$$

$$\frac{\mathrm{d}\zeta_{0_c}}{\mathrm{d}\phi} = a^{3/2}\left[\frac{\mathrm{d}\mathscr{E}}{\mathrm{d}\phi}\left(6a\arctan\left(\frac{V_r}{k_4+k_3}\right) - 3a\phi + k_1\right) + \left(\frac{f_r}{\zeta_3 s} - 2R\right)k_2\right] \tag{5.9}$$

where $\frac{\mathrm{d}\mathscr{E}}{\mathrm{d}\phi}$ is the rate-of-change of the total energy and f_r the radial component of the perturbing acceleration. k_{1-4} are relations that simplify the notation and are defined to be:

$$k_1 = \frac{\sqrt{a}V_r}{s^2}\left(\frac{\zeta_3+s}{k_4} + \frac{2k_3}{\zeta_3} + 1\right)$$

$$k_2 = \frac{1}{s^2}\left(\frac{k_4}{\zeta_3} + \frac{k_3}{k_4} + \frac{V_r^2}{k_4 s}\right)$$

$$k_3 = \zeta_1\cos\phi + \zeta_2\sin\phi$$

$$k_4 = \zeta_3 + \sqrt{-2\mathscr{E}}$$

SHAPE AND ORIENTATION

As mentioned before the set ζ_{1-7} can be split up into elements concerning the shape and dynamics ζ_{1-3}, and the orientation of the orbital plane ζ_{4-7}. The first three elements are obtained by introducing the generalised orbital element $\zeta_3 = \tilde{h}^{-1}$, from which ζ_1 and ζ_2 follow as integration constants. The remaining four constants of motion ζ_{4-7} describe the orientation and are closely related to quaternions.

The ODEs of the elements with respect to the independent parameter are

$$\frac{\mathrm{d}\zeta_1}{\mathrm{d}\phi} = \frac{\sin\phi}{s}\left(\frac{f_r}{\zeta_3 s} - 2R\right) - \left(\frac{s}{\zeta_3} + 1\right)\cos\phi\frac{\mathrm{d}\zeta_3}{\phi} \tag{5.10}$$

$$\frac{\mathrm{d}\zeta_2}{\mathrm{d}\phi} = \frac{\cos\phi}{s}\left(2R - \frac{f_r}{\zeta_3 s}\right) - \left(\frac{s}{\zeta_3} + 1\right)\sin\phi\frac{\mathrm{d}\zeta_3}{\phi} \tag{5.11}$$

$$\frac{\mathrm{d}\zeta_3}{\mathrm{d}\phi} = -\frac{1}{s^4}\left[V_r\zeta_3 s\left(2R - \frac{\zeta_3 s}{s+\zeta_3}\frac{\partial R}{\partial\zeta_3}\right) + V_t P_t + \frac{\partial R}{\partial t}\right] \tag{5.12}$$

$$\frac{\mathrm{d}\zeta_4}{\mathrm{d}\phi} = \frac{1}{s}\left[\frac{f_n}{\zeta_3 s V_t}(\zeta_7\cos\Delta\phi - \zeta_6\sin\Delta\phi) + \zeta_5(V_t - s)\right] \tag{5.13}$$

$$\frac{\mathrm{d}\zeta_5}{\mathrm{d}\phi} = \frac{1}{s}\left[\frac{f_n}{\zeta_3 s V_t}(\zeta_6\cos\Delta\phi + \zeta_7\sin\Delta\phi) - \zeta_4(V_t - s)\right] \tag{5.14}$$

$$\frac{\mathrm{d}\zeta_6}{\mathrm{d}\phi} = -\frac{1}{s}\left[\frac{f_n}{\zeta_3 s V_t}(\zeta_5\cos\Delta\phi - \zeta_4\sin\Delta\phi) - \zeta_7(V_t - s)\right] \tag{5.15}$$

$$\frac{\mathrm{d}\zeta_7}{\mathrm{d}\phi} = -\frac{1}{s}\left[\frac{f_n}{\zeta_3 s V_t}(\zeta_4\cos\Delta\phi + \zeta_5\sin\Delta\phi) + \zeta_6(V_t - s)\right] \tag{5.16}$$

where the pseudo-transverse s, transverse V_t, and radial velocity V_r are given by

$$s = \zeta_3 + \zeta_1\cos\phi + \zeta_2\sin\phi \tag{5.17}$$

$$V_t = \sqrt{s^2 - 2R} \tag{5.18}$$

$$V_r = \zeta_1\sin\phi - \zeta_2\cos\phi \tag{5.19}$$

It is important to note that $\Delta\phi$ in Eqs.(5.13-5.16) represents the difference between the current and initial value $\Delta\phi = \phi - \phi_0$, and not the step size. The initial value of ϕ_0 can be arbitrarily chosen when the initial Dromo state is constructed. A common choice for ϕ_0 is the initial true anomaly $\phi_0 = \nu_0$ or just $\phi_0 = 0$.

Alternatively, when the perturbations are mainly conservative, the third element ζ_3 can be replaced by the total energy $\mathscr{E}$, replacing Equation 5.12 by

$$\frac{\mathrm{d}\mathscr{E}}{\mathrm{d}\phi} = \frac{1}{\zeta_3 s^2}\left(uP_r + P_t\sqrt{s^2 - 2R} + \frac{\partial R}{\partial t}\right) \tag{5.20}$$

where ζ_3 can then be obtained through the following equation:

$$\zeta_3 = \sqrt{\zeta_1^2 + \zeta_2^2 - 2\mathscr{E}} \tag{5.21}$$

In conclusion, only eight first-order ODEs need to be numerically integrated with Dromo. Different options for a set of eight equations have been present, these are: one related to time (Equation 5.3, (5.8), or (5.9)), three related to the shape of the orbit (Eqs.

(5.10), (5.11), and (5.12) or (5.20)) and four related to the orientation of the orbital plane (Eqs. (5.13) to (5.16)). The Dromo state thus consists of the following eight elements

$$\zeta = [t \text{ or } \zeta_{0_l} \text{ or } \zeta_{0_c}, \zeta_1, \zeta_2, \zeta_3 \text{ or } \mathscr{E}, \zeta_4, \zeta_5, \zeta_6, \zeta_7]$$

By default (unless stated otherwise) the following set is used:

$$\zeta = [\zeta_{0_c}, \zeta_1, \zeta_2, \mathscr{E}, \zeta_4, \zeta_5, \zeta_6, \zeta_7]$$

5.3. METHODOLOGY

The formulation of Dromo presented has a number of practical limitations. These limitations are generally true for any regularised method. To facilitate the implementation of these methods, the issue of propagating to a final time is considered. Although this treatment considers time, the methodology presented can in fact be used for finding the final state at any value of one of the dependent parameters, such as the orbital altitude (in case of re-entry) or any of the instantaneous orbital elements.

5.3.1. FIXED TIME PROPAGATION

Although the time transformation has many advantages, the major drawback is that time has become a dependent parameter and the relationship between both is non-linear. Therefore, propagating to a certain epoch is not straightforward. The final value of the independent parameter ϕ_f corresponding with the final physical time t_f can only be obtained numerically. This presents a problem for applications that require the state at an exact time, e.g., orbit determination.

The approximations of the final independent parameter and dependent time are in this section denoted as $\hat{\phi}_f$ and $\hat{t}_f$.

The procedure of propagating to a final time has a number of drawbacks. First of all, finding the corresponding $\hat{\phi}_f$ can be computationally expensive, as will be demonstrated. Secondly, since $\hat{\phi}_f$ is only approximated and thus differs from the true unknown value, also the integrated $\hat{t}_f$ will not be exactly the desired t_f. Lastly, a small variation (or error) in $\hat{\phi}_f$ can lead to a very large deviation in $\hat{t}_f$. This sensitivity is illustrated in Figure 5.1, where a change of about 0.35 rad in ϕ leads to a variation in t of almost 250 000 s. The error in time translates into additional state errors. It is therefore important to find a very good approximation in a computationally lean manner.

Three different solutions to this problem exist, which will be explained in more detail. Each method will be treated based on their implications on function evaluations, accuracy, and ease of implementation. To gain better insight in the differences in accuracy, the error in the final time can be split up as follows:

$$\epsilon = |t_f - \hat{t}_f| = \epsilon_n + \epsilon_a + \epsilon_e \tag{5.22}$$

where ϵ_n is the numerical error due to the numerical integration (containing both round-off and truncation errors) and is dependent on the integration scheme. ϵ_a is the error due to approximation of $\hat{\phi}_f$ by the different methods, such that $|t(\hat{\phi}_f) - t(\phi_f)| = \epsilon_a$. This error stems from convergence tolerance (if iterations are required). It has to be noted that this tolerance should be set individually from the integrator tolerances. Finally, ϵ_e is

an additional estimation error introduced by the methods in finding $\hat{\phi}_f$. The last source is not immediately intuitive, but will become clear. The error due to estimation is defined as:

$$\epsilon_e = |\hat{t}_f(\text{integrator} + \text{estimator}(t_f)) - \hat{t}_f(\text{integrator}(\hat{\phi}_f))| \tag{5.23}$$

where the first $\hat{t}_f$ is the result of the integration and estimation procedure combined and the second $\hat{t}_f$ is when the integration is repeated (without the estimation procedure) using the estimate of the independent parameter $\hat{\phi}_f$. The difference between these two is the impact of the estimation.

HOUSEHOLDER

Householder methods are a class of iterative root-finding algorithms. Newton's method (sometimes also Newton-Raphson) and Halley's method are first-order and second-order Householder members, respectively. Newton only uses the function gradient, while Halley uses additional second-order derivative information. Halley's method is considered to be more stable and generally faster, as it has a cubic upper bound for the rate of convergence, as opposed to quadratic for Newton's method. The scheme is initialised with an initial guess $\hat{\phi}_{f_0}$, which is updated after each iteration until convergence to within a set tolerance. The iterative schemes for Newton's and Halley's method are given by:

$$\hat{\phi}_{f_{n+1}} = \hat{\phi}_{f_n} - \frac{f}{f'} \qquad \hat{\phi}_{f_{n+1}} = \hat{\phi}_{f_n} - \frac{2ff'}{2f'^2 - ff''} \tag{5.24}$$

where the derivatives are found using Eqs. (5.3) and (5.17):

$$f = t_n - t_f \tag{5.25}$$

$$f' = \frac{\mathrm{d}f}{\mathrm{d}\hat{\phi}} = \frac{1}{\zeta_3 s^2} \tag{5.26}$$

$$f'' = \frac{\mathrm{d}^2 f}{\mathrm{d}\hat{\phi}^2} = \frac{-2(-\zeta_1 \sin\hat{\phi}_{f_n} + \zeta_2 \cos\hat{\phi}_{f_n})}{\zeta_3 s^3} \tag{5.27}$$

This approach is both very accurate and expensive. As the integration is restarted for each new guess $\hat{\phi}_f$, the error due to estimation is not present ($\epsilon_{estimation} = 0$). However, the number of function evaluations can be high: roughly equal to the number of iterations times number of evaluations necessary to propagate a single trajectory. The number of iterations depends on the quality of the initial guess and the required level of convergence. Also, convergence is not guaranteed.

BISECTION

The second method uses bisection to successively approximate the ϕ_f. This is a simple root-finding method that repeatedly bisects an interval. As the maximum bisection interval is limited to the maximum step size, the state is first propagated until it overshoots

the target t_f. The step is then reverted to the last point corresponding to ϕ_n, such that $t_n < t_f$. The step size is subsequently halved and the procedure repeated.

The approach is very simple to implement. The convergence is linear, which is slower than the other methods. However, the procedure requires no derivatives, initial guesses, and restarts. Therefore, requiring only a moderate number of additional function evaluations. However, the accuracy is only moderate, as additional numerical errors are introduced in the process, through the increasingly smaller steps.

HERMITE INTERPOLATION

The third and final method solves ϕ_f using interpolation. Out of the many different choices that exist (e.g., Lagrange polynomials, splines, etc.), a Hermite polynomial is chosen. Hermite polynomials (as opposed to Lagrange/Newton polynomials) use higher-order derivative information. Here, only the states and its first-order derivatives are used. Since this method is very akin to an extrapolation polynomial used by numerical integrators, the error made will be of the same order as the integration error, making it suitable for combination with numerical integration.

The first integration step after overshoot $t_n > t_f$ is denoted ϕ_n. Along with the state at ϕ_n, a number of additional points before and after are used. The interpolation of time is illustrated in Figure 5.1. The orbit used for this example is Problem 1 and is introduced in Section 5.4.4.

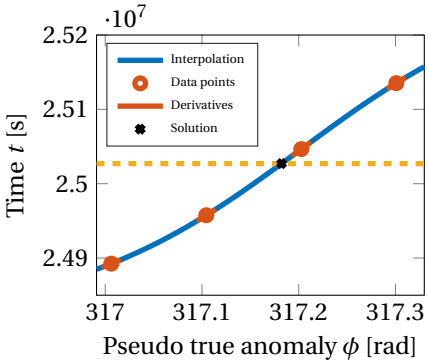

Figure 5.1: Hermite interpolation of the final time after 49.5 revolutions.

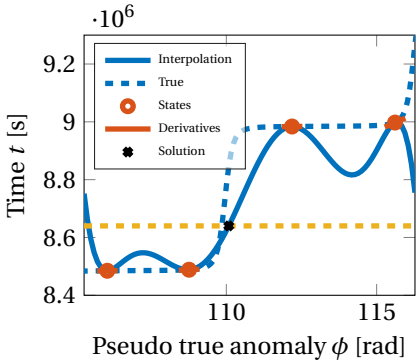

Figure 5.2: Improper interpolation of the final time due to too large step-size using time elements.

The values of the independent and dependent parameter are reduced according to Eqs.(5.28) and (5.29). For the independent parameter, it is essential for a good fit that the values are around zero. Moreover, the final time is subtracted, such that the polynomial $p(\bar{\phi}_f) = 0$ needs to be solved.

$$\bar{\phi}_i = \phi_i - \phi_n \tag{5.28}$$

$$\bar{t}_i = t_i - t_f \tag{5.29}$$

The polynomial can then be generated using the set of points $\{\bar{t}_i, \dot{t}, \bar{\phi}_i\}$. The usual way would be to (numerically) compute the divided-difference table, from which the

polynomial can then easily be found. However, it is proposed to solve the expression for the polynomial coefficients analytically as a function of the data points, such that $\mathbf{c} = f(\bar{\phi}, \bar{\mathbf{t}}, \dot{\mathbf{t}})$, making it more efficient to set-up the polynomial. Note that one such set of expression for the coefficients needs to be found for each integration order. The polynomial then becomes:

$$\bar{t} = p(\bar{\phi}; \mathbf{c}) = \sum_{i=1}^{N} c_i \bar{\phi}^{i-1} \tag{5.30}$$

The roots of the polynomial are then solved to find potential candidates for $\bar{\phi}_f$. For polynomials of up to order four, closed-form analytic solutions exist. For higher orders, the roots must be solved numerically, which are found as the eigenvalues of the polynomial's companion matrix, defined as:

$$C(\mathbf{c}) = \begin{bmatrix} 0 & 0 & \cdots & 0 & -c_1 \\ 1 & 0 & \cdots & 0 & -c_2 \\ 0 & 1 & \cdots & 0 & -c_3 \\ \vdots & \vdots & \ddots & \vdots & \vdots \\ 0 & 0 & \cdots & 1 & -c_N \end{bmatrix} \tag{5.31}$$

The number of roots (real and imaginary, including multiplicity) is equal to the polynomial order. To find the correct root, knowledge about the solution is applied to eliminate candidates. The following conditions are used to identify the proper root:

$$\bar{\phi}_f \in \mathbb{R} \qquad\qquad \bar{\phi}_{n-1} < \bar{\phi}_f < 0 \tag{5.32}$$

The final independent variable is then $\hat{\phi}_f = \phi_n + \bar{\phi}_f$.

The method is both accurate and efficient. The accuracy of the solution is driven by the fit of the polynomial alone, as the solving of the eigenvalues is exact (only round-off). Similarly, the estimation error is of the same order as the numerical errors for a single step, thus $\epsilon_{estimation} \approx 0$. The method uses even less evaluations than bisection. Lastly, no initial guess is required and the method can be applied for any parameter. The implementation, however, is perhaps the most involved of the three methods.

If the parameter is part of the state, the step-size controller of the integrator ensures that a good spacing of data points for the polynomial is obtained. However, this can not be guaranteed when the parameter is derived from the state (in case of a time element), resulting in improper interpolation of the final time. Figure 5.2 illustrates the problem of improper interpolation. Although the polynomial satisfies the state and derivative constraints, the solution for $\hat{\phi}_f$ is off. In such a case, time (instead of a time element) can be integrated around the solution. Note that the error of the interpolation can be easily obtained by integrating from ϕ_{n-1} to the estimated $\hat{\phi}_f$. Using this error, the step size can be modified and the quality of the interpolation checked in a trial-and-error approach.

5.4. EXPERIMENTAL SET-UP

The general set-up of the numerical simulation is explained below, followed by an introduction to the numerical integration techniques used. Finally the test problems are given. Dromo (with the proposed solution) is tested for the following cases:

Case A: Time-state options investigates the effects of using different options for time.

Case B: Fixed-time propagation compares the three solutions for propagating to a fixed end in terms of time and positional accuracy.

Case C: Force modelling analyses the difference between conservative and dissipative perturbations.

Case D: Numerical integrators investigates different numerical integration techniques.

Case E: Different orbits compares the effect of orbits for the test problems.

5.4.1. GENERAL SET-UP

The aim is to make the comparison between the regularised and non-regularised methods as realistic as possible. The following two important aspects ensure this.

First, Runge-Kutta Dormand-Prince 5(4) (DOPRI5) is used for all methods by default, unless stated otherwise. This integrator features step-size control, even though regularised methods could propagate with high accuracy using a fixed step-size integrator, through their analytic step-size control. However, doing so for the non-regularised methods would result in very poor performance and an unfair comparison.

Second, all problems are integrated to a fixed final time, not a pre-computed final value of the independent parameter that corresponds to the final time. This distinction is important, as it was already discussed, that integration to a final time is not straightforward with regularised methods. Usually for benchmarking the final independent parameter is first estimated with very high precision and the state is then propagated to the final value of the independent parameter instead. This approach, however, does not accurately reflect the computational costs associated with finding the final value ϕ_f.

5.4.2. ERROR AND REFERENCE POSITION

For each of the problems the orbit is integrated to the final time to obtain the final state for various numerical tolerances between 10^{-6} and 10^{-14}. The final state is converted to the Cartesian position $\hat{\mathbf{r}}$ and then compared against a reference position $\mathbf{r}$. This comparison highlights the computational effort required to reach a certain accuracy (and vica-versa). The error is computed as the minimum between the absolute and relative error:

$$\epsilon = \min\left(\|\hat{\mathbf{r}}-\mathbf{r}\|, \left\|\frac{\hat{\mathbf{r}}-\mathbf{r}}{\max(|\hat{\mathbf{r}}|,|\mathbf{r}|)}\right\|\right) \tag{5.33}$$

A reference solution is not available for most tests. Unless the motion is unperturbed, the solution has to be found numerically. For this, a solution is computed using Dromo with the householder approach. The tolerance chosen is at least one order lower than the minimum tolerance for the test.

5.4.3. FORCE MODELLING

In addition to two-body unperturbed motion, the effects of the Earth's oblateness and atmosphere are analysed. The models, introduced in more detail below, can be considered crude. However, they represent two fundamental ingredients, namely conservative potential-derived and dissipative perturbations. Therefore, they are representative for more advanced models and will suffice in highlighting differences among the methods.

OBLATENESS

Variations in the Earth's gravity field can be expressed as both a perturbing acceleration $\mathbf{f}$ or potential R. Accounting for only oblateness, the potential and acceleration are given by [98]:

$$R_{J_2} = \frac{J_2 \mu R_E^2}{2r^3}\left(1 - 3\sin^2 i \sin^2(v+\omega)\right) \tag{5.34}$$

$$\mathbf{f}_{J_2} = -\nabla R_{J_2} \tag{5.35}$$

To facilitate comparison with literature, the following constants were assumed [87]: $\mu = 398\,601\,\mathrm{km}^3\,\mathrm{s}^{-2}$, $R_E = 6371.22\,\mathrm{km}$, and $J_2 = 1.082\,65 \times 10^{-3}$.

DRAG ACCELERATION

Due to the presence of an atmosphere the satellite will experience drag, dissipating the satellite's orbital energy. A simple tabulated exponential density model, based on USSA-1976 and CIRA1972, is assumed [106]. A spherical Earth is assumed and the co-rotation neglected. The drag acceleration is:

$$\mathbf{f}_{drag} = \frac{1}{2}\rho \mathbf{v}^\intercal \mathbf{v} \frac{SC_D}{m} \tag{5.36}$$

where the constants $C_D = 2.2$ and $S/m = 0.01\,\mathrm{m}^2\,\mathrm{kg}^{-1}$ are assumed [95].

5.4.4. TEST PROBLEMS

The analysis is executed for several test problems. Table 5.2 gives an overview. By default Problem 1 is used for Cases A to D, for Case E all three problems are analysed. The initial positions are given in Table 5.3.

Table 5.2: Overview of the orbits of the different test problems.

#	a [km]	e [–]	i [°]	T [d]	Revs [–]	Note
1	136 000	0.95	30.0	100	17.43	"Example 2" [87]
2	6777	0.0012	51.4	2	31.12	ISS [2]
3	29 600	0.0005	55.2	20	34.57	GSAT0101 [3]

Problem 1 was originally introduced as "Example 2" in Ref. [87] and is commonly used throughout literature [88, 93, 95]. Problem 2 is a near-circular low-earth orbit (LEO).

Table 5.3: Initial position and velocity of different test problems.

#	x_0 [km]	y_0 [km]	z_0 [km]	v_{x_0} [km s^{-1}]	v_{y_0} [km s^{-1}]	v_{z_0} [km s^{-1}]
1	0	−5888.9727	3400	10.691 338	0	0
2	−276.511	4783.577	4790.565	6.899 16	2.172 63	−2.554 63
3	−6836.512	2513.848	−28 685.790	−0.990 54	−3.533 21	−0.071 89

The orbit of the ISS (orbit 925) is used as a reference. Of course, for the propagation in LEO a more accurate atmospheric model is necessary. Nonetheless, the exponential model that was selected will show the effect of a dissipative force. Moreover the gravity model including only J_2 is not considered very accurate for this type of orbit. Finally, Problem 3 uses the orbit of the first Galileo satellite (GSAT0101) as a reference. The TLE at epoch 15 051.142 84 834 (February 20, 2015) is used for the initial conditions. As the satellite is in MEO, it will not experience the effects of the atmosphere or oblateness as much as a LEO satellite. Nonetheless, both the drag and J_2 perturbations are modelled.

5.4.5. INTEGRATORS

Except for unperturbed motion, the EOMs need to be integrated numerically. The choice of integrator also has a large influence on the accuracy and efficiency. Distinctly different types of integrators are analysed to assess their performance. These include a single-step (DOPRI), multi-step (Adams-Bashforth-Adams-Moulton or ABAM), and Taylor-Series integrators (TSI).

For each integrator, only the absolute and relative tolerances are changed to obtain different data points of the accuracy versus the number of function evaluations. The tolerances in each case are set equal for each parameter, such that $\epsilon_{abs_i} = \epsilon_{rel_i} = \epsilon \forall i$.

DORMAND-PRINCE 5(4)

DOPRI is a member of the Runge-Kutta (RK) family and convenient for adaptive step-size. RK techniques approximate a Taylor-series extrapolation of a function by evaluating the first derivative at different points within the interval and do not rely on previous solutions. Unfortunately, the truncation error is not available as part of the solution and requires the evaluation of another RK method of one order less or higher [107]. DOPRI5(4) is a fifth-order integration method, where the fourth-order is used for error control. The method is implemented in Matlab as ode45, and is used as is.

ADAMS-BASHFORTH-ADAMS-MOULTON

Multi-step methods take advantage of the history of previously evaluated steps. In case of predictor schemes the new step is predicted using only the history available. A corrector uses the derivative at this new point to further improve the solution. ABAM, uses the AB predictor and AM corrector. The difference between the predicted and corrected values offers a measure of the error at each step. Only two derivatives are evaluated for each step, independent of the order. However, these methods are more complex to program and require special starting methods [108]. The integrator is implemented in

Matlab as ode113, with adaptive order and step size based on the theory presented in Ref.[109].

TAYLOR SERIES INTEGRATION

TSI uses higher-order derivatives to expand the solution around the known point. In theory, a solution can be represented by an infinite series. In practice, the series is truncated after a desirable order K. TSI is very efficient as large steps can be made. However, it is difficult to implement. Automatic derivation up to any order is achieved by rewriting the EOMs using recursion formulas. To derive the recursion formulas, additional state variables need to be introduced. Due to this overhead, TSI is only more efficient when a problem can be solved many times [110]. Complications arise from models that are discrete/discontinuous (e.g., look-up tables). Most models can only be made piecewise continuous. The derivatives are therefore only valid within a certain region, limiting the maximum step size to its boundary. The value of the independent parameter at the boundaries need to be found using a root-finding algorithm. Interpolation of models can either be done once (for simple models) or on a need basis. Derivatives of numerical (black-box) models can be obtained through finite differencing. In Ref. [111] a practical introduction of the subject is presented.

The order K and step size h need to be controlled to keep the truncation error in bounds, while maximising computational efficiency. An estimate of the truncation error is generally obtained from the higher-order terms. The following step-size controller, which computes the Lagrange remainder using the last two terms, is used [112]:

$$\begin{aligned} h_0 &= \left(\min_{\forall i} \left\{ \frac{\epsilon_i}{|(x_i)_{K-1}|} \right\} \right)^{\frac{1}{K-1}} \\ h_1 &= \exp\left[\frac{1}{K-1} \ln\left(\min_{\forall i} \left\{ \frac{\epsilon_i}{|(x_i)_{K-1}| + K|(x_i)_K| h_1} \right\} \right) \right] \end{aligned} \tag{5.37}$$

The estimate for the step size can be iterated further (by obtaining h_2 by substituting $h_0 = h_1$ etc.), but only the first iteration is applied. The order is assumed to be fixed throughout the integration and is optimised for each tolerance.

SIMPLIFICATIONS OF THE ATMOSPHERIC MODELLING

To simplify integrating with TSI, the following atmospheric model is assumed (for Case D only): $\rho = \exp(-0.003\,731\,343\,283\,582\,1 h - 29.702\,507\,460\,603\,904\,1)$, giving a good fit for $h \geq 800\,\text{km}$. The EOMs for the gravity with oblateness (J_2) are taken from Ref. [112], with

the following additionally derived equations and recurrence relations:

$$f_4 = \mathbf{v}^\mathsf{T}\mathbf{v} \qquad (f_4)_k = \sum_{j=0}^{k} (\mathbf{v})_k^\mathsf{T} (\mathbf{v})_{k-j} \tag{5.38}$$

$$v = \sqrt{f_4} \qquad (v)_k = \frac{1}{(f_4)_0} \sum_{j=1}^{k} \left(\frac{3j}{2k} - 1 \right) (f_4)_j (v)_{k-j} \tag{5.39}$$

$$\rho = a\exp(-br) \qquad (\rho)_k = a(-b)^k \sum_{j=1}^{k} \frac{j(r)_j (\rho)_{k-j}}{k} \tag{5.40}$$

$$f_5 = v\rho \qquad (f_5)_k = \sum_{j=0}^{k} (v)_j (\rho)_{k-j} \tag{5.41}$$

$$\mathbf{f} = -\frac{1}{2} f_5 \mathbf{v} \frac{SC_D}{m} \qquad (\mathbf{f})_k = \frac{1}{2} \frac{SC_D}{m} \sum_{j=0}^{k} (f_5)_j (\mathbf{v})_{k-j} \tag{5.42}$$

where f_4 and f_5 represent some auxiliary introduced variables and

$$a = \exp(bR_E - 29.702\,507\,460\,603\,904\,1)$$
$$b = 0.003\,731\,343\,283\,582\,1$$

5.5. RESULTS AND DISCUSSION

Each of the cases is analysed and their results are presented and discussed.

5.5.1. CASE A: TIME-STATE OPTIONS

The linear and constant time elements have been presented. The numerical properties of the three options have been extensively studied in Ref.[96]. In general, it is found that the time elements outperform the physical time on all test problems. As expected, for circular orbits with only J_2, all three options perform roughly equal. Similarly, they converge with higher number of function evaluations. For these two cases the physical time can be considered, as the equations are much simpler.

The time elements were found to be most accurate (up to 3-6 orders in magnitude) for low number of function evaluations, where the accuracy of the time t is dominating the integration. The evolution of all three options over two full orbits on Problem 1 are shown in Figure 5.3. As can be seen from the plot the physical (non-dimensional) time exhibits a sigmoid-type curve for every revolution. For this specific problem, this behaviour is driven by variations in the radius r. However, looking at Eqs. (5.3) and (5.4), a similar trend occurs for variations of the orbital energy. As time is a strictly increasing function, it is by definition hard to approximate with a polynomial and therefore difficult to integrate. Only when the orbit is circular (and mainly conservatively perturbed) or the integration steps become small, a good fit can be obtained.

5.5.2. CASE B: FIXED-TIME PROPAGATION

Three solutions for propagating to a fixed time have been proposed. Figure 5.4 shows the error made in approximating final time (solid lines) and in position (dashed lines) as

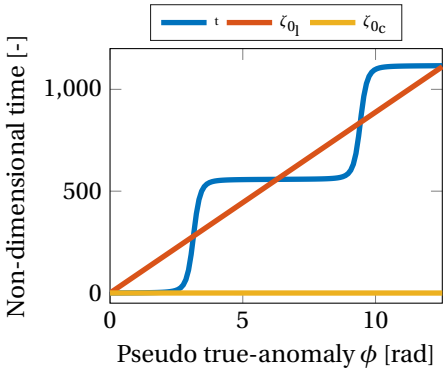

Figure 5.3: Evolution of different time elements (Case A) for two revolutions on problem 1.

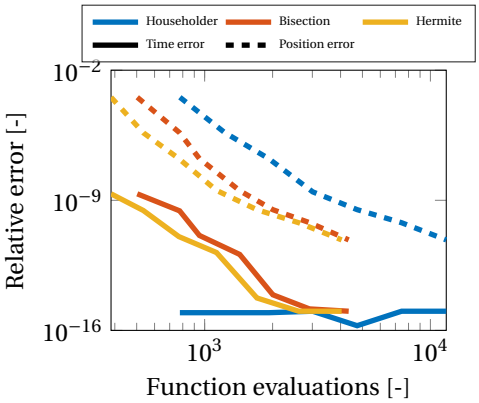

Figure 5.4: Error in final time as a function of the derivative evalutions for different approximation methods (Case B).

5

a function of the number of function evaluations.

The ability of the householder method to estimate time correctly is constant, regardless of the number of function evaluations. This is to be expected considering the earlier discussion about how the iterative scheme decouples the error of estimation from the solution. The bisection and Hermite interpolating methods show only a small difference. Both approach the accuracy of the householder method as the number of function evaluations increases. As the step size goes down with increasingly stringent tolerances, the integration steps get smaller and thus closer to the value of t_f that is to be estimated, therefore reducing the impact of estimation.

Looking at the position error (dashed lines), the householder method actually performs worst, due to its inefficiency. The difference between the other two methods is again relatively small. However in terms of function evaluations the Hermite interpolation method is between 7 (for high accuracy) to 24 % (for low accuracy) more efficient than bisection.

5.5.3. CASE C: FORCE MODELLING

Next, the effects of different perturbations are investigated. First, the unperturbed motion is analysed, followed by perturbed motion due to the Earth's oblateness (J_2), and finally the atmospheric drag is added. The results are shown in Figure 5.5.

For the unperturbed case (solid line), Dromo clearly performs best and the function evaluations and precision are hardly impacted by the tolerances settings. Ideally the precision would be perfect, as the elements are not impacted by the integration as their derivatives are zero and thus remain constant. The small error that is present and the associated number of function evaluations stem from the approximation of ϕ_f and any numerical errors during conversion from and to Cartesian coordinates.

It can further be seen that MEE is about an order more accurate compared to Cowell, for a given number of function evaluations. The errors originate from the integration of the true longitude alone (as the other five are constant).

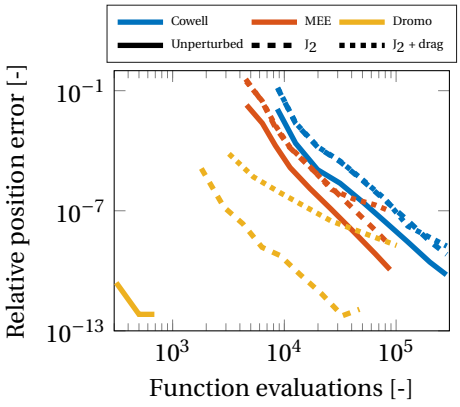

Figure 5.5: Comparison of different force models (Case C) on test problem 1.

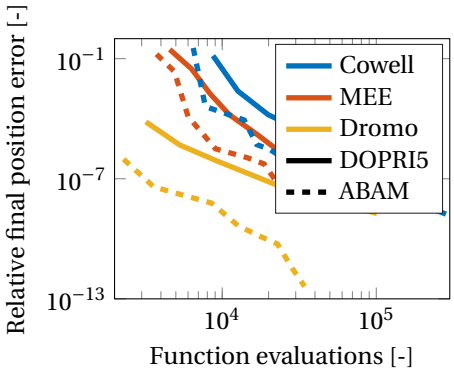

Figure 5.6: Comparison of different integration methods (Case D) on test problem 1.

For the second case (J_2, dashed line), again Dromo performs best. Compared to MEEs, Dromo has a better accuracy and is more efficient. It is remarkable that for a low number of function evaluations the other methods do not even offer a useful solution, Moreover, for Dromo the minimum error remains unaffected, though the number of function evaluations has increased. This shows the benefit of Dromo's approach to treating the perturbation as a conservative potential, in which the total energy does not change. The other two methods show a shift upwards, signifying a reduction in accuracy for a given number of function evaluations.

Lastly, for the case with both a conservative and a non-conservative perturbation (J_2 + drag, dotted line), all methods show a reduction in accuracy. Especially Dromo shows a significantly reduced accuracy. Nonetheless, the method still performs best, especially with a low number of function evaluations, where it is over two orders more accurate than MEE.

5.5.4. CASE D: NUMERICAL INTEGRATORS

The fully-perturbed problem is analysed for three different variable step-size integrators: DOPRI5(4), ABAM, and TSI. Figure 5.6 shows the results. The differences among the integrators are most profound for the more stringent tolerance settings (higher evaluations). ABAM is found to be more efficient than DOPRI5(4) (or any other RK-family integrator) on this problem, especially for high-accuracy applications. For Dromo and MEE there is only an improvement in function evaluations. ABAM for Cowell's method shows better performance at a reduction in accuracy. This is likely due to the large variation of the states for this method, as ABAM relies on previous states.

Only results for TSI of Cowell's method were obtained. It can be seen that TSI performs significantly better than DOPRI and approaches ABAM for the lower number of function evaluations. Increasing the tolerance above 10^{-13} yields no additional benefits in terms of accuracy at the expense of evaluations. Three factors however have to be taken into account when viewing these results. First, the atmospheric model was further

simplified for the comparison. If more advanced models are used, the step size has to be limited further. Secondly, the dimension of the Cartesian TSI state is 22 as opposed to 6 for the regular implementation, which has not been taken into account in the number of function evaluations. Lastly, finding the optimal order for TSI was found to be non-trivial. No order controller gave consistent results on this problem and was thus optimised for each run and shown in Table 5.4.

Table 5.4: Optimal Taylor-series integration order for a given tolerance, determined throught trial-and-error.

Tolerance	10^{-7}	10^{-8}	10^{-9}	10^{-10}	10^{-11}	10^{-12}	10^{-13}	10^{-14}	10^{-15}
Order	14	16	16	16	18	20	18	18	19

5.5.5. CASE E: DIFFERENT ORBITS

The fully perturbed case of Problem 1, given by Figure 5.5, was already analysed. Problems 2 and 3 are also analysed. Their results are shown in Figures 5.7 and 5.8, respectively. Comparing Problem 2 to Problem 1, Dromo and MEE are much closer to each other. For the lower number of function evaluations, Dromo is about 1-2 orders more accurate than MEE, compared to 2-4 orders for the fully perturbed case of Problem 1. For a higher number of function evaluations two methods even converge and reach the same minimum error.

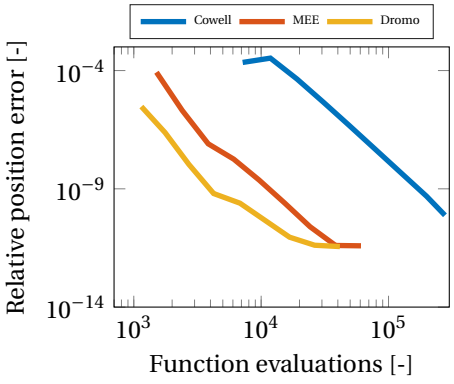

Figure 5.7: Comparison of methods on circular LEO (Case E, Problem 2).

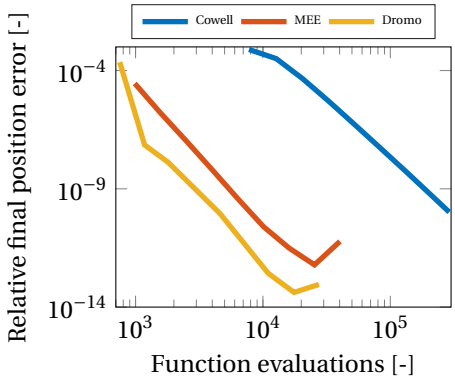

Figure 5.8: Comparison of methods on circular MEO (Case E, Problem 3).

As can be seen from the figures, Dromo also performs best for these problems. Both Dromo and MEE achieve a maximum accuracy, after which higher tolerances do not result in increased accuracy. This is caused by the total round-off error becoming dominant over the decrease in the total truncation error. Dromo compares favourably in this respect against MEE, by achieving a lower minimum error of around one order less.

Both Problems 2 and 3, compared to 1, show Dromo and MEE closer to each other. From this it can be concluded that MEE performs relatively worse on highly elliptic orbits. The convergence of Dromo to MEE, which is present in Problem 2, but not in 3

indicates that this should be attributed to atmospheric drag.

5.6. CONCLUSIONS

The time elements have very interesting properties and prove a useful addition to the Dromo formulation, especially for low-accuracy computations on problems where the orbital radius and/or energy vary.

Two methods for propagating to a fixed epoch have been proposed, namely bisection and Hermite interpolation. Both methods work very well. In terms of accuracy they approach the classical Householder method for stringent tolerance settings. Although their absolute accuracy lacks behind the iterative scheme, overall their performance in terms of positional accuracy over function evaluations is better in all cases. The differences between bisection and Hermite interpolation are largest in the low-accuracy region, where Hermite interpolation is up to 25 % more efficient in terms of function evaluations.

Dromo dominates the other methods for all cases and problems, especially in terms of computational effeciency. Cowell's method performed worst on all problems. Dromo and MEE performed roughly equal for a small portion of the regime with high accuracy and number of function evalutions on Problem 2 (LEO with drag). Dromo is found to be very efficient, finding relatively accurate solutions for a limited number of evaluations. Similarly, Dromo is able to propagate more accurately than other methods, demonstrating a higher maximum accuracy, at a fraction of the computational cost of the other methods.

The choice of numerical integrators has an effect on performance. ABAM works very well with VOP formulations. TSI outperforms ABAM and DOPRI5(4) for Cowell's method. However, a number of practical issues have been presented that have to be addressed, especially expansion for discontinuous models and order control. TSI for Dromo should provide an additional gain in performance; it remains to be seen how much additional overhead is introduced. The number of additional state variables that needs to be introduced is large, due to Dromo's more complex ODEs.

In conclusion, it is demonstrated that Dromo, through the proposed adaptations, can be successfully applied to real orbit problems, providing significant benefits in both accuracy and number of functions evaluations. These findings should hold true for regularised propagation methods in general. The advantage in terms of computational efficiency is most significant for low- to medium-accuracy applications. For the propagation of LEO satellites, Dromo offers an improvement in accuracy (for a given number of function evaluations) of up to seven orders in magnitude, compared to the standard Cowell's method using Cartesian coordinates. The proposed method is recommended for all orbit problems that have been analysed. Especially great potential is foreseen for highly demanding applications, such as the propagation of a large catalog of objects, where currently (semi-)analytic techniques are employed.

6

VERIFIED REGULARISED INTERVAL ORBIT PROPAGATION

Geul, J., Mooij, E. and Noomen, R.

Published [1] in Journal of Guidance, Control, and Dynamics, Vol. 44, No. 4, pp. 719–731, 2021

Verified interval orbit propagation provides mathematically guaranteed solutions of satellite position and velocity over time. These verified solutions are useful for conjunction analysis and other space-situational-awareness activities. Unfortunately, verified methods suffer from overestimation and explosive interval growth, limiting the possible propagation time and thus their applicability. Different orbital-element state models have been shown to increase the maximum propagation time to a degree, but at the expense of significant overestimation introduced by the state transformations. This thesis proposes the Dromo state model for verified integration. Dromo is a regularized variation-of-parameter formulation of the perturbed two-body equations of motion. Taylor models are implemented for both integration and transformation. Moreover, a technique is developed for dealing with time uncertainty resulting from verified regularized propagation. Dromo significantly prolongs the maximum forecasting window, producing verified trajectories of days up to weeks in duration for the low-Earth orbit regime. A sensitivity analysis of the integrator settings identifies combinations that produce stable and computationally efficient solutions. A sensitivity study of the orbital parameters shows that the method is applicable to a large orbital regime, especially for low-Earth orbit regions that contain high densities of space debris.

6.1. INTRODUCTION

Space debris composes the largest group of observable objects in Earth orbit, and presents a major threat to operational spaceflight [113]. Collision prediction methods gen-

[1] Minor modifications have been made for this thesis.

erally compute potential collisions, by propagating initial states and state errors as probability density functions to an estimated time of closest approach [114–117]. Verified interval orbit propagation (VIOP) presents a different approach to conjunction analysis [118]. VIOP generates bounds on the state that are guaranteed to encompass the exact solution at any given time. The non-intersection of VIOP solutions mathematically rules out possible collisions, whereas an intersection implies the possibility of a collision, however, with an unknown likelihood. This unique mathematical property makes VIOP interesting for many space-situational-awareness (SSA) activities, potentially in combination with statistical methods. Verified integration has previously been applied to computing Solar-System dynamics [119], intersections between near-Earth objects and Earth [120, 121], and satellite conjunctions [118, 122]. Verified predictions of the Iridium-Cosmos collision were studied in Ref. [118]. The error build-up of regularized formulations was analysed using interval arithmetic in Ref. [123].

Verified methods are known to suffer from overestimation, which results in rapid growth and explosion of the verified solutions after short periods of integration. Different state models are shown to improve the forecasting window up to four to ten times [118]. A differential algebra formulation of the simplified general perturbation (SGP4) model was used for uncertainty propagation in Ref. [124]. Due to the interval transformations from Cartesian coordinates to the propagation state model and back, a large amount of additional overestimation is introduced. Especially, the overestimation resulting from the transformation of the initial uncertainty is included in the propagation, reducing the overall effectiveness. Regularized methods for verified propagation have recently been suggested as a state model [123]. However, the time transformation in regularization brings forth additional practical challenges, as described in Chapter 5 [125].

This thesis aims to increase the time until solution explosion by proposing the regularized Dromo formulation as the state model [95]. Moreover, the research aims to reduce the overestimation in the interval state transformations. Also, the thesis proposes a new technique for converting time uncertainty into additional post-propagation uncertainty in position and velocity. The study primarily focusses on low-Earth orbit (LEO) satellites. LEO presents a demanding environment and is very relevant for collision prediction and avoidance.

The chapter is structured as follows. First, a background of interval analysis and verified orbit propagation is provided in Sec. 6.2. Regularized propagation and the proposed Dromo state model are given in Sec. 6.3. The interval state transformations and the developed time uncertainty transformation technique are presented in Sec. 6.4. In Sec. 6.5, the models and set-up of the study are explained. Section 6.6 shows the results of the transformation techniques, a comparison of Dromo with other state models, and a sensitivity analysis into the integrator settings and orbital parameters. Lastly, the conclusions are given in Sec. 6.7.

6.2. VERIFIED PROPAGATION

VIOP is an uncertainty analysis method that applies initial-value-problem (IVP) interval methods to the satellite equations of motion (EOMs). In this, the initial uncertainty, model uncertainty, and numerical truncation and rounding errors are modeled and bound by intervals. VIOP provides a verified interval solution of the position and velo-

city of a satellite trajectory over time, which is mathematically guaranteed to contain all possible trajectories. This characteristic makes verified integration interesting for many different applications.

A classical application of VIOP in celestial mechanics is the propagation of asteroid state vectors [119, 126]. If the interval solution, which encloses all possible trajectories, fails to intersect the Earth, an impact can be mathematically ruled out. This is opposed to statistical methods, which only ascribe probabilities to certain events, and are not able to rule any out.

It is realistic to consider that for physical applications, the mathematical proof holds for the model (i.e., the ordinary differential equations (ODEs) and its parameters) and the given initial conditions. Inherently, the mathematical model has a limited fidelity and the initial conditions are often not known perfectly (e.g., derived from observations). So the mathematically guaranteed solution does not necessarily translate to the physical world. To account for this, the modeling and initial condition errors have to be conservatively estimated and included in the uncertainty of the system.

Interval analysis (IA) in general and Taylor Models (TM) specifically are presented in Sec. 6.2.1. IA suffers from overestimation, which is the inclusion of trajectories that should not be contained within the interval. Several sources of overestimation are discussed in detail in Sec. 6.2.2. Finally, Sec. 6.2.3 discusses the verified solution of initial value problems.

6.2.1. INTERVAL ANALYSIS AND TAYLOR MODELS

IA is an extension of real-number arithmetic to intervals and was developed by Moore in the early 1960s [127]. A real interval X is defined as the set of real numbers lying within (and including) a given lower and upper bound:

$$X = [\underline{X}, \overline{X}] = \{x \in \mathbb{R} \mid \underline{X} \leq x \leq \overline{X}\} \tag{6.1}$$

where the under- and overline indicate the lower and upper bound, respectively. The width of the interval is calculated as $w(X) = \overline{X} - \underline{X}$, and the midpoint as $m(X) = (\underline{X} + \overline{X})/2$. IA describes rules for the basic arithmetic operations, such as addition, multiplication, and inversion [128]:

$$X + Y = [\underline{X} + \underline{Y}, \overline{X} + \overline{Y}] \tag{6.2}$$

$$XY = [\min(\underline{X}\underline{Y}, \underline{X}\overline{Y}, \overline{X}\underline{Y}, \overline{X}\overline{Y}), \max(\underline{X}\underline{Y}, \underline{X}\overline{Y}, \overline{X}\underline{Y}, \overline{X}\overline{Y})] \tag{6.3}$$

$$X^{-1} = [\overline{X}^{-1}, \underline{X}^{-1}] \tag{6.4}$$

where a special formulation of the inversion is used when $0 \in X$.

Most mathematical operations and functions have been defined for IA, as well as expansion to interval vectors and matrices. An example of an interval calculation is presented in Sec. 6.2.2. When interval calculations are performed numerically, special rounding techniques ensure that the interval bounds are always rounded outward to the next machine- representable number. This ensures that rounding errors are absorbed within the intervals during all computations.

TM recursively computes high-order multivariate polynomial function approximations of IA to reduce overestimation due to the dependency problem. With TM possible cancellation of sub-parts of the function can be detected [129]. The dependency problem is discussed in Section 6.2.2. TMs have been developed by Berz and Makino, and Hoefkens since 1996 [126, 129, 130]. A separate remainder term rigorously bounds the approximation error due to truncation, to control the dependency problem of IA [130].

The TM T_f of a function f of up to order k is written as:

$$f(x) \in T_f(x) = p_f(x) + R_f(x) \qquad \text{for } x \in [\underline{X}, \overline{X}] \tag{6.5}$$

$$p_f(x) = \sum_{n=0}^{k} \frac{f^{(n)}(a)}{n!}(x-a)^n \tag{6.6}$$

where $p_f(x)$ is the expansion of $f(x)$ around a up to order k. The interval remainder is R_f. To obtain the interval remainder bound, the remainder, i.e., the $(k+1)$th term, of the series expansion can be quantitatively bounded using different interval methods. The choice of method has a significant impact on the performance of TMs and many bounding schemes have been proposed [131, 132].

6.2.2. OVERESTIMATION

Overestimation is the inclusion of non-solutions within the interval. Three sources for overestimation can be distinguished: wrapping, cancellation, and dependency. Wrapping and dependency are discussed in more detail below. Cancellation occurs when the regular floating-point result of an operation has a small magnitude compared to the individual numbers, for instance, when subtracting two large and nearly equal numbers. The floating-point result is a number of relatively small magnitude, while in IA the widths of the interval are always additive and thus result in a large interval with large overestimation [131].

In recurrent computations, overestimation leads to the inclusion of non-solutions in subsequent analyses, giving rise to even more overestimation. This leads to a phenomenon known as interval explosion: an exponential growth of the interval solution. When interval explosion occurs, further computation becomes physically nonsensical. Interval explosion can also occur for stable dynamical systems.

WRAPPING

Wrapping occurs when the true shape of the uncertainty cannot be sufficiently represented by an interval. Consider an initial uncertainty that is described by a circle. The representation of this uncertainty in Cartesian coordinates results in a square interval. Therefore, the interval contains many non-solutions outside the original circle. In VIOP, the wrapping effect occurs not only when enclosing the initial uncertainty in interval form, but also at every step of the integration, as the continuous dynamical system is numerically discretized [131]. The recurrent wrapping at each time step might only produce a small amount of overestimation, but cumulatively it can lead to interval explosion.

The wrapping effect can be reduced by choosing a different coordinate system. In the example of the 2D circular uncertainty, polar coordinates can be used to perfectly

describe the uncertainty without any overestimation at all. Likewise, for orbit propagation, different state models can be used to better describe the uncertainty and thus limit wrapping overestimation at each step. Furthermore, state models with slow-varying elements can reduce the number of integration steps necessary and thus the number of times wrapping occurs. The downside of a different state model is that the initial uncertainty and final solution after propagation often need to be transformed, which itself introduces overestimation.

The unified state model (USM) and modified equinoctial elements (MEE) are investigated in Ref. [118], and outperform the classic Cartesian state model significantly in propagation time to solution explosion. The hybrid-interval trajectory is a novel technique proposed in Ref. [118], and propagates multiple state models concurrently. In this approach, only the intersection of the interval solutions (in Cartesian coordinates) becomes the true verified solution. Solutions outside the intersection of the intervals produce overestimation, as verified methods demand that all solutions are enclosed. The technique is effective in reducing the overestimation of the instantaneous verified solution. However, the intersection of the intervals must be computed in a common coordinate system, which introduces overestimation in the transformation. Therefore, hybrid intervals do not improve the propagation time until solution explosion.

DEPENDENCY PROBLEM

Dependency results from multiple occurrences of one or several variables in a system of equations. While a variable may take on any value within its interval, it must take on the same value in each occurrence. However, this dependency is not taken into account in interval arithmetic [133, 134]. To illustrate the dependency problem, the interval solutions G and H of equivalent functions $g(x)$ and $h(x)$ are computed for $X = [2, 3]$ [134]:

$$
\begin{aligned}
g(x) &= \frac{x}{x-1} \\
G([2,3]) &= \frac{[2,3]}{[2,3]-1} = \frac{[2,3]}{[1,2]} = [1,3] \\
h(x) &= 1 + \frac{1}{x-1} \\
H([2,3]) &= 1 + \frac{1}{[2,3]-1} = 1 + \frac{1}{[1,2]} = 1 + [0.5,1] = [1.5,2]
\end{aligned}
$$

where $w(G) = 2$ and $w(H) = 0.5$. G overestimates the true width by a factor four. The dependency problem increases with the complexity of the equations and the number of occurrences. Often, it is not possible to rewrite the equations to reduce dependency.

6.2.3. VERIFIED INITIAL VALUE PROBLEM SOLVERS

In traditional IA the solution at each integration step is computed in two stages [135]. In the first stage, the existence and uniqueness of a solution are proven by computing a rough enclosure of the solution, referred to as the *a-priori* solution, which is valid over the integration step, from t_1 to $t_1 + \Delta t$. The rough enclosure can potentially significantly overestimate the solution. A smaller (or tighter) solution is desired. In the second stage,

a tighter solution is computed, which provides the instantaneous verified solution at time t_1. The exact details of each step depend on the specific solver that is used and are not important for the application. The a-priori solutions are used when a continuous solution is desired, while the tight solutions are the starting point for each integration step.

Many software packages exist that use TM for verified integration, including COSY [129], VNODE-LP [133], VSPODE [134], and RiOT [136]. These packages differ in how range bounding is implemented and what techniques are used for computing the tighter enclosure in the second stage. The packages further differ in their availability [137]. A survey of available packages on the basis of propagation time until solution explosion shows that VSPODE (Validating Solver for Parametric ODEs) is very promising [118].

VSPODE uses a unique algorithm for computing tighter enclosures, which addresses the wrapping effect by propagating the intermediate results using TMs as a function of the model parameters and initial values [134]. This means that intervals of both initial state and model parameters are parametrically expressed in the solution and evaluated in the last step. VSPODE solves parametric autonomous IVPs. For non-autonomous systems, the EOMs need to be adapted to an autonomous form by introducing an additional pseudo-state variable.

The VSPODE solver is controlled by three tuning parameters: k, q, and ϵ, where k is the order of the interval Taylor series (ITS) with respect to time, q is the order of the TM as a function of the initial intervals and uncertain parameters, and ϵ the numerical tolerance controlling the step-size. The order q determines how well the intervals are described as a function of the initial intervals and uncertain parameters, and thus the effectivenes in reducing overestimation when computing tighter enclosures. The sensitivity of the verified solution to the tuning parameters is investigated in Sec. 6.6.6. Another important parameter of VSPODE is the number of uncertain quantities N_u, which is the sum of uncertain state variables and system parameters. The computational cost of VSPODE is proportional to a power $N_u q$ [134]. Therefore, it is important to minimize N_u, which will be discussed in Secs. 6.5 and 6.6.6.

6.3. REGULARIZED PROPAGATION

Regularization aims to remove singularities and dynamical instability from the EOMs, leading to less integration errors and more efficient integration. This is achieved by a transformation of the independent variable (in orbital mechanics a Sundman transformation is commonly used for this) and the introduction of a new set of variables instead of position and velocity to represent the motion [138]. Sometimes, these new variables are integrals of the two-body problem, and their variations when the motion is perturbed can be obtained by the variation-of-parameters (VOP) technique, starting from the unperturbed solution of the equations of motion.

6.3.1. DROMO AND COMPARISON OF REGULARIZED METHODS

Two popular methods are Kustaanheimo-Stiefel (KS) [99] and Sperling-Burdet (SB) [100] regularizations. Since 2000, new special perturbation methods that take advantage of quaternions have been developed [89–96].

Dromo is a modern VOP method derived from the Burdet-Ferrándiz regularization [93, 101]. It has been applied to the propagation of asteroid orbits for computing planetary close encounters, and for the lifetime analysis of space debris [139]. Dromo is also used for covariance propagation of asteroids [140]. Dromo employs only eight EOMs, which is close to non-regularized methods (often six) and less than other regularized methods: KS and SB feature 10 and 12 differential equations, respectively [102]. In Ref. [95] a new version of Dromo is presented, which allows a separate treatment of perturbing forces that are derivable from a potential and those that are not. The behavior of the EOMs can be further improved through the use of time elements [96].

Dromo is compared against a number of classical and modern methods in Table 6.1. This table is a reproduction of Table 5.1. Stiefel-Scheifele (SS) [141] represents the benchmark for this problem. The table gives the final state of a satellite in a highly eccentric ($e = 0.95$ and $r_p = 6800$ km) orbit about the Earth. The motion is perturbed by the Earth's oblateness (J_2) and third-body gravitational attraction of the Moon. The orbit is integrated for 288.127 689 41 mean solar days (roughly 50 revolutions). The final position (R_x, R_y, R_z), number of steps per revolution (steps/rev), and the absolute error with respect to the benchmark are reported. Additional results for Cowell, Dromo, and MEE, and USM [103] are added to the original comparison table reported in [142].

Table 6.1: Comparison of results from literature of several methods for the oblate Earth plus Moon after 288.12768941 days [103, 142].

	SS [142]	SB [142]	KS [142]	Cowell-E[a] [142]
R_x [km]	−24 219.050	−24 218.818	−24 219.002	−24 182.152
R_y [km]	227 962.106	227 961.915	227 962.429	227 943.989
R_z [km]	129 753.442	129 753.343	129 753.822	129 744.270
Steps/rev	500	62	62	240
Error [km]	*baseline*	0.318	0.501	42.5

	Dromo [125]	Cowell[a] [125]	MEE	USM [103]
R_x [km]	−24 218.829	−24 256.391	−24 256.980	−24 219.049
R_y [km]	227 961.980	227 980.068	227 979.117	227 962.106
R_z [km]	129 753.414	129 762.509	129 761.798	129 753.442
Steps/rev	113	453	188	372
Error [km]	0.256	42.4	42.4	42.1

[a] "Cowell-E" indicates the formulation in Ref. [105], which uses the total energy as an independent parameter, while "Cowell" indicates the classic Cartesian formulation.

On the test problem, all regularized methods (SB, KS and Dromo) perform much better in terms of accuracy than the others. This is not at all surprising as the orbit is highly eccentric. Cowell, MEE and USM are integrated using Runge-Kutta Dormand-Prince 5(4) variable step-size integrator. The final errors of these three methods were matched

to the Cowell-E final error by changing the numerical tolerances, to provide a direct comparison of the number of integration steps per revolution. The cost and error of Dromo are comparable to other regularized methods. On problems with lower eccentricities ($e = 0, 0.3, 0.7$) it performs much better than the other methods, as shown in Chapter 5 and Ref. [96]. The Dromo transformation equations to Cartesian coordinates are more accurate than KS [123]. MEE and USM have much better performance (approaching the performance of Dromo) for less eccentric orbits ($e < 0.3$) [103, 125]. The lean formulation, regularized properties, and good performance on a wide range of problems, make Dromo interesting for verified propagation.

6.3.2. DROMO FORMULATION

In Dromo, the motion is represented by the non-dimensional physical time (ζ_0) and seven parameters, which are first integrals of the two-body problem. Three of the parameters (ζ_{1-3}) fix the shape of the osculating conic and the remaining four are the components of a unit quaternion (ζ_{4-7}), which describes the orientation of the orbital plane and of a reference direction on it. All quantities in Dromo are made non-dimensional by introducing units for time and length as n_0^{-1} and R_0, respectively. These quantities are defined when the Dromo state is first computed. Here, R_0 is the initial radius and n_0 the initial circular mean motion (i.e., $n_0 = n(a{=}R_0) = \sqrt{\mu/R_0^3}$) [95]. For intervals, R_0 is defined as $R_0 = \sqrt{m(X_0)^2 + m(Y_0)^2 + m(Z_0)^2}$. Here $m(X_0)$ is the midpoint of initial interval X_0 in x-direction, as discussed in Section 6.2.1.

The perturbations are expressed in the orbital reference frame (i.e., consisting of the radial, transverse, and normal components [143]) and separated into those derivable and non-derivable from a potential. The separation allows for conservation of energy, when only conservative forces are applied. The total perturbing acceleration $\mathbf{f}$ is given by:

$$\mathbf{f} = \mathbf{P} + \nabla\mathscr{U} \tag{6.7}$$

where $\mathbf{P}$ is the sum of all perturbations that are non-derivable from a potential and $\nabla\mathscr{U}$ is the gradient of the total perturbing potential.

EQUATIONS OF MOTION

The physical time t is non-dimensionalized as $\zeta_0 = tn_0$, and is a function of the fictitious time ϕ through Eq. (6.8). Along Keplerian motion ϕ behaves like the true anomaly. The entire derivation of the elements is presented in Ref. [95], and only the ODEs and relevant transformation equations are presented here. The ODEs of the elements with respect to the independent parameter are [95]

$$\frac{\mathrm{d}\zeta_0}{\mathrm{d}\phi} = \frac{1}{\zeta_3 V_s^2} \tag{6.8}$$

$$\frac{\mathrm{d}\zeta_1}{\mathrm{d}\phi} = \frac{\sin\phi}{V_s}\left(\frac{f_r}{\zeta_3 V_s} - 2\mathscr{U}\right) - \left(\frac{V_s}{\zeta_3} + 1\right)\cos\phi\frac{\mathrm{d}\zeta_3}{\mathrm{d}\phi} \tag{6.9}$$

$$\frac{\mathrm{d}\zeta_2}{\mathrm{d}\phi} = \frac{\cos\phi}{V_s}\left(2\mathscr{U} - \frac{f_r}{\zeta_3 V_s}\right) - \left(\frac{V_s}{\zeta_3} + 1\right)\sin\phi\frac{\mathrm{d}\zeta_3}{\mathrm{d}\phi} \tag{6.10}$$

$$\frac{d\zeta_3}{d\phi} = -\frac{1}{V_s^4}\left[\zeta_3 V_r V_s\left(2\mathscr{U} - \frac{\zeta_3 V_s}{V_s+\zeta_3}\frac{\partial \mathscr{U}}{\partial \zeta_3}\right) + V_t P_t + \frac{\partial \mathscr{U}}{\partial t}\right] \tag{6.11}$$

$$\frac{d\zeta_4}{d\phi} = \frac{1}{2V_s}\left[\frac{f_n}{\zeta_3 V_s V_t}(\zeta_7\cos\Delta\phi - \zeta_6\sin\Delta\phi) + \zeta_5(V_t - V_s)\right] \tag{6.12}$$

$$\frac{d\zeta_5}{d\phi} = \frac{1}{2V_s}\left[\frac{f_n}{\zeta_3 V_s V_t}(\zeta_6\cos\Delta\phi + \zeta_7\sin\Delta\phi) - \zeta_4(V_t - V_s)\right] \tag{6.13}$$

$$\frac{d\zeta_6}{d\phi} = -\frac{1}{2V_s}\left[\frac{f_n}{\zeta_3 V_s V_t}(\zeta_5\cos\Delta\phi - \zeta_4\sin\Delta\phi) - \zeta_7(V_t - V_s)\right] \tag{6.14}$$

$$\frac{d\zeta_7}{d\phi} = -\frac{1}{2V_s}\left[\frac{f_n}{\zeta_3 V_s V_t}(\zeta_4\cos\Delta\phi + \zeta_5\sin\Delta\phi) + \zeta_6(V_t - V_s)\right] \tag{6.15}$$

where f_r and f_n are the radial and normal components of the total perturbing acceleration vector and P_t the transverse component of all perturbing accelerations not derived from a potential. The pseudo-transverse V_s, transverse V_t, and radial velocity V_r are given by

$$V_s = \zeta_3 + \zeta_1\cos\phi + \zeta_2\sin\phi \tag{6.16}$$

$$V_t = \sqrt{V_s^2 - 2\mathscr{U}} \tag{6.17}$$

$$V_r = \zeta_1\sin\phi - \zeta_2\cos\phi \tag{6.18}$$

It is important to note that $\Delta\phi$ in Eqs. (6.12)-(6.15) represents the difference between the current and initial value of the independent variable ($\Delta\phi = \phi - \phi_0$), and not the step size. The initial value of ϕ_0 can be arbitrarily chosen when the initial Dromo state is constructed. A common choice for ϕ_0 is the initial true anomaly $\phi_0 = \nu_0$ or just $\phi_0 = 0$.

Alternatively, when the contribution of the perturbation (**P**) to the total perturbation (**f**) is small, the ODE of the third element ζ_3 can be replaced by that of the total specific energy $\mathscr{E}$:

$$\frac{d\mathscr{E}}{d\phi} = \frac{1}{\zeta_3 V_s^2}\left(V_r P_r + P_t\sqrt{V_s^2 - 2\mathscr{U}} + \frac{\partial \mathscr{U}}{\partial t}\right) \tag{6.19}$$

where ζ_3 can then be obtained through the following equation [95]:

$$\zeta_3 = \sqrt{\zeta_1^2 + \zeta_2^2 - 2\mathscr{E}} \tag{6.20}$$

FROM DROMO TO CARTESIAN COORDINATES

Cartesian coordinates are directly obtained through the transformation matrix $\mathbf{C}_{\mathscr{R}\mathscr{I}}$ of the local-vertical local-horizontal frame $\mathscr{R}$ to the inertial frame $\mathscr{I}$, defined by [95]:

$$\mathbf{C}_{\mathscr{RI}} = \mathbf{C}_0 \mathbf{C}_\phi \tag{6.21}$$

$$\mathbf{C}_0 = \begin{bmatrix} 1-2\zeta_5^2-2\zeta_6^2 & 2\zeta_4\zeta_5-2\zeta_6\zeta_7 & 2\zeta_4\zeta_6+2\zeta_5\zeta_7 \\ 2\zeta_4\zeta_5+2\zeta_6\zeta_7 & 1-2\zeta_4^2-2\zeta_6^2 & 2\zeta_5\zeta_6-2\zeta_4\zeta_7 \\ 2\zeta_4\zeta_6-2\zeta_5\zeta_7 & 2\zeta_5\zeta_6+2\zeta_4\zeta_7 & 1-2\zeta_4^2-2\zeta_5^2 \end{bmatrix} \tag{6.22}$$

$$\mathbf{C}_\phi = \begin{bmatrix} \cos\Delta\phi & -\sin\Delta\phi & 0 \\ \sin\Delta\phi & \cos\Delta\phi & 0 \\ 0 & 0 & 1 \end{bmatrix} \tag{6.23}$$

The non-dimensional Cartesian position and velocity components are obtained as:

$$[R_X, R_Y, R_Z]^\mathsf{T} = \mathbf{C}_{\mathscr{RI}}[r, 0, 0]^\mathsf{T} \tag{6.24}$$

$$[V_X, V_Y, V_Z]^\mathsf{T} = \mathbf{C}_{\mathscr{RI}}[V_r, V_t, 0]^\mathsf{T} \tag{6.25}$$

where the position and velocity can be dimensionalized using the quantities R_0 and n_0, for distance and time, respectively, as defined previously.

FROM CARTESIAN TO DROMO ELEMENTS

Before transformation, the Cartesian coordinates are first non-dimensionalized using the quantities R_0 and n_0, as described in Sec. 6.3.2. The orbital radius r, radial velocity V_r, transverse velocity V_t, and pseudo-transverse velocity V_s are first calculated using [95]:

$$r = \sqrt{R_X^2 + R_Y^2 + R_Z^2} \tag{6.26}$$

$$h = \|\mathbf{h}\| = \|\mathbf{r} \times \mathbf{v}\| \tag{6.27}$$

$$V_r = \frac{\mathbf{r}\cdot\mathbf{v}}{r} \tag{6.28}$$

$$V_t = \frac{h}{r} \tag{6.29}$$

$$V_s = \sqrt{V_t^2 + 2\mathscr{U}} \tag{6.30}$$

which are used to express the Dromo parameters ζ_{1-3}, and the transformation matrices $\mathbf{C}_{\mathscr{RI}}$ and $\mathbf{C}_0$:

$$\zeta_3 = \frac{1}{rV_s} \tag{6.31}$$

$$\zeta_1 = (V_s - \zeta_3)\cos\phi_0 + V_r \sin\phi_0 \tag{6.32}$$

$$\zeta_2 = (V_s - \zeta_3)\sin\phi_0 - V_r \cos\phi_0 \tag{6.33}$$

$$\mathbf{C}_{\mathscr{RI}} = \left(\frac{\mathbf{r}}{r}, \frac{\mathbf{h}}{h} \times \frac{\mathbf{r}}{r}, \frac{\mathbf{h}}{h}\right) \tag{6.34}$$

$$\mathbf{C}_0 = \mathbf{C}_{\mathscr{RI}} \mathbf{C}_\phi^\mathsf{T} \tag{6.35}$$

The quantity ζ_0 is simply the non-dimensionalized physical time. The initial value of t can be chosen arbitrarily, and in this study it is always set equal to 0. Note that $\zeta_3 \to \infty$ as $rV_s \to 0$, however, it can be assumed that this is not realized for the considered motion in the presence of a non-zero potential(see Eq.(6.30)) and radius $r >> 0$. The remaining elements can be found by using the transformation matrix $\mathbf{C}_0$:

$$\zeta_7 = \frac{1}{2}\sqrt{1 + \mathbf{C}_0(1,1) + \mathbf{C}_0(2,2) + \mathbf{C}_0(3,3)} \tag{6.36}$$

$$\zeta_4 = \frac{\mathbf{C}_0(3,2) - \mathbf{C}_0(2,3)}{4\zeta_7} \tag{6.37}$$

$$\zeta_5 = \frac{\mathbf{C}_0(1,3) - \mathbf{C}_0(3,1)}{4\zeta_7} \tag{6.38}$$

$$\zeta_6 = \frac{\mathbf{C}_0(2,1) - \mathbf{C}_0(1,2)}{4\zeta_7} \tag{6.39}$$

where $\mathbf{C}_0(i,j)$ denotes the element of $\mathbf{C}_0$ in the i-th row and j-th column. When $\zeta_7 = 0$ special formulas for the elements ζ_{4-6} have to be used, which can be found in Ref. [95].

6.4. METHODOLOGY

Dromo is proposed as a state model to further improve the propagation time to solution explosion. The use of a regularized formulation is here referred to as verified regularized interval orbit propagation (VRIOP). Cartesian coordinates are used to express the initial state and uncertainty and perform analysis after propagation, such as computing conjunctions. All initial uncertainties are assumed to be represented by intervals.

The simplest uncertainty transformation method is Monte Carlo (MC), where the uncertainty distribution (in this case an interval) is sampled to a sufficient degree and each individual sample is transformed to the propagation state model, to construct the new transformed distribution. For interval transformation, the minimum and maximum values in each dimension are taken to be the new intervals. MC intervals are non-verified as the obtained intervals only approach the true interval. Verified interval transformation techniques will be discussed in Sec. 6.4.1.

The physical time has become a dependent variable and thus has an uncertainty that will grow with propagation. The uncertainty in the time variable needs to be converted to additional position and velocity uncertainty. A new procedure for this is proposed in Sec. 6.4.2.

6.4.1. VERIFIED TRANSFORMATIONS

Verified transformation ensures that solution enclosure is maintained. Any IA technique can be used for the transformation and does not have to match the technique used for the propagation. For example, IA is used for the transformations and TM for the propagation in Ref. [118].

Transformations give rise to additional overestimation due to the non-linear equations. Also the transformation needs to be performed twice: once to the propagation state model and once more after integration, back to Cartesian coordinates. The overestimation introduced by the transformation results in a large additional uncertainty even

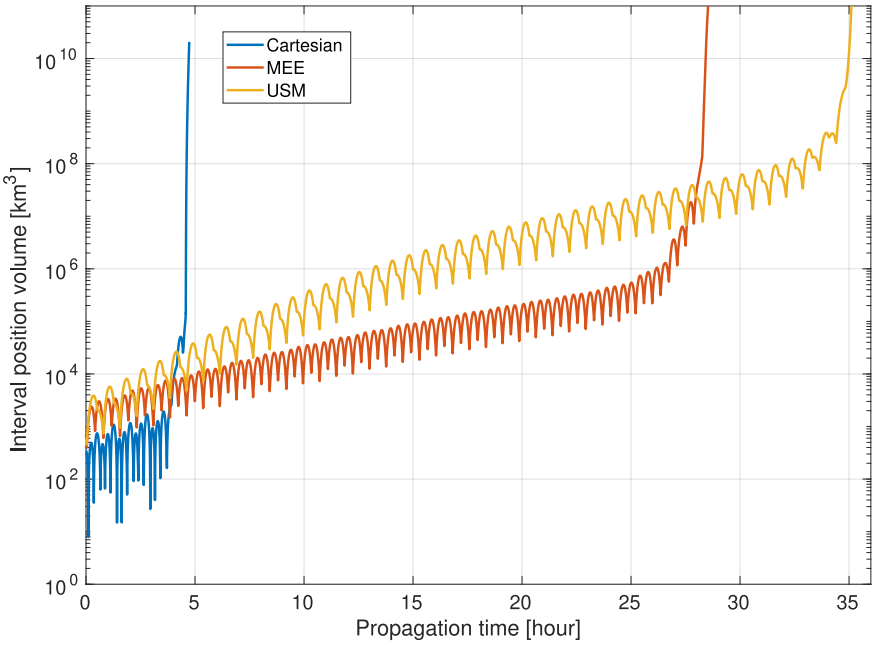

Figure 6.1: Position interval volume growth with propagation time for the Cartesian, MEE, and USM state models (reproduced from Fig.7 of Ref. [118]).

before any propagation is done and can even outweigh the benefits an alternative state model may provide. In Ref. [118] the MEE and USM are compared against Cartesian coordinates for the VIOP of a satellite in a circular orbit at 400 km altitude. The different solutions explode after a different time of propagation. To illustrate the effects of the transformations and the benefits of different propagation models, the results have been reproduced in Fig. 6.1. The results for Dromo will be directly compared to the same trial in Sec. 6.6.4.

Due to the additional uncertainty from the transformations, the Cartesian solution outperforms the MEE and USM until a propagation time of 4 h. The initial volumes of MEE and USM transformed back to Cartesian coordinates are 703 and 601 km^3, respectively. Considering that the initial uncertainty is only 1×10^{-6} km^3, the overestimation due to transformation is very large indeed.

Figure 6.1 shows once and twice-per-orbit oscillations of the volumes. For Cartesian coordinates the oscillation is by far the largest. These oscillations illustrate the overestimation due to wrapping in a Cartesian cuboid as the uncertainty is rotated along a full orbit.

IA transformations are shown to a produce large overestimation for MEE and USM [118]. IA and TM transformations are implemented in this research. TM transformations follow the same two-step approach as TM integration: a rough solution enclosure is first computed, which is then tightened using TM. The TM is expressed as a function of the original Cartesian initial interval conditions. Dependency arising from the transform-

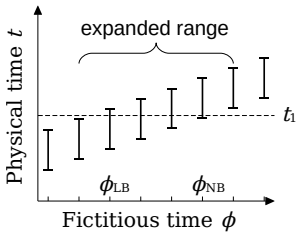

Figure 6.2: Proccess for selecting the range of ϕ for removing time uncertainty.

ation equations can be reduced when the tighter solution is computed, which helps to reduce overestimation.

6.4.2. TIME UNCERTAINTY TRANSFORMATION

Due to the time transformation that is included in Dromo ODEs, physical time is regarded as a state variable and therefore it is integrated along with the other seven Dromo parameters. From Eqs. (6.8) and (6.16) it is clear that the derivative of time with respect to ϕ depends on ζ_{1-3}. Any uncertainty in these variables results into a growing uncertainty in the physical time variable itself. An uncertainty in time is impractical for many applications. A process for obtaining only the position and velocity uncertainty at a specific time t_1 is outlined below.

The uncertainty of the physical time at a given ϕ is represented by the time interval $[\underline{t}, \bar{t}]$. Conversely, a desired time t_1 will be present in a number of solutions for various values ϕ. The first and last of the integrated solutions at ϕ_i $(i = 0, 1, \ldots, N)$ containing t_1 are denoted as:

$$\phi_{n_{LB}} = \min_i \phi_i \qquad \phi_{n_{UB}} = \max_i \phi_i \qquad \text{where } t_1 \in [\underline{t}_i, \bar{t}_i] \tag{6.40}$$

It is important to expand the range outward and include the neighboring solutions of ϕ on the lower and upper bound, such that all solutions between $\phi_{n_{LB}-1}$ and $\phi_{n_{UB}+1}$ are considered. Here $n_X + 1$ and $n_X - 1$ indicate the solutions after and before n_X, respectively. Although intervals t of solutions at $\phi_{n_{LB}-1}$ and $\phi_{n_{UB}+1}$ certainly do not contain t_1, it is not known which solutions in the ranges $[\phi_{n_{LB}-1}, \phi_{n_{LB}}]$ and $[\phi_{n_{UB}}, \phi_{n_{UB}+1}]$ might contain t_1. The resulting Cartesian volumes of the integrated solutions between $[\phi_{n_{LB}-1}, \phi_{n_{UB}+1}]$ need to be joined to get the total verified solution for a given time t_1. The process is illustrated in Fig. 6.2.

As VSPODE uses a variable step size, subsequent values of ϕ can be far apart. The large spacing results in overestimation in two ways. First, the *a-priori* solution, compared to the tight enclosure, is larger for large step sizes. Only the *a-priori* solution is valid over the ϕ range from one step to the next. Second, all solutions $\phi_{n_{LB}-1}$ until $\phi_{n_{UB}+1}$ have to be considered. At large step sizes, this will likely contain many solutions that do not include t_1. To overcome these issues a refinement is made. The integration is performed again from $\phi_{n_{LB}-1}$ to $\phi_{n_{UB}+1}$ by using a smaller fixed step size. This will produce smaller *a-priori* solutions and discard integration steps that do not contain t_1.

The procedure can even be repeated to further reduce the total volume, albeit at diminishing improvements (reduction of wrapping and narrowing the considered ϕ range) for a given reduction in step size. Each refinement does require additional integration steps and so presents a trade-off between volume and computational effort. On the whole, the number of integration steps required when refining once for a single time t_1 is likely small, compared to the total number of integration steps taken from t_0 to t_1. The optimal strategy for refinement will depend on the number of time-certain verified solutions required and depends on the application.

6.5. EXPERIMENTAL SET-UP

The experimental set-up of this study is similar to that of Ref. [118], to be able to compare the Dromo state model directly to the previously obtained results for MEE and USM. Only two uncertainty parameters are included in the study: the atmospheric-density uncertainty factor and the model-error acceleration. The uncertainty parameters and eight uncertainty state variables result in a total of ten uncertainty quantities ($N_u = 10$). These quantities are introduced and discussed in the following sections.

6.5.1. INITIAL STATE

Two initial uncertainty models are used: the simple and correlated model. In the simple model the initial uncertainty state is modeled as a uniform and uncorrelated six-dimensional distribution in the inertial Cartesian frame. The simple model is included to make the results more comparable to previous studies [118]. Also the initial widths are the same as in Ref. [118]: 10 m and 0.1 m s^{-1} in the position and velocity components, respectively. The magnitudes are realistic even for very-low orbiting satellites, depending on the measurement type considered [144].

The second correlated initial uncertainty model has two important distinctions: the uncertainties are expressed in the orbital frame and made correlated. The orbital frame is a common reference frame for expressing uncertainty in the state. Specifically, the transverse (or along-track) position uncertainty and radial velocity uncertainty, and radial position uncertainty and transverse velocity uncertainty are inversely correlated, as was demonstrated in Chapter 3.

To prevent wrapping the solutions twice, the entire conversion from the uncertainty in the orbital frame to Dromo is executed in one step. This is done by substituting the transformation equations from the orbital frame to the inertial Cartesian frame in the Cartesian to Dromo transformation equations presented in Sec. 6.3.2. Moreover, two inversely correlated variables are modeled only by a single initial uncertainty. The two variables are then simply defined as the positive and negative copy of this combined uncertainty variable. This approach reduces the number of uncertain variables and allows for cancellation.

6.5.2. ATMOSPHERIC DENSITY

As the research concerns LEO satellites, atmospheric drag needs to be accounted for. A simple tabulated exponential density model, based on U.S. Standard Atmosphere 1976 and CIRA1972 models, is used [145]. A spherical Earth and a co-rotating atmosphere are

assumed. The drag acceleration is modeled by:

$$\mathbf{f}_{drag} = -\frac{1}{2}\rho \|\mathbf{v}_{rel}\| \mathbf{v}_{rel} K \tag{6.41}$$

where the ballistic coefficient is defined as $K = 0.05 \times 10^{-6}\,\mathrm{km^2\,kg^{-1}}$ [118].

For LEO, atmospheric density is by far one of the most uncertain model parameters. To model this, a random unbiased error of ±20 % is assumed [38, 118, 146], see also Chapter 4. The atmospheric drag is modeled as an interval by multiplying the acceleration by an interval factor:

$$\mathbf{F}_{drag} = [0.8, 1.2]\mathbf{f}_{drag} \tag{6.42}$$

6.5.3. GRAVITY FIELD

Variations in the Earth's gravity field are modeled as a perturbing potential, having contributions to both the perturbing acceleration $\mathbf{f}$ and the potential $\mathscr{U}$. Accounting for oblateness only, the potential and acceleration are given by [143]:

$$\mathscr{U}_{J_2} = \frac{J_2 \mu R_E^2}{2r^3}\left(1 - 3\sin^2 i \sin^2(\nu + \omega)\right) \tag{6.43}$$

$$\mathbf{f}_{J_2} = -\nabla \mathscr{U}_{J_2} \tag{6.44}$$

where the following constants were assumed [147]: $\mu = 398\,601\,\mathrm{km^3\,s^{-2}}$, $R_E = 6371.22\,\mathrm{km}$, and $J_2 = 1.082\,65 \times 10^{-3}$. The uncertainty arising from the limited knowledge on the model parameters and limited order and degree of gravity terms are discussed in Sec. 6.5.5.

6.5.4. GRAVITATIONAL ATTRACTION OF THE MOON

The third-body gravitational attraction by the Moon is modeled. This is the only third-body perturbation considered, as the goal is to investigate the effect of this type of perturbation and not necessarily the contribution of different particular bodies. Moreover, the particular perturbation of the Moon is included in most regularized propagation studies [95, 105, 125, 147], but not in the previous study [118]. The third-body perturbation depends explicitly on the physical time, so that the uncertainty related to this variable appears explicitly in the EOMs. This perturbation is implemented in Dromo as derived from a perturbing potential. The perturbing acceleration and the Moon's position in the Earth-centered inertial frame are:

$$\mathbf{f}_M = -\frac{\mu_M}{r_{sM}^2}\mathbf{r}_{sM} \tag{6.45}$$

$$\mathbf{r}_M = -\frac{1}{2}Q\left[2\sin(\omega t), \sqrt{3}\cos(\omega t), \cos(\omega t)\right] \tag{6.46}$$

where $Q = 384\,400\,\mathrm{km}$, $\omega = 2.665\,315\,780\,887 \times 10^{-6}\,\mathrm{rad\,s^{-1}}$, and $\mu_M = 4902.66\,\mathrm{km^3\,s^{-2}}$. The distance vector $\mathbf{r}_{sM} = \mathbf{r}_M - \mathbf{r}_s$ can be obtained from Eqs. (6.21) and (6.24). The computation of the potential $\mathscr{U}_M$ and the perturbing accelerations is straightforward. The partial derivative of the potential is:

$$\frac{\partial \mathscr{U}_M}{\partial t} = \frac{1}{2}\mu_M \omega Q \left(\frac{2cR_x + \sqrt{3}R_y + sR_z}{Q^3} - \frac{2ca_X + \sqrt{3}sa_Y + sa_Z}{\left(a_X^2 + a_Y^2 + a_Z^2\right)^{3/2}} \right) \tag{6.47}$$

where $a_X = R_x - sQ$, $a_Y = R_y + \frac{1}{2}\sqrt{3}cQ$, $a_Z = R_z + \frac{1}{2}cQ$, $s = \sin(\omega t)$, and $c = \cos(\omega t)$.

6.5.5. MODELING ERRORS

The model only includes a limited number of perturbations with a limited fidelity. Moreover, all model parameters (e.g., physical quantities μ and J_2) are only known approximately. To account for both, these contributions are combined into a single additional modeling error acceleration vector, where each component is estimated to be enclosed within $[-10^{-8}, 10^{-8}]\,\mathrm{km\,s^{-2}}$ [118, 148].

It could be beneficial to include unmodeled contributions to the gravity field as an uncertainty interval on top of the J_2 parameter. Dromo treats perturbations arising from a potential separately from other perturbing accelerations. In this way, an uncertainty in a conservative potential will not cause a growth in uncertainty in orbital energy. However, practically this means the introduction of another uncertainty parameter, which significantly affects the computational efficiency and is therefore not included in this study.

6

6.6. RESULTS

The study investigates TM transformation, a correlated initial interval uncertainty model, and Dromo as a propagation state model. As a result of the chosen state model, a method for removing the time uncertainty by converting it to additional positional and velocity uncertainty is developed. The results of the transformation are separated in the wrapping effect and dependency problem, presented in Secs. 6.6.1 and 6.6.2. The different initial uncertainty models are compared in Sec. 6.6.3. In Section 6.6.4, Dromo is compared against previous state models. The integration of the time uncertainty is detailed in Sec. 6.6.5. Finally, a sensitivity analysis is presented in Secs.6.6.6-6.6.8.

6.6.1. TRANSFORMATION WRAPPING EFFECT OVERESTIMATION

By using a different state model for the propagation, overestimation is unavoidable and mainly due to two sources: wrapping and dependency. The overestimation due to wrapping represents how much an interval cuboid in one state space remains cuboid in another state space and results from the choice of state models. The overestimation due to dependency measures the complexity of the transformation and also depends on the verified transformation technique.

To better understand the effect of the transformation technique, the wrapping contribution is investigated first. The initial interval state in Cartesian coordinates is transformed to a Dromo initial interval and back. In this process the Cartesian cuboid is wrapped inside a Dromo cuboid, and then wrapped back in a Cartesian cuboid. To negate the dependency problem of the transformation method, the MC method is used for both transformations using 10 000 samples. Figure 6.3 shows the final interval compared

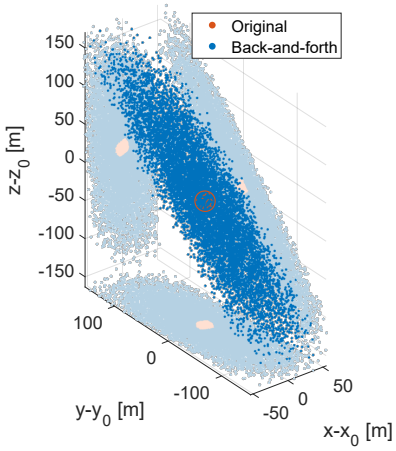

Figure 6.3: MC transformation of the initial uncertainty interval from Cartesian to Dromo and back around the initial position at t_0.

to the original interval. The relative growth with respect to the nominal state (x_0, y_0, z_0) at t_0 is shown.

It can be seen that the initial interval has grown significantly. The final interval has a large spread in the XY- and XZ-plane, but occupies a relatively narrow band in the YZ-plane, causing most of the overestimation due to wrapping of the final Dromo to Cartesian transformation. The shape of the final point cloud appears normally distributed in the three dimensions, while the original point cloud was a cuboid of even density. This change is caused by the transformation equations, in which certain combinations of values are physically not compatible.

The volume of the back-and-forth result is estimated to be $2.48 \times 10^{-3}\,\mathrm{km}^3$ by drawing a convex hull around the samples, while the corresponding cuboid measures $11.12 \times 10^{-3}\,\mathrm{km}^3$. The overestimation due to wrapping is thus a factor 4.48. In a similar fashion, the overestimation of the velocity volume is by a factor 3.36. These factors are small compared to the overestimation due to dependency and thus the total overestimation. Nonetheless, wrapping occurs at every integration step. This illustrates the downside of verified propagation in Cartesian space. The ellipsoid rotates 360 deg every orbit and is wrapped by a Cartesian cuboid at each step.

To investigate the wrapping in the Dromo space the volume of the samples is estimated by fitting a three-dimensional and four-dimensional convex hull around ζ_{1-3} and ζ_{4-7}, respectively. The volume of the convex hull is compared to the volume of the cuboid interval to obtain an overestimation factor. The obtained (hyper)ellipsoid volumes are extremely small compared to the cuboid volumes and nearly zero. Due to limited machine precision, computing an exact overestimation factor is nonsensical, so it can only be noted that the overestimation due to wrapping is very significant.

Comparing the wrapping effect of the transformation from Cartesian to Dromo, and also Dromo back to Cartesian, the major part of the wrapping effect is caused in the initial transformation. Nevertheless, the overestimation due to wrapping is still 300 times

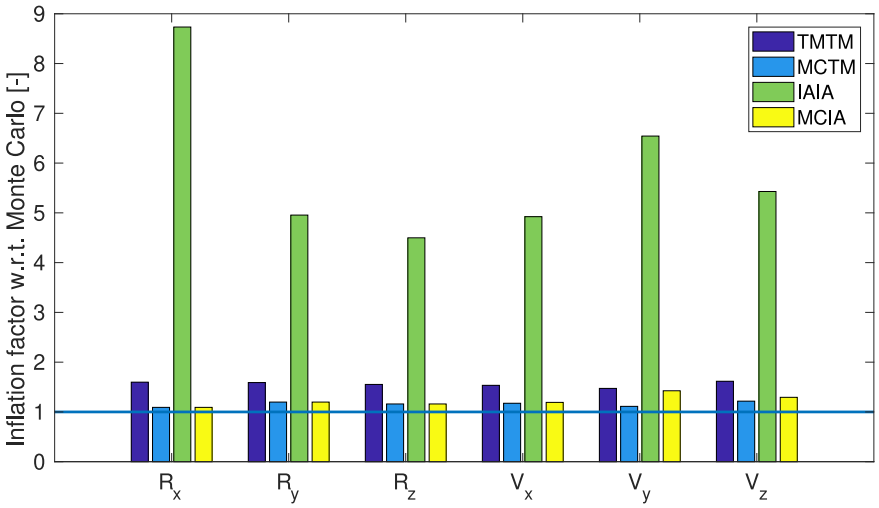

Figure 6.4: Inflation factor of the initial uncertainty interval with respect to MC for both directions, using TM for both directions (TMTM), TM only for Dromo back to Cartesian (MCTM), IA for both directions (IAIA), and lastly IA only for the transformation back to Cartesian (MCIA).

smaller compared to the same transformation for USM and MEE [118].

6.6.2. TRANSFORMATION DEPENDENCY PROBLEM OVERESTIMATION

The second source of overestimation due to transformation is the dependency problem, which depends on the interval technique used. In Ref. [118], standard IA is used for both directions of the transformation between Cartesian and Dromo variables. For this study TM transformations are implemented and compared against IA. To differentiate between both directions of transformation, the verified methods are used for the entire forth-and-back transformation and also starting from the previous MC interval solution in Dromo state space. The MC solution, which already accounts for the wrapping effect, is used as a baseline for the transformation. For the TM transformations, a TM order of $q = 4$ and tolerance of $\epsilon = 10^{-16}$ are used. The result of the comparison is shown in Fig. 6.4.

The figure shows the interval inflation factor as the transformed Cartesian interval width divided by the MC interval width obtained earlier. The inflation factor of the Cartesian coordinates is between five and nine when IA is used for both transformations. The inflation in x-direction is largest, which is approximately in the cross-track direction in this particular example. Overall, the inflation is roughly similar for each of the Cartesian components. Comparing the different techniques, TM transformation provides significantly better results than IA and is close to the MC transformation. The final position volume of the TM solution is four times the MC volume, compared to an increase of a factor 195 for IA.

Both techniques perform significantly better on the Dromo-to-Cartesian transformation than vice-versa, as illustrated by the MCTM and MCIA results. This further indicates that the initial transformation introduces the most overestimation. The final

Cartesian position volumes of MCTM and MCIA are both 152 % larger than MCMC. The velocity volumes are larger than the position volumes for both techniques, with also a larger difference between the two: 220 % for MCTM and 435 % for MCIA compared to MCMC.

The significantly smaller volumes for MC suggest that applications where the initial conditions are obtained from empirical data would benefit from transforming the data to the propagation state model directly, before computing the initial intervals. In conclusion, the final volume of the TM transformation, back to Cartesian space, is $0.044\,\mathrm{km}^3$, which is roughly four orders of magnitude larger than the initial volume of $1 \times 10^{-6}\,\mathrm{km}^3$. Much of the overestimation is due to the inherent wrapping effect of the chosen Dromo state model. This is unavoidable, when the model is used for propagation. Nonetheless, this is four orders of magnitude smaller than the starting volumes of the MEE and USM state models used in Ref. [118], as shown in Sec. 6.4.1.

6.6.3. INITIAL INTERVAL MODELS

The correlated initial uncertainty model assumes a dependency between uncertainty in the state variables. The marginal distributions and thus intervals remain exactly the same as the simple (uncorrelated) model. The usage of fully correlated variables reduces the number of uncertain variables, simplifying the transformation problem and allowing for additional cancellation and removal of dependency when the tighter enclosure is computed. To compare the effect of correlated uncertainty among variables, the uncertainties in the transverse position and radial velocity, and radial position and transverse velocity are assumed to be correlated with a correlation coefficient $\rho = -1$ [82]. This reduces the number of uncertain parameters from six to four.

To benefit from this reduction, the entire initial uncertainty transformation from the orbital frame to inertial Cartesian coordinates and Cartesian coordinates to Dromo elements is combined into a single transformation. The correlation is not carried on through the propagation and only affects the first transformation, which was previously shown to cause the largest overestimation. A reduction in width of all Dromo elements, compared to the uncorrelated situation, is observed. The interval width of the elements is reduced by a factor between 1.3 and 4.4. This reduction is quite significant, considering that the marginal distributions are identical. The correlated samples have roughly similar orbital energy and thus produce smaller initial Dromo intervals. Transformed back to Cartesian coordinates, the resulting position and velocity volumes are a factor 1.7 and 1.9 smaller, when correlations are introduced.

6.6.4. COMPARISON WITH OTHER STATE MODELS

Two initial uncertainty models are used for the comparison. The first is the simple initial uncertainty model, which is also used for MEE and USM in Ref. [118]. However, this model gives much smaller starting intervals when using TM transformations with Dromo compared to Ref. [118], in which IA transformations were used for both state models. To account for this, a second model is introduced that inflates the initial Cartesian uncertainty by a factor 25, such that the forth-and-back Cartesian position volume is $688\,\mathrm{km}^3$ and roughly equal to that obtained with MEE and USM. In this way differences between Dromo x25, MEE, and USM are due to the propagation stability only.

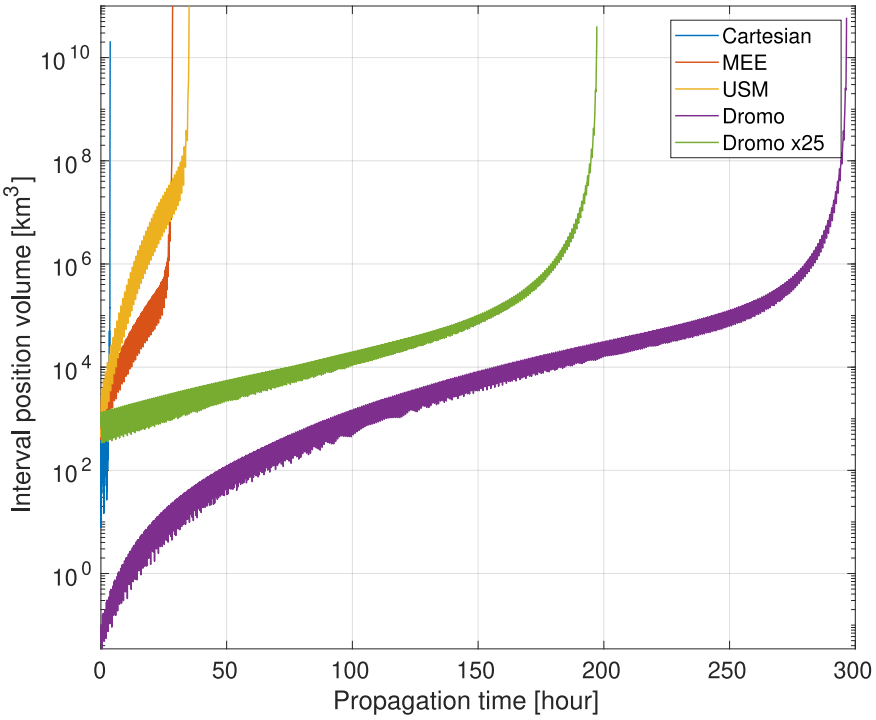

Figure 6.5: Position interval volume growth with propagation time for the Cartesian, MEE, USM, and Dromo state models.

The verified orbit is propagated until solution explosion, for both initial uncertainty models and compared to the previous values shown in Fig. 6.1. The settings for VSPODE are as follows: $q = 3$, $k = 16$, and $\epsilon = 10^{-14}$. These settings (or tuning parameters) were introduced in Sec. 6.2.3. The comparison with Cartesian, MEE and USM state models is shown in Fig. 6.5.

Dromo with the uncorrelated TM initial volume is able to propagate for almost 300 hours until interval explosion, whereas the Dromo x25 model is able to propagate for almost 200 hours. This is much longer that the previously obtained durations of 5, 30, and 35 hours for Cartesian, MEE, and USM, respectively. Dromo is able to provide a stable verified propagation, which is at least five times longer with respect to that obtained with the other state models. For applications, such as conjunction analysis, this allows a significantly longer forecasting period.

6.6.5. TIME TRANSFORMATION

A Dromo interval solution at a given ϕ has an uncertainty in both Cartesian coordinates and time. For most analyses, this time uncertainty is often undesirable. To construct an interval of position and velocity only for a given epoch, a range of integrated solutions needs to be considered. The developed process was discussed in Sec. 6.4.2. A target epoch of $t_1 = 10\,\text{h}$ is chosen for the x25 Dromo propagation. The first integrated solution

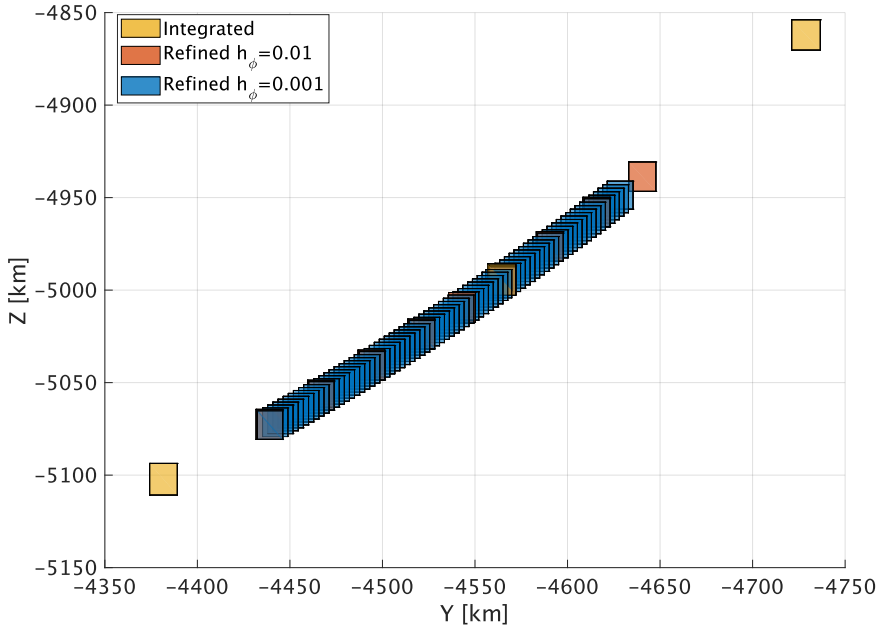

Figure 6.6: Interval solutions of the variable step-size integration and two refinements around the target time t_1 of 10 hours.

containing t_1 has a time interval width of $w(t) = 62.4\,\text{s}$ and is shown in Fig. 6.6. The interval solutions are shown as the result of three levels of refinement. The third refined level with step size $h_\phi = 0.001$ is considered the final and desired Cartesian interval.

In the first unrefined level, the total Cartesian interval is obtained by finding all integrated solutions that contain t_1 and expanding the range of solution outward. Although the two outer integrated solutions do not contain t_1, they are included, as it cannot be known which solutions in-between do contain the target time. The downside of the result from the first unrefined level is that it produces large overestimation when joined. As the step size is large, the range in ϕ is also large. A better result is obtained when the step size is refined.

For the second level (now including refinement), the integration is restarted at each of the previous integrated solutions and propagated to the next with a fixed step-size of $h_\phi = 0.01$. The process of selecting only the integrated solutions that contain the target time and the expansion of the range is repeated. As a result of the finer spacing, 6 out of the 15 new solutions are discarded, giving a narrower range in ϕ.

For the third level, the same process of refinement is repeated, but with an even finer step size of $h_\phi = 0.001$. Out of the 78 solutions, 73 contain t_1 or are at the boundaries. A further refinement can be made, if required. To obtain the final verified Cartesian interval at the specified time t_1, the *a-priori* solutions of each of the 73 solutions are joined.

A major advantage of this method is that the final verified Cartesian interval consists of a large number of individual solutions, allowing for more complex shapes than a single

six-dimensional interval cuboid. In many cases, such as in this example, a single cuboid would have a large overestimation due to wrapping: a single cuboid wrapping all 73 sub-intervals is 3.5×10^7 km^3, compared to 1.4×10^5 km^3 for a union of the sub-intervals, as estimated by fitting a convex hull around all the corner coordinates. The overestimation due to wrapping is almost a factor 250.

The large cuboid and the set of smaller ones can be used for further analysis, including conjunction analysis. For instance, if an intersection between the large cuboid of two objects is detected, a more refined comparison between the respective smaller cuboids can be made. The process of computing interval intersections and collision predictions is treated in Ref. [118].

The shown intervals are nearly square in the $yz-$plane and very small in the along-track direction, even if this direction contains most of the uncertainty. By studying the contribution of Dromo elements on the positional uncertainty, it is found that the along-track uncertainty is almost entirely absorbed by the time uncertainty. So while the ODE of this element is directly dependent on other elements, it has only a marginal effect on the overall system through the third-body perturbation of the Moon. This allows the regularized formulation to remain stable for so long.

6.6.6. SENSITIVITY OF THE PROPAGATION TIME TO TUNING PARAMETERS

This section describes the different tuning parameters and how they affect the propagation using Dromo and is followed by a sensitivity study. For certain combinations of the tuning parameters, VRIOP sometimes produces significantly worse results, despite only small changes to the parameters, creating plateaus of *successful* combinations in the tuning-parameter space. This instability has been noted in Ref. [118] and will be demonstrated and discussed further.

The ITS order k presents a trade-off between computational efficiency and numerical sensitivity. A high value of k tends to be much more computationally efficient. At higher orders the step-size can often be made very large, at the cost of introducing numerical sensitivity in the higher-order terms. The coefficients of the higher-order terms become very small, while the independent variable is raised to a high exponent. Also, in practice, a satellite orbit model is only continuously differentiable by approximation. For instance, the atmospheric density results from a tabulated model. This trade-off holds true for Taylor-series integration of satellite trajectories in general [149]. Ref. [134] also notes a worsening in breakdown time on the Lotka-Volterra problem for increasing order k. The larger steps result in a slight increase in overestimation in the tightened solutions and thus shorter propagation time until explosion.

A higher TM order q generally results in a higher accuracy and longer propagation time until explosion, at the cost of numerical efficiency and sensitivity. The computational cost is roughly raised to the power of $N_u q$, where N_u is the number of uncertain quantities (state variables and model parameters). As q increases, the success of a run becomes very sensitive to the other parameters and initial conditions.

Finally, the numerical tolerance ϵ directly drives the step-size control. Due to the large model uncertainty and overestimation, the numerical accuracy has only a small effect on the solution and thus time until interval explosion. However, it still significantly impacts the computational efficiency. Also, the numerical tolerance generally needs to

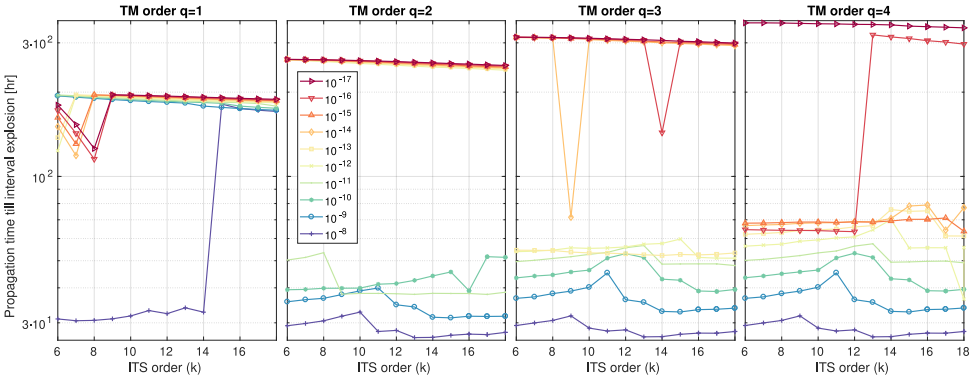

Figure 6.7: Sensitivity of propagation time to various combinations of the tuning parameters: TM order q, ITS order k, and tolerance ϵ.

be large for high values of q, to produce successful runs.

The following ranges of parameters are investigated: $k \in [6, 18]$, $q \in [1, 4]$, and $\epsilon \in [10^{-8}, 10^{-17}]$. Also $q = 5$ and 6 were considered, but no successful results could be obtained even with very tight tolerances. Moreover, tighter tolerances such as $\epsilon = 10^{-18}$ and 10^{-19} produced results similar to 10^{-17}, at higher computational cost. Tolerances beyond 10^{-16} are below double precision, however the VSPODE solver produces different solutions for all mentioned tolerances, suggesting different behavior of the step-size control algorithm. This is especially clear for order $q = 4$, as will be demonstrated.

Figure 6.7 shows the result of the propagation time in hours until interval explosion for a range of tuning parameters. The best propagation results are obtained for the TM order $q = 4$, with the ITS order $k = 8$ and tolerance $\epsilon = 10^{-17}$. The resulting propagation time until interval explosion is 354 h.

From the graphs it can be seen that an increase in the TM order results in a longer propagation time. The relative increase in additional propagation time with increasing order q is 24 % ($q = 2$ to 3), 20 % ($q = 3$ to 4) and 12 % ($q = 3$ to 4). The gain in additional propagation time thus seems to converge. There exists a clear separation in propagation time between successful and unsuccessful combinations of the tuning parameters, which is roughly a factor 5. The number of successful solutions decreases with the TM order q. Moreover, no successful runs for orders 5 and 6 were obtained within the given parameter space.

It can further be seen that the propagation time decreases slightly with increasing integration order. This is due to overestimation remaining after computing the tighter enclosure, also noted in Ref. [134]. The decrease from order $k = 6$ to 18 is less than 5 %. For certain choices of the tuning parameters, k is important in achieving successful runs. Some drops in lines of solutions with varying k can also be observed for $q = 1$ and 3. For the former there is a clear pattern. This phenomenon is also observed by Ref. [118]. These solutions are only slightly unstable, within a stable region of the tuning-parameter space.

The numerical tolerance has little effect on the actual propagation time amongst successful runs, especially below the value of $\epsilon = 10^{-12}$. More stringent tolerance settings are

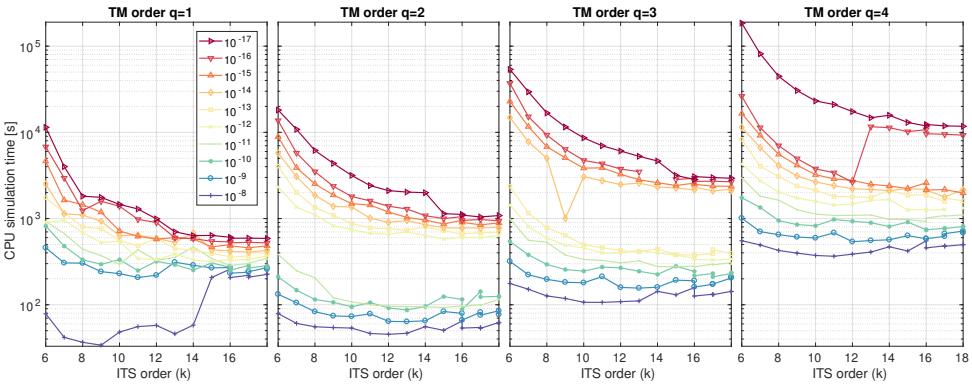

Figure 6.8: Sensitivity of CPU simulation time to various combinations of the tuning parameters: TM order q, ITS order k, and tolerance ϵ.

required to produce successful runs of higher orders of q.

Without performing a computationally costly survey of the tuning parameter space, it is advised to start with a low TM order, combined with high ITS order and medium tolerance, for example, $k = 16$ and $\epsilon = 10^{-14}$. Such a combination tends to produce the most robust results and is also computationally favourable (as will be discussed next).

6

6.6.7. SENSITIVITY OF CPU TIME TO TUNING PARAMETERS

The corresponding CPU simulation time to obtain the results of Fig. 6.7 are shown in Fig. 6.8. The sensitivity study is entirely performed on an Intel i7-4712HQ CPU at 2.30 GHz with a maximum Turbo frequency of 3.30 GHz.

There is a wide spread of CPU simulation time and there is still a clear separation between successful and unsuccessful runs, although the distinction is less pronounced. The relationship between propagation time until explosion and CPU simulation time is strongly non-linear. For instance, the solution with the best result (longest propagation time of 352 h) took 185 092 s (or 51.4 h), while the successful solution that required the shortest computation time was obtained with $q = 1$, $k = 16$ and $\epsilon = 10^{-8}$ and took a total of 225 s to complete for a propagation time of 172 h. Therefore, increasing the propagation time by a factor two comes at the expense of increasing the computational cost by a factor 323.

The ITS order k also has a strong effect on the computational cost, which is inversely related to the order. Comparing the solutions obtained with order $k = 6$ and 18, the decrease in computational cost is roughly a factor 18 for all TM orders, considering only the successful runs. The propagation time until explosion only marginally decreases, while providing more successful solutions. So, higher orders of k are recommended. Small values of k should be considered when a dense history of solutions is desirable.

Finally, a good trade-off for the numerical tolerance is more difficult to obtain. In contrast to the propagation time, there is quite a significant spread among the different tolerance settings for a given value of q. More stringent tolerances significantly increase the computational load at almost no improvement in propagation time. The least strin-

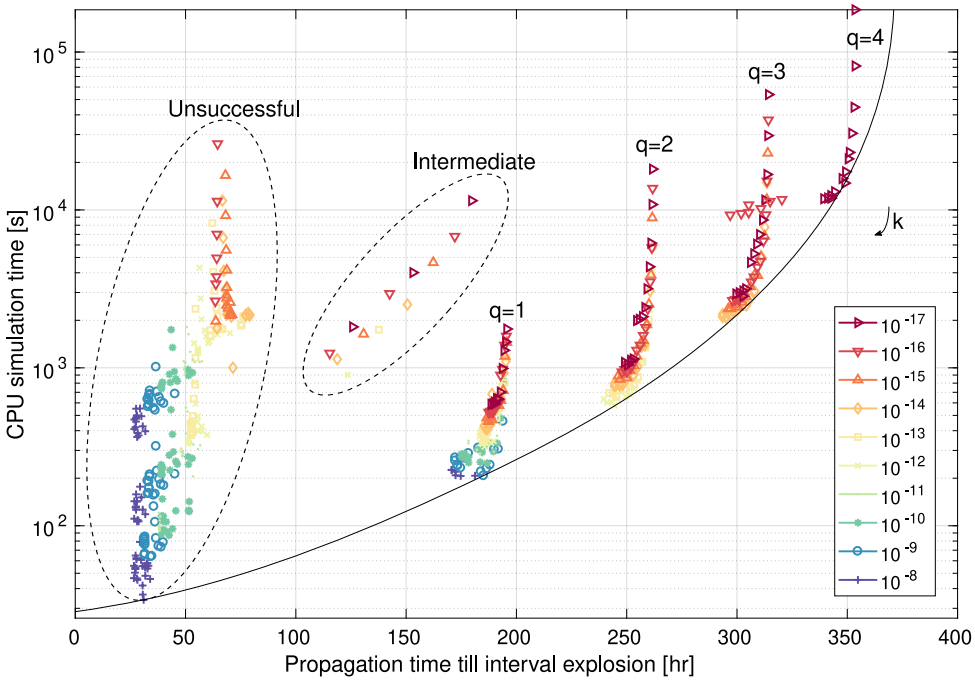

Figure 6.9: CPU simulation time compared to propagation time for various combinations of the tuning parameters: TM order q, ITS order k, and tolerance ϵ.

gent tolerance for a given combination of k and q, while producing successful results, is thus most favorable. The CPU simulation time decreases with increasing ITS order k. Also, high values of TM order q require more stringent tolerances.

6.6.8. CPU TIME VERSUS PROPAGATION TIME

To better understand the trade-off between solution stability and computational effeciency, the same results as shown in Figs. 6.7 and 6.8 are combined to construct a Pareto front shown in Fig. 6.9.

A line is fitted to approximate the Pareto frontier, solutions to the bottom and/or right of this line are likely to be infeasible. The groups of successful solutions belonging to each of the TM order q are clearly identifiable and separated. Varying order k creates hockey-stick patterns, with increasing order towards the bottom. The only exceptions are some solutions with $q = 4$, $\epsilon = 10^{-16}$, which are intersecting the group of solutions obtained with $q = 3$.

The unsuccessful solutions are also clearly separate from successful solutions. Groups of constant order q of unsuccessful solutions are less distinct, due to the invariance of propagation time with q for this group. So, if the propagation time until solution explosion does not improve with increasing order q, it can be that only unsuccessful solutions are generated.

The intermediate solutions are also a distinctly separate group. These present solu-

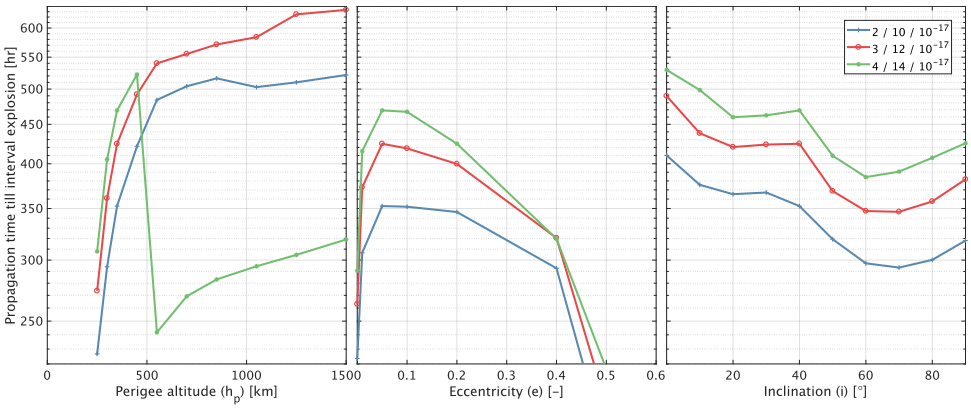

Figure 6.10: Sensitivity of propagation time to orbital parameters.

tions that are generally within a successful region of the tuning-parameter space, but perform worse than neighboring solutions. These are also visible in Fig. 6.7 and previously discussed. The figure further confirms that even higher orders of q will likely only produce unsuccessful runs or only a small improvement in propagation time at a large computational cost.

6

6.6.9. ORBITAL SENSITIVITY

To further investigate the sensitivity of the propagation time, a study across various orbits is conducted. The perigee altitude h_p, eccentricity e, and inclination i are varied. The initial uncertainty remains the same in each case. The various choices for the orbital parameters are:

$$
\begin{aligned}
h_p &\in \{250, 300, 350, 450, 550, 700, 850, 1050, 1250, 1500\} \\
e &\in \{0.0001, 0.01, 0.05, 0.1, 0.2, 0.4, 0.7, 0.9, 0.95, 0.99\} \\
i &\in \{0, 10, 20, 30, 40, 50, 60, 70, 80, 90\}
\end{aligned}
$$

To limit the number of runs, the orbital parameters are varied only one parameter at a time with respect to a nominal orbit: $h_p = 350\,\text{km}$, $e = 0.05$, and $i = 40°$. So 28 simulations are performed for three sets of tuning parameters. Following the results of Secs. 6.6.6 and 6.6.7, the following combinations of $q/k/\epsilon$ are investigated: $2/10/10^{-17}$, $3/12/10^{-17}$, and $4/14/10^{-17}$. The results of this study are shown in Fig. 6.10.

Looking at the perigee altitude, the propagation time until solution explosion initially strongly grows with increasing altitude, which is explained by the reduction in atmospheric density and the diminishing effects of the oblate gravity model. Above 550 km the rate of increase is milder. For the setting $4\,/\,14\,/\,10^{-17}$, no successful solutions were obtained beyond 450 km. Several values of k and ϵ were seen to not avail. It is clear that a complex TM with a high order increases the propagation time until explosion, but also results in a more sensitive solution. For higher orbits, it is advisable to not model the

atmospheric density separately, but to include it in the combined uncertainty acceleration, as discussed in Sec. 6.5.5. For the other two settings, the propagation continues to increase with h_p; the maximum propagation time achieved is 633 h.

Considering the orbital eccentricity, the propagation time is improved with increasing order, which is to expected. At the altitude of the nominal orbit all three settings are equally stable. Slightly eccentric orbits ($e = 0.05$) produce more stable solutions than nearly circular orbits ($e = 0.0001$). Results are obtained to about an eccentricity of 0.4, where the propagation time is 25 % less than at $e = 0.05$. Instead of the tabulated atmosphere model, a continuously differentiable model could be used when the orbit is very eccentric [149].

Finally, looking at the inclination, there is a clear and similar trend for each of the three settings. Compared to the maximum propagation time at 0° inclination, the minimum is about 28 % lower and occurs between $i = 60°$ and 70°. The propagation time increases again towards $i = 90°$. This dependency is caused by the oblate gravity field. Perturbations to the orbital plane due to the J_2-term are known to have the largest magnitude between $i = 45°$ and 90°. For the values of eccentricity and perigee altitude of the nominal orbit, the variation in inclination has no effect on the solution stability.

The different settings presented here and many more attempted in trial and error, further illustrate the sensitivity of VRIOP to its tuning parameters, especially for higher values of the TM order q. To achieve a robust set of tuning parameters across a different range of orbital parameters, a trade-off between propagation time, computational cost, and sensitivity needs to be made. From the wide range of values studied, the following settings are recommended: $q = 3$, $k = 12$, and $\epsilon = 10^{-17}$.

6.7. CONCLUSIONS

The proposed Dromo state model and Taylor Model (TM) transformation method for the verified interval orbital propagation (VIOP) result in a much more stable state model, compared to previously investigated models. For comparison, a satellite in a circular low-Earth orbit (LEO) at 400 km is propagated, including perturbations caused by the atmosphere and the oblate gravity field. Dromo is able to propagate for almost 300 h until solution explosion, compared to 5, 30, and 35 h for Cartesian, MEE, and USM, respectively. This result is due to a smaller initial uncertainty volume and better propagation stability. Starting from a comparable initial uncertainty volume the resulting propagation time is nearly 200 h.

Wrapping of the Cartesian intervals in the Dromo space is found to be the primary source of overestimation in the transformation. Wrapping of Dromo intervals back in Cartesian space inflates the position and velocity volumes by a factor 4.5 and 3.4, respectively. TM transformation produces significantly less overestimation than interval analysis (IA) transformation. The total initial positional uncertainty overestimation is reduced by a factor 1600 compared to previous studies. Compared to Monte Carlo (MC) (i.e., overestimation due to dependency only), the position volumes of a back-and-forth transformation using TM and IA are 4 and 195 times larger, respectively. When both TM and IA are used to only transform the intermediate MC result back to the Cartesian space, the resulting inflation is only 1.5 for both. This shows that the Cartesian-to-Dromo transformation introduces most of the overestimation.

The uncertainty in the time state variable is initially zero, but is shown to quickly grow in interval width and to acquire much of the uncertainty present in the along-track direction. This allows for a very good representation and absorption of the orbital uncertainty. Moreover, it improves the stability of the integration, as the physical time has only marginal influence on the other elements.

To remove time uncertainty from the verified solutions a process for transforming it into additional position and velocity uncertainty has been proposed and demonstrated. To remain verified, the solution needs to consider a wide range of ϕ, which introduces additional overestimation. This overestimation can be reduced by re-integrating sections of the trajectory with a finer and fixed step-size $\Delta\phi$.

A study has been conducted to analyze the sensitivity of verified regularized interval orbit propagation (VRIOP) to tuning parameters: the Taylor-expansion order of integration k, the TM order q, and the numerical tolerance ϵ. The propagation time until solution explosion is found to vary between 172 h and 354 h for a LEO satellite. Generally, the propagation time increases with a higher TM order q, but at a diminishing rate, increasing 24, 20 and 12 % changing q from 1 to 4. The propagation time is slightly negatively correlated with the expansion order k of the integration: less than 5 % from $k = 6$ to 18. The propagation is hardly affected by the numerical tolerance ϵ, especially below 10^{-14}.

Certain regions of the tuning space are shown to produce many unsuccessful solutions, which generally abort integration at 15 % of the propagation time, compared to neighboring successful solutions. Higher TM orders q are more sensitive and require more stringent tolerance settings and higher values of ITS order k. No successful solutions are obtained for order $q = 5$ and higher. For unsuccessful runs the propagation time does not vary with q and can serve as indication of an unsuccessful region of the tuning-parameter space.

The CPU time is found to have a large spread for all tuning parameters, varying from minutes to days in length. The CPU time increases to a power of q, is inversely proportional to the numerical tolerance, and exponentially decays with k. Considering the small impact of k and ϵ on the propagation time and the diminishing return with increasing values of q, the following settings are recommended: $q = 3$, $k = 12$, and $\epsilon = 10^{-17}$.

Finally, the sensitivity to the perigee altitude, eccentricity and inclination were investigated. For nearly circular orbits, a higher altitude results in increased propagation time up to 633 h at $h_p = 1500$ km. The TM order $q = 4$ is not able to provide successful solutions beyond $h_p = 450$ km. This is likely due to overmodeling of the increasingly unperturbed motion. The removal of the atmospheric density as an uncertain parameter is then recommended. Eccentricities beyond $e = 0.4$ did not produce any satisfactory results, which is likely due to solution steps far transcending the altitude brackets of the tabulated atmosphere model. For the inclination, there is a variation of 28 % in propagation time with respect to the maximum at $i = 0°$, but viable solutions are obtained over the entire range.

The propagation time of VRIOP is almost 10 times longer than previously obtained in literature. The maximum forecasting window of verified solutions ranges from several days to nearly a month, depending on the integrator settings, orbital regime, and initial uncertainty. Thus Dromo greatly increases the applicability of VRIOP to conjunction

analyses and other SSA activities, especially where verified solutions are required or can provide additional advantages.

7

CONCLUSIONS AND RECOMMENDATIONS

The thesis concerns the problem of accurately quantifying and predicting space-debris trajectories. This has been investigated with a focus on the error modelling, estimation and propagation of space-debris orbits for the purpose of improving space-situational awareness (SSA) predictions, including short-term re-entry predictions and conjunction analysis.

Chapters 2 to 6 have presented the work that addresses the various research questions. The overarching conclusions that answer these questions will be given in Section 7.1. Section 7.2 presents recommendations on topics for future research.

7.1. CONCLUSIONS

The aim of the research is:

> **To improve space-debris orbit prediction and analysis, to facilitate reducing the number of potential satellite collisions and improving re-entry and impact location forecasting.**

The primary focus is on low-Earth orbit (LEO), which contains the vast majority of space debris, and on using actively maintained and publicly available data sources, covering the broad spectrum of orbits.

The primary research question is:

> **What aspects of space-debris trajectory modelling and propagation impact the quality of space-debris orbit predictions?**

The following sections address this primary and the derived research sub-questions.

7.1.1. SPACE-DEBRIS SITUATIONAL AWARENESS

> **What space surveillance data sources on space-debris orbits are available, how do they come about, and how are they disseminated?**

To better understand SSA trajectory predictions, it is important to understand how space-debris objects are tracked, and how their orbital state and related physical characteristics are determined from such observations using estimation models. The primary focus here is on Two-Line Elements (TLEs) that are published in the satellite catalogue (SATCAT) and maintained by the United States Space Command (USSPACECOM). SATCAT remains the largest source of publicly available ephemeris.

What are the primary gaps and limitations of these data for performing space-debris analysis and predictions?

Two challenges in SSA have been identified: the growing number of objects that need to be tracked and the quality of the trajectory data. Although the number of objects in space is rapidly increasing, there is a trend in Space Surveillance and Tracking (SST) to meet this demand in a number of key ways. More nations and commercial entities are developing SSA capabilities. New radars with a high capacity for tracking a large number of objects have become operational. These new sensors are also capable of tracking much smaller objects than previously possible, below 10 cm in LEO. The sensor locations are in regions, such as the southern and eastern hemisphere, where the coverage was historically limited. The sensors have the ability of integrating in existing networks, such as the Space Surveillance Network (SSN).

The primary challenge for SSA activities is the data availability and format. Especially, the continued use of TLEs is troublesome due to the limited accuracy and the lack of covariance information, and satellite parameters, such as parameters for the atmospheric drag, solar radiation pressure and attitude. The primary contributor to the accuracy of TLEs is the underlying analytical Simplified General Perturbations model (SGP4), which is necessarily used for both estimation and propagation of all TLEs. SGP4 has a history of 40 years (status 2020) and remains in place for more practical rather than scientific and technological reasons. Since 2013, a new step in the process of estimating TLEs was introduced, creating an undocumented new version: the enhanced TLE (eTLE). eTLEs are more accurate merely by the method of estimation and processing, which will be discussed next.

7.1.2. SPACE-DEBRIS STATES AND UNCERTAINTIES

How can modelling and simulation address the current gaps and limitations in space surveillance and tracking data for the purpose of debris analysis and orbit predictions?

Covariance data, or any form of an error estimate or estimation residuals, are essential for proper error propagation, which purpose is to provide an estimate of the possible volume containing the state over time. The error volumes are vital for defining (radar) search volumes, object correlation, conjunction analysis, and re-entry predictions, amongst others. The covariance and a number of interesting error characteristics can be estimated using only TLE data, given a number of TLE states for a particular object, within a time window, are available.

Due to the challenging environment of the lower part of LEO, the final month of the Gravity Field and Steady-State Ocean Circulation Explorer (GOCE) is studied. Both

enhanced and classic TLEs were found to be released simultaneously, over this period. Moreover, high-accuracy GPS solutions are also available for comparison.

The temporal bias is an offset from the TLE epoch to the epoch where the TLE is actually most accurate. This bias is in the order of the update interval, which typically ranges in the order of hours to days. The bias is negative for classic TLEs and is demonstrated to be positive for enhanced TLEs. The error of eTLEs thus first becomes smaller when propagated into the future, before growing larger beyond the interval of the temporal bias.

During the period studied, eTLEs are twice as accurate as classic TLEs at the published epoch. Also, the rate of error growth of eTLEs is a factor three smaller when propagating forward compared to propagating backward, both over two days. The forward shift of the epoch with minimum error, improved propagation stability, and the overall better accuracy of eTLEs makes them much more suited for forward propagation applications. Extra caution should be taken for applications that require backward propagation, such as stitching TLE solutions.

The improvements are by design and a result of eTLEs being estimated from pseudo observations derived from high-precision orbit determination (HPOD) states that are also propagated beyond the TLE epoch. When converting TLEs for non-SGP4 applications, advantage should be taken of the maximum accuracy by accounting for the temporal bias.

Robust least-squares regression is able to handle noisy data and uses only publicly available (e)TLEs. It is preferable over previous data binning and differencing methods for estimating the temporal bias, instantaneous (co)variance, and strong correlations in the absence of external data sources.

Error characteristics estimated using only (e)TLE data are verified by using GPS data. The temporal bias is estimated with an error of less than 3 % for both TLE types. The standard deviations for the significant error components are overestimated by up to 50 %. Strong correlation coefficients of more than ± 0.5 are also obtained accurately, allowing the cross couplings to have an important contribution during state error propagation when relevant.

For re-entry predictions the ballistic coefficient is an important parameter for the rate of decay, and the likely re-entry epochs. In orbit estimation the atmospheric density model and the spacecraft model (e.g., ballistic coefficient) are coupled through the drag acceleration. As a result, the TLE-reported ballistic coefficient is model dependent and in practice very unreliable. When a different atmospheric density model is considered for the re-entry prediction, the parameter must be re-estimated. The ballistic coefficient of a given satellite for a given atmospheric model must be estimated by a process called retrofitting.

Together, the estimated covariance data and ballistic coefficient supplement the TLE state estimate for the purpose of space-debris orbit predictions. These models that were derived and implemented are able to resolve some of the gaps and limitations in the by-far largest public database of space-debris objects.

7.1.3. RE-ENTRY PREDICTIONS

What are the primary drivers of short-term re-entry prediction accuracy? How well do currently operational re-entry predictions perform and how can they be further improved?

Current short-term re-entry predictions apply either a window on the predicted (nominal) re-entry epoch or on the ballistic coefficient. The fact that in the past a significant number of cases has fallen outside predicted confidence windows demonstrates that these approaches are not a reliable substitute for state-error propagation.

The effect of different (error) components on short-term re-entry predictions can only be investigated by first considering high-fidelity error and dynamics models. To this end, a six degrees-of-freedom (6DOF) state-error propagator is used to study the re-entry of the GOCE satellite.

The re-entry epoch bias is primarily determined by the atmospheric bias and the spacecraft attitude evolution. The attitude evolution was shown to have a large impact on the re-entry epoch accuracy. In fact, using the wrong assumptions can lead to re-entry predictions that are outside the predicted confidence bounds, caused by the introduction of an unwanted bias. In any case, a complete range of likely attitude scenarios needs to be considered. The atmospheric bias is a product of the systematic errors in the atmospheric density model and the spacecraft aerodynamic model. The bias can lead to significant under- or overestimation of the atmospheric accelerations during re-entry. The systematic error is between 15 and 23 % on the total aerodynamic acceleration during the last month of GOCE.

Fortunately, the atmospheric bias can be estimated by comparing the predicted and actual dynamical behaviour of the satellite. Using GPS-derived accelerations, this bias can be estimated with high accuracy and frequency. Due to the coupling between the atmospheric density model and the spacecraft model (e.g., ballistic coefficient), the TLE-reported ballistic coefficient cannot be directly used, when a different atmospheric density model is considered. Instead, this parameter must be estimated by a process called retrofitting. The obtained biases have a lower accuracy and coarser temporal resolution. To improve the accuracy, the estimates need to be averaged over an interval of a few days, further reducing the temporal resolution. This becomes problematic if the atmospheric bias is not stable over the period considered.

The spacecraft attitude evolution has a significant effect on the prediction accuracy in the case of elongated and complex shapes. For GOCE, the re-entry can take roughly three times longer with a stable attitude (for minimum cross-sectional area) compared to tumbling, as the mean ballistic coefficient is much higher than in a stable frontal configuration. Determining the transition point where the attitude motion behaviour changes from stable to tumbling is difficult, and requires knowledge on the spacecraft, and careful modelling and analysis.

The re-entry epoch accuracy, on the other hand, is primarily driven by the atmospheric uncertainty. The initial translational uncertainty has a small contribution, but becomes larger closer to re-entry. Although GPS orbit solution is four orders of magnitude more accurate than for TLE, GPS-based predictions are 35 % more precise than TLE-based.

The predicted decay-epoch distributions are not symmetric and are shown to be slightly log-normal. Several simplifications to the re-entry prediction method are made to approach methods that are in use today. A nominal state derived by choosing mean values for all uncertainties is shown to be very close to the actual mean of the full uncertainty distribution. However, assuming a symmetric interval about the nominal point will result in solutions outside the ±20 % interval on the upper tail. An asymmetric interval can be obtained by adding a factor of ±12 % to the ballistic coefficient and additionally propagating these extrema. However, a general approach for choosing this value is lacking and the results are very sensitive to the choice of the factor. The limited precision affects the operational application of re-entry predictions significantly and only allows for meaningful impact-time and impact-location windows shortly before actual re-entry, in the order of a couple of hours.

Several drivers for re-entry predictions have been identified, that either affect the prediction accuracy or prediction precision. For the case study, real-time operational predictions and post-re-entry research predictions from literature have been shown to operate on various levels of simulation fidelity and specificity of spacecraft modelling. At least for the case study, it was shown that a move towards high-fidelity and specific models, including error models, can help improve the re-entry predictions.

7.1.4. PROPAGATION OF SPACE DEBRIS

How can the propagation of space-debris trajectories be made more efficient and robust?

Regularisation offers an improved dynamically and mathematically stable formulation of the equations of motion. Dromo is a modern regularised formulation that compares favourably against other regularised formulations.

A major practical challenge of regularised methods is propagating a given state to a specific epoch. This limitation arises from the time transformation, in which time becomes a dependent variable to be numerically solved. Therefore, time, too, is prone to numerical truncation and round-off errors. Moreover, iterative root-finding is used to stop the integration at the given epoch, which itself introduces a third estimation error.

Three distinct root-finding methods to obtain a solution at a fixed physical time are identified and compared: Halley's method, bi-sectioning and (Hermite) interpolation. Halley's method is shown to be the most accurate, but also the most computationally expensive technique. Hermite interpolation requires no iterations and is more efficient than bi-sectioning, but requires the most effort to implement.

Dromo is only absolutely more accurate than Cowell's method, using Cartesian coordinates, and modified equinoctial elements (MEE) on problems with highly-elliptical orbits ($e \approx 0.95$). Over a wide range of LEOs, Dromo requires less function evaluations for a given accuracy. The difference compared to the other methods reduces when the orbits are more circular, have a lower altitude, and include atmospheric perturbations. Considering an orbit similar to that of the International Space Station (ISS), Dromo takes up to three times less function evaluations than MEE and over two orders less than Cowell's propagation scheme. Only for the tightest numerical tolerances the efficiency of Dromo and MEE converged on this problem.

A multi-step numerical integrator, such as Adams-Bashforth-Adams-Moulton, takes advantage of the linearity of the Dromo scheme and can further improve the efficiency; it requires up to five times less function evaluations when compared to Dormand-Prince Runge-Kutta. Unlike for Cowell and MEE, the multi-step integrator is shown to not affect the maximum accuracy of Dromo, over the orbit propagation problems analysed. This suggests that the Dromo formulation is very linear and the errors are driven by numerical round-off, rather than truncation.

The research has shown propagation of space-debris trajectories using regularised equations of motion can improve the accuracy and reduce the number of function evaluations, but also introduces practical challenges. In the thesis solutions are proposed, resulting in robust methods for trajectory propagation.

7.1.5. ERROR PROPAGATION OF SPACE DEBRIS

How can verified numerical analysis techniques be applied to space-debris propagation? What are the main challenges and how can they be overcome?

The major difficulty of verified integration is controlling the overestimation, which causes the artificial and exponential growth of the solution enclosure. Due to the highly perturbed environment and the large mean motion, verified solutions of LEO satellites become unstable after mere hours of propagation time. Different orbital state formulations can improve the propagation stability, but at the cost of additional overestimation in the transformation between Cartesian coordinates.

Dromo is shown to greatly improve the verified solution stability. For a 400 km LEO, the solution is stable for nearly 300 hours. This presents a factor 60 improvement over Cartesian coordinates and at least a factor eight improvement over other orbital elements, such as USM and MEE.

The primary source of overestimation in the transformation of the initial Cartesian position and velocity uncertainty to Dromo elements is wrapping. Taylor models (TM) are able to significantly reduce the wrapping effect, but also result in a 50 % increase in propagation time.

The dependent time variable will also have an interval solution, which must be reduced to a certain time epoch for most analyses to be meaningful. A novel process for transforming the time uncertainty to additional Cartesian position and velocity uncertainty was successfully developed and demonstrated. The processes allow the solution to remain verified. The final Cartesian uncertainty consists of a collection of smaller cuboids, which, taken together, are able to represent more complex uncertainty shapes and prevent overestimation due to wrapping.

During propagation most of the uncertainty is shown to be absorbed in the (dependent) time variable, which is equivalent to an uncertainty in the position of a satellite along its orbit. By itself, time has little influence on the other orbital parameters. This makes the Dromo formulation very suited for representing and absorbing the growth of orbital uncertainty.

Verified regularised orbit propagation is sensitive to the tuning parameters of the verified solver. Not all combinations result in satisfactory solutions and certain combinations are both less stable and computationally more expensive. A Pareto front can be

used to represent the trade-off between propagation stability and cost, and to identify the most interesting combinations of the tuning parameters.

The propagation stability improves with increasing orbital altitude, with solutions over the entire range of 250 to 1500 km. Near-circular orbits are most stable and no solutions are obtained for eccentricities beyond $e = 0.4$. The inclination has a marginal effect on the solution stability, with the least stable inclination at 70 degrees (30 % shorter forecasting time).

This verified regularised propagator is shown to be much more stable than any known previously published efforts. This allows the forecasting window to be prolonged from several hours to several weeks, improving the practical application of interval methods for space-debris predictions.

7.2. RECOMMENDATIONS

Several improvements to space-debris state prediction methods are suggested and investigated in this research. However, as space is increasingly "congested, contested, and competitive" the demanding space-debris problem is only becoming more complex and potentially severe. In this section recommendations for future research into this topic are made.

7.2.1. SPACE-DEBRIS SITUATIONAL AWARENESS

A growing awareness of space debris in the last two decades has seen a promising development of SSA by various nations and space agencies. However, for the moment this remains mostly complementary and thus dependent on the SSN. SSA is shown to be of high commercial and strategic importance. Moreover, due to the global nature of the space domain, SSA should be a multi-nation effort at the very least. So, much like the need to have independent GNSS capabilities, the European nations should desire a fully independent European SSA capability. Broadly, this requires research into space surveillance network architecture and design, sensors, data sharing, and estimation and prediction models.

The orbital ephemeris format, data sharing, and estimation and prediction models are highly interlinked, as discussed thoroughly in this thesis.

Regarding data sharing, enhanced TLEs show that as early as 2013 the estimation of TLEs started moving away from SGP4 towards numerical methods in the background with TLEs merely as the publishing format. This artificially improves the accuracy, promotes the continued use and development of SGP4/TLE-based tooling, and persuades third parties to keep generating and sharing TLEs. A common format beyond TLEs is needed that is more accurate, easy to use and share, and most importantly includes covariance data. A good candidate is the Orbit Ephemeris Message (OEM), in combination with the Orbit Parameter Message (OPM) by the Consultative Committee for Space Data Systems (CCSDS) [150]. Ultimately, a proper choice of format and desired accuracies should be driven top-down, by the SSA needs, rather than bottom-up, by the surveillance network and strategic interests. Research is necessary on what orbital parameters, and their quality and frequency, are required to successfully perform SSA and space traffic management (STM) activities in the current and also future space environment.

There is a growing trend towards more networked and smarter systems, especially in the case of mega constellations. These systems should be able to both autonomously perform collision avoidance, as well as share (planned) avoidance responses with operators and other autonomous systems. Topics such as manoeuvre deconfliction, responsibility, and timing are all necessary to study in the context of autonomous systems.

Models developed for supplementing TLE data with estimates of the covariance and ballistic coefficient were shown to partly address some of the gaps and limitations in TLEs. Ultimately, it is necessary to replace TLEs with a more modern format and include this information as obtained directly from the estimation process. However, this either requires the cooperation of the United States government or another organisation, with similar space-debris surveillance capabilities, and a desire to publicly provide and maintain a catalog. In the latter case, the architecture of such a network, the types of sensors, and models for the catalog, all need to be investigated to suit the needs of the space environment for decades to come.

A serious, but likely, scenario is that TLEs remain prevalent in the coming decades. In this scenario, it is important to continue to research possible improvements of TLE ephemeris. In this thesis, a method is developed for deriving high-dimensional covariance data. Similar, processing of TLEs should be investigated. For instance, through understanding the HPOD models and estimation methods underlying eTLEs, the process of creating eTLEs can be carefully reversed to a certain degree. A level of accuracy could be achieved that lies somewhere in between that of eTLEs and the unknown original HPOD. Conveniently, such a state is directly suitable for high-fidelity predictions.

7.2.2. RE-ENTRY PREDICTIONS

The re-entry predictions of GOCE show promising results for using high-fidelity re-entry predictions compared to traditional methods. The computational expense is negligible when considering the limited number of high-risk objects for which these predictions are desired. The only disadvantage is the required object knowledge and modelling. It is recommended to investigate the usage of basic or analytic shapes for the aerodynamic modelling for such trajectory predictions. This holds especially if these shape parameters can be related to already existing resources, such as the Database and Information System Characterising Objects in Space (DISCOS) maintained by the European Space Agency (ESA).

What constitutes high-risk objects is another possible line of research, and should include factors such as size, the presence of materials able to survive the stresses of atmospheric re-entry, and also the effect of attitude.

Assumptions on the spacecraft attitude can result in discrete re-entry scenarios and have a significant effect on the predicted re-entry epoch. Re-entry predictions should allow for the various scenarios and in the case of multiple likely scenarios a joint prediction. It is recommended to research both the range of possible scenarios, as well as the unification into a continuous re-entry prediction solution from several scenarios.

The atmospheric uncertainty is driving both the accuracy and precision of re-entry predictions. It is demonstrated that the systematic errors can be estimated and therefore corrected for. At present, the random error of atmospheric density models results in a $\pm 20\,\%$ random error on the predicted re-entry epoch. At two days in advance, this

translates to nearly 10 hours. The corresponding possible impact location on Earth is somewhere along the ground track of six orbital revolutions. To improve short-term re-entry predictions, improvements in thermospheric density and wind prediction models, and new and better forecasting of space-weather proxies are necessary. Especially additional measurement data of this region are needed to improve our knowledge and ultimately these models.

7.2.3. SPACE-DEBRIS STATE AND UNCERTAINTY PROPAGATION

Regularised methods are often benchmarked on exotic high-elliptical and hyperbolic orbits, offering an accuracy that is simply beyond the capability of more conventional formulations. This is useful for certain specific applications, such as the long-term integration of near-Earth asteroid trajectories. For near-circular LEOs, regularised methods are not necessarily more accurate than other methods, but can still provide a significant reduction in the number of function evaluations. Factors, such as CPU time per function evaluation and ease of implementation, should be taken into account when comparing different methods. However, for applications where the absolute number of function evaluations is important, regularised methods can provide numerical benefits and even enable unique capabilities. A broad survey of possible applications of regularised orbit propagation is recommended, such as for real-time problems (with hardware).

The current forecasting window of verified solutions is increased from the order of days to weeks, making the technique more interesting for SSA analyses. Further improvements are still desired however, and alternative interval overestimation-reduction techniques from other fields should be investigated, such as interval subdivision and interval constraints.

Conjunction analysis using verified solutions of multiple satellites is promising and should be further investigated, to really understand the benefits of verified propagation for conjunction analysis. So far, only LEO was investigated; different regimes, such as MEO and GEO, are also very good candidates, the reduction of perturbing accelerations should make for more stable solutions, compared to LEO, and thus even longer forecasting times.

The instantaneous overestimation due to coordinate transformation is reduced by TM, but still remains very large. More work into practical methods for transforming the initial uncertainty is needed. Especially, considering that the initial interval is commonly derived from confidence intervals and only verified by assumption.

ACKNOWLEDGEMENTS

The entire research project was supported by the European Office for Aerospace Research and Development (EOARD) of the United States Air Force Office of Scientific Research (AFOSR) under grant FA9550-14-1-0344. EOARD is kindly acknowledged for making this dissertation possible and especially the freedom provided in directing the research project with limited overhead. The work described in Chapters 3 and 4 was in part carried out in the framework of the European Space Agency (ESA) study on "Benchmarking reentry prediction uncertainties" under contract number 400011517/15/F/MOS. The Space Debris Office (SDO) of ESA is acknowledged for kindly providing all the required GOCE observation data, supporting information, and critical review of the reports.

Looking back at all the moments and choices that led to the present day, I can see a path that is both chaotic, but, at the same time, clearly defined by a few key moments and experiences. The wonders of space exploration, and its role in humanities future, were put stage-centre during my bachelor thesis project on the topic of human travel to Mars. Studying space exploration at the section of astrodynamics and space missions (AS) came as no brainer. My master thesis project was interrupted half-way by an internship at the advanced concepts team (ACT) at ESA, a diverse and innovative group, which drove me to pursue a research career. Luckily, a PhD candidate position at AS on the topic of space debris was open. It has been transformative to work on a problem that is so multifaceted and societally relevant. For their roles, in chronological order, I would like to thank Marc Naije (BSc supervisor), Annalisa Riccardi (ACT supervisor), Ron Noomen (MSc and PhD supervisor) and Erwin Mooij (MSc and PhD supervisor and co-promoter).

Having two supervisors is always positive, which tends to result in many positive feedback loops. Of which, jokes and red ink are just two common manifestations. While most jokes remain not-safe for print (NSFP), some formed a basis for a propositions. Of the red ink I never tired, even when the pages seemed to bleed, because of the attention to detail and effort it indicated. Again, Erwin and Ron, thank you both sincerely. I am grateful to my promoter Pieter Visser for the kind chats, encouragement and final feedback on the dissertation. I also want to thank all the members for partaking in the committee and their devotion to reading my dissertation.

Staying within aerospace engineering for so long, has the advantage of seeing it from many different perspectives: student, graduate, researcher, assistant, lecturer, supervisor *et cetera*. For instance, it was wonderful to contribute to education. My most memorable experience was the work on the TU Delft Astrodynamics Toolbox (TUDAT) as course assistant, developer and maintainer. TUDAT attracts the right kind of passionate and slightly nerdy crowd. With Dominic at the helm, I am really glad that TUDAT grows stronger and more powerful each day.

Mental support is one of the most important ingredients to a successful PhD. Plenty

of which was provided by the fellowship of room 9.18: Svenja, Tim, and Günther. I treasure the great talks, walks, and food (cakes above all) we shared. No witty pun here, just my deepest gratitude. In general, I have found many kindred spirits at aerospace. In particular, I want to express gratitude to Ingo and Roy; it was really awesome to create the vision of space society Vis Viva and share it with so many others. To this day, I cannot help but bump into aerospace people around every corner; I hope that never changes.

At the core of it all, are my wonderful family and close friends. I want to thank you all for your support and being part of my life for so long. Specially, for all the times you did not remind me I still had a PhD to finish. I dedicate this work to my other half Nienke, love of my life, and my parents Harry and Marja.

Jacco Geul
Doorn, December 29, 2022

BIBLIOGRAPHY

[1] Dezfuli, H., Benjamin, A., Everett, C., Maggio, G., Stamatelatos, M., and Youngblood, R., *NASA risk management handbook*, NASA Headquarters, 1st ed., 2011.

[2] Kessler, D. J. and Cour-Palais, B. G., "Collision frequency of artificial satellites: The creation of a debris belt," *Journal of Geophysical Research: Space Physics*, Vol. 83, No. A6, 1978, pp. 2637–2646.

[3] Undseth, M., Jolly, C., and Olivari, M., "Space sustainability: The economics of space debris in perspective," *OECD Science, Technology, and Industry Policy Papers*, Vol. 1, No. 87, April 2020, doi: 10.1787/a339de43-en.

[4] OECD, *The Space Economy in Figures – How Space Contributes to the Global Economy*, Organisation for Economic Co-operation and Development, 2019, doi: 10.1787/c5996201-en.

[5] Bryce Space and Techonology, "State of the Satellite Industry Report," Tech. Rep. SIA-SSIR-2021, Satellite Industry Association, 2021.

[6] Global Future Council on Space Technologies 2019-2020, "Six ways space technologies benefit life on Earth," Tech. Rep. WEF-GFC-2020-10-16, World Economic Forum, 2020.

[7] Raitt, D. and Battrick, B., "The Impact of Space Activities upon Society," Tech. Rep. ESA BR-237, European Space Agency, 2005.

[8] ISECG, "Benefits Stemming from Space Exploration," Tech. Rep. ISECG-2013-09-20, International Space Exploration Coordination Group, 2013.

[9] Liou, J., Anilkumar, A., Bastida, B., Hanada, T., Krag, H., Lewis, H., Raj, M., Rao, M., Rossi, A., and Sharma, R., "Stability of the future LEO environment – an IADC comparison study," *Proceedings of the 6th European Conference on Space Debris*, Vol. 723, 2013, pp. 1–7, Paper 199.

[10] Vallado, D. A. and Griesbach, J. D., "Simulating Space Surveillance Networks," *AAS/AIAA Astrodynamic Specialist Conference, Girdwood, Alaska*, 2011, pp. 1–20, Paper AAS 11-580.

[11] Bugos, S., "Russian ASAT Test Creates Massive Debris," *Arms Control Today*, Vol. 51, 2021, pp. 30–31.

[12] Weeden, B. and Samson, V., "Global Counterspace Capabalities - An Open Source Assessment," Tech. Rep. 2022/04 rev 2, Secure World Foundation, 2022.

[13] Kelso, T., "Analysis of the Iridium 33-Cosmos 2251 collision," *Advances in the Astronautical Sciences*, Vol. 135, 2009, pp. 1157–1172, Paper AAS 09-368.

[14] Oltrogge, D., Strah, M., Skinner, M. A., Rovetto, R. J., Lacroix, A., Kumar, A. A., Grattan, K., Francillout, L., and Alonso, I., "Recommendations of the IAF Space Traffic Management Terminology Working Group," *International Association for the Advancement of Space Safety Conference*, Octobre 2021, pp. 1–7.

[15] Johnson, N. L., "Medium Earth Orbits: is there a need for a third protected region?" *61st International Astronautical Congress, Prague, Czech Republic*, 2010, pp. 1–11, JSC-CN-21489.

[16] European Space Agency, "ESA Space Debris Mitigation Compliance Verification Guidelines," Tech. Rep. ESSB-HB-U-002, European Space Research and Technology Centre, ESA, 2015.

[17] Krag, H., Flohrer, T., and Lemmens, S., "Consideration of space debris mitigation requirements in the operation of LEO missions," *Space Operations: Experience, Mission Systems, and Advanced Concepts*, edited by M. Schmidhuber, C. Cruzen, and J. Kehr, chap. 23, American Institute of Aeronautics and Astronautics, Inc., 2013, pp. 413–429, doi: 10.2514/5.9781624102080.0413.0430.

[18] Bauer, W., Romberg, O., Wiedemann, C., Drolshagen, G., and Vörsmann, P., "Development of in-situ space debris detector," *Advances in Space Research*, Vol. 54, No. 9, 2014, pp. 1858–1869.

[19] Flohrer, T. and Krag, H., "Space Surveillance and Tracking in ESA's SSA Programme," *Proceedings 7th European Conference on Space Debris, Darmstadt, Germany*, 2017, pp. 1–6, Paper 242.

[20] Sturdevant, R. W., "From Satellite Tracking to Space Situational Awareness: The USAF and Space Surveillance, 1957-2007," *Air Power History*, Vol. 55, No. 4, 2008, pp. 4–23.

[21] Vallado, D. A. and Cefola, P. J., "Two-Line Element Sets – Practice and Use," *63rd International Astronautical Congress, Naples, Italy*, 2012, Paper IAC-12.C1.6.13.

[22] Kelso, T. and Alfano, S., "Satellite Orbital Conjunction Reports Assessing Threatening Encounters in Space (SOCRATES)," *15th AAS/AIAA Space Flight Mechanics Conference*, Vol. 120, 2005, pp. 317–327, Paper AAS 05-124.

[23] Lhane, M., "The development of an artificial satellite theory using a power-law atmospheric density representation," *2nd Aerospace Sciences Meeting*, 1965, pp. 1–29, doi: 10.2514/6.1965-35.

[24] Hoots, F. R. and Roehrich, R. L., "Models for Propagation of NORAD Element Sets," Tech. Rep. Spacetrack Report No. 3, Aerospace Defense Command, December 1980.

[25] Vallado, D., Crawford, P., Hujsak, R., and Kelso, T., "Revisiting Spacetrack Report #3," *AIAA/AAS Astrodynamics Specialist Conference and Exhibit*, 2006, pp. 1–94, doi: 10.2514/6.2006-6753.

[26] Hejduk, M. D., Casali, S. J., Cappellucci, D. A., Ericson, N. L., and Snow, D. E., "A Catalogue-Wide Implementation of General Perturbations Orbit Determination Extrapolated From Higher Order Orbital Theory Solutions," *Advances in the Astronautical Sciences*, Vol. 148, 2013, pp. 619–632.

[27] Wang, R., Liu, J., and Zhang, Q., "Propagation errors analysis of TLE data," *Advances in Space Research*, Vol. 43, No. 7, 2009, pp. 1065–1069, doi: 10.1016/j.asr.2008.11.017.

[28] Johnson, N. L., "U.S. Space Surveillance," *Advances in Space Research*, Vol. 13, No. 8, 1993, pp. 5–20, doi: 10.1016/0273-1177(93)90563-Q.

[29] Klinkrad, H., Fritsche, B., and Koppenwallner, G., "Re-Entry Prediction and On-Ground Risk Estimation," *Space Debris - Models and Risk Analysis*, edited by H. Klinkrad, chap. 9, Springer Verlag, Berlin, 2006, pp. 241–288.

[30] Chatters, E. and Crothers, B. J., "Space Surveillance Network," *Space Primer AU-18*, Vol. 18, Air University Press, 2nd ed., 2009, pp. 249–258.

[31] Flohrer, T., *Optical Survey Strategies and their Application to Space Surveillance*, Schweizerischen Geodätischen Kommission, Zurich, 2012.

[32] Missile Defense Agency, "Upgraded Early Warning Radars, AN/FPS-132," Tech. Rep. Fact Sheet 16-MDA-8777, Missile Defense Agency, 2016.

[33] Hack, P. J., Carbaugh, K., and Simon, K. J., "Automated Space Surveillance Using the AN/FSY-3 Space Fence System," *Advanced Maui Optical and Space Surveillance Technologies*, 2016, pp. 1–9.

[34] Allen, R. S., Donatelli, D. E., and Picardi, M. C., "Correction for Ionospheric Refraction for COBRA DANE," *Air Force Surveys in Geophysics*, 1977, doi: 10.21236/ada053222.

[35] Pechkis, D. L., Pacheco, N. S., and Botting, T. W., "Statistical Approach to the Operational Testing of Space Fence," *IEEE Aerospace and Electronic Systems Magazine*, Vol. 31, No. 11, 2016, pp. 30–39.

[36] Binnie, J., "Qatari long-range radar procurement moves forward," *IHS Jane's Defence Weekly*, dec 2016.

[37] Ronse, A. and Mooij, E., "Statistical Impact Prediction of Decaying Objects," *Journal of Spacecraft and Rockets*, Vol. 51, No. 6, 2014, pp. 1797–1810, doi: 10.2514/1.A32832.

[38] Picone, J. M., Hedin, A. E., Drob, D. P., and Aikin, A. C., "NRLMSISE-00 Empirical Model of the Atmosphere: Statistical Comparisons and Scientific Issues," *Journal of Geophysical Research*, Vol. 107, No. A12, 2002, pp. 1468–1483, doi: 10.1029/2002JA009430.

[39] Vallado, D. A. and Crawford, P., "SGP4 Orbit Determination," *AIAA/AAS Astrodynamics Specialist Conference and Exhibit*, 2008, pp. 18–21.

[40] Peterson, G. E., Gist, R. G., and Oltrogge, D. L., "Covariance generation for space objects using public data," *AAS/AIAA Space Flight Mechanics Meeting*, 2001, pp. 201–214.

[41] Deguine, B., Foliard, J., Alby, F., Donath, T., Bouchard, J., and Quillien, C., "Covariance Modelling In Satellite Collision Risk Activities," *AIAA/AAS Astrodynamics Specialist Conference and Exhibit*, 2002, doi: 10.2514/6.2002-4631.

[42] Osweiler, V. P., *Covariance Estimation and Autocorrelation of NORAD Two-Line Element Sets*, MSc thesis report, Air Force Institute of Technology, 2006.

[43] Legendre, P., Deguine, B., Garmier, R., and Revelin, B., "Two Line Element Accuracy Assessment Based On A Mixture of Gaussian Laws," *AIAA/AAS Astrodynamics Specialist Conference and Exhibit*, 2006, pp. 1–13, doi: 10.2514/6.2006-6518.

[44] Levit, C. and Marshall, W., "Improved orbit predictions using two-line elements," *Advances in Space Research*, Vol. 47, No. 7, 2011, pp. 1107–1115, doi: 10.1016/j.asr.2010.10.017.

[45] Flohrer, T., Krag, H., and Klinkrad, H., "Assessment and Categorization of TLE Orbit Errors for the US SSN Catalogue," *Advanced Maui Optical and Space Surveillance Technologies Conference*, 2008, pp. 1–12.

[46] Flohrer, T., Krag, H., and Klinkrad, H., "ESA's process for the identification and assessment of high-risk conjunction events," *Advances in Space Research*, Vol. 44, No. 3, 2009, pp. 355–363, doi: 10.1016/j.asr.2009.04.012.

[47] Vallado, D. A., Virgili, B. B., and Flohrer, T., "Improved SSA Through Orbit Determination of Two-Line Element Sets," *6th European Conference on Space Debris*, Vol. 2013, No. April, 2013, pp. 22–25.

[48] Doornbos, E., *Thermospheric Density and Wind Determination from Satellite Dynamics*, PhD thesis report, Delft University of Technology, 2011.

[49] Mason, J., *Development of a MATLAB/STK TLE Accuracy Assessment Tool, in Support of the NASA Ames Space Traffic Management Project*, MSc thesis report, International Space University, 2009.

[50] Kelso, T., "Validation of SGP4 and IS-GPS-200D against GPS precision ephemerides," *AIAA Space Flight Mechanics Conference*, 2007, pp. 1–14, Paper AAS 07-127.

[51] Legendre, P., Garmier, R., Revelin, B., and Delevault, S., "Improvement of the TLE accuracy model based on a Gaussian mixture depending on the propagation duration," *AIAA/AAS Astrodynamics Specialist Conference and Exhibit*, 2008, doi: 10.2514/6.2008-6772.

[52] Rousseeuw, P. J. and Leroy, A. M., *Robust regression and outlier detection*, John wiley & sons, 1987.

[53] Strizzi, J. D., *An Improved Algorithm for Satellite Orbit Decay and Re-Entry Predictions*, MSc Thesis, Massachusetts Institute of Technology, 1993.

[54] Klinkrad, H., "Methods and Procedures for Re-Entry Predictions at ESA," *European Conference on Space Debris*, 2013, pp. 1–8, ESA SP-723.

[55] Anselmo, L. and Pardini, C., "Satellite reentry predictions for the Italian civil protection authorities," *Acta Astronautica*, Vol. 87, 2013, pp. 163–181, doi: 10.1016/j.actaastro.2013.02.004.

[56] Ikeda, S., Tajima, T., Abe, J., and Matsuda, I., "Improved Re-Entry Prediction Method Using the Last-Minute Motion of Re-Entering Objects," *SpaceOps Conference*, 2014, pp. 1–10, doi: 10.2514/6.2014-1836.

[57] Lefebvre, S., *An Analysis of Tracking and Impact Predictions*, MSc Thesis, Air Force Institute of Technology, 1991, No. AFIT/GSO/ENG/91D-11.

[58] Storz, M. F., Bowman, B. R., Branson, M. J. I., Casali, S. J., and Tobiska, W. K., "High accuracy satellite drag model (HASDM)," *Advances in Space Research*, Vol. 36, No. 12, 2005, pp. 2497–2505, doi: 10.1016/j.asr.2004.02.020.

[59] Visser, P., Doornbos, E., van den IJssel, J. A. A., and Da Encarnação, J. T., "Thermospheric density and wind retrieval from Swarm observations," *Earths, Planets and Space*, Vol. 65, No. 11, 2013, pp. 1319–1331, doi: 10.5047/eps.2013.08.003.

[60] Vallado, D. a. and Finkleman, D., "A critical assessment of satellite drag and atmospheric density modeling," *Acta Astronautica*, Vol. 95, 2014, pp. 141–165, doi: 10.1016/j.actaastro.2013.10.005.

[61] Wit, T. D. D. and Bruinsma, S., "The 30 cm radio flux as a solar proxy for thermosphere density modelling," *Journal of Space Weather and Space Climate*, Vol. 7, No. A9, 2017, doi: 10.1051/swsc/2017008.

[62] Crowther, R., "Re-entry Aerodynamics Derived from Space Debris Trajectory Analysis," *Planetary and Space Science*, Vol. 40, No. 5, 1992, pp. 641–646, doi: 10.1016/0032-0633(92)90004-8.

[63] Bowman, B. R. and Stan, H., "Drag coefficient variability at 100-300 km from the orbit decay analyses of rocket bodies," *AIAA/AAS Astrodynamics Specialist Conference*, 2007, pp. 1–16, Paper AAS 07-262.

[64] Koppenwallner, G., Fritsche, B., Lips, T., and Klinkrad, H., "SCARAB - A Multi-Disciplinary Code for Destruction Analysis of Spacecraft During Re-Entry," *European Symposium on Aerothermodynamics for Space Vehicles*, 2005, pp. 281–286, ESA SP-563.

[65] Desai, P. N., Schoenenberger, M., and Cheatwood, F. M., "Mars Exploration Rover Six-Degree-of-Freedom," *Journal of Spacecraft and Rockets*, Vol. 43, No. 5, 2006, pp. 1019–1025, doi: 10.2514/1.6008.

[66] Neuenfeldt, B., *A survey of uncontrolled satellite reentry and impact prediction*, MSc Thesis, Naval Postgraduate School, 1993.

[67] Terejanu, G., Singla, P., Singh, T., and Scott, P. D., "Uncertainty Propagation for Nonlinear Dynamic Systems Using Gaussian Mixture Models," *Journal of Guidance, Control, and Dynamics*, Vol. 31, No. 6, 2008, pp. 1623–1633, doi: 10.2514/1.36247.

[68] Prabhakar, A., Fisher, J., and Bhattacharya, R., "Polynomial Chaos-Based Analysis of Probabilistic Uncertainty in Hypersonic Flight Dynamics," *Journal of Guidance Control, and Dynamics*, Vol. 33, No. 1, 2010, pp. 222–234, doi: 10.2514/1.41551.

[69] Halder, A. and Bhattacharya, R., "Dispersion Analysis in Hypersonic Flight During Planetary Entry Using Stochastic Liouville Equation," *Journal of Guidance, Control, and Dynamics*, Vol. 34, No. 2, 2011, pp. 459–474, doi: 10.2514/1.51196.

[70] Plazolles, B., Spel, M., Rivola, V., and El Baz, D., "Monte-Carlo Analysis of Object Reentry in Earth's Atompshere Based on Taguchi Method," *European Symposium on Aerothermodynamics for Space Vehicles*, 2015, pp. 1–8.

[71] Virgili, B. B., Flohrer, T., Lemmens, S., and Krag, H., "GOCE Re-entry Campaign," *International GOCE User Workshop*, 2014, pp. 1–7, ESA SP-728.

[72] Marcos, F. A., "Accuracy of atmospheric drag models at low satellite altitudes," *Advances in Space Research*, Vol. 10, No. 3-4, 1990, pp. 417–422, doi: 10.1016/0273-1177(90)90381-9.

[73] King-Hele, D., *Satellite Orbits in an Atmosphere: Theory and Applications*, Blackie and Son Ltd., 1987.

[74] Anderson, J., *Hypersonic and High-Temperature Gas Dynamics*, AIAA, 2006.

[75] Consultative Committee for Space Data Systems, "GOCE Stand-alone Aerodynamic Model How-to," Tech. Rep. GO-TN-AI-0179, Thales Alenia Space, 2010.

[76] Blanchard, R. C. and Buck, G. M., "Rarefied-flow Aerodynamics and Thermosphere Structure from Shuttle Flight Measurements," *Journal of Spacecraft and Rockets*, Vol. 23, No. 1, 1986, pp. 18–24, doi: 10.2514/3.25078.

[77] Wilmoth, R. G., Blanchard, R. C., and Moss, J. N., "Rarefied Transitional Bridging of Blunt Body Aerodynamics," *International Symposium on Rarefied Gas Dynamics*, 1998, pp. 1–8, doi: 10.5555/888016.

[78] Sechi, G., André, G., Andreis, D., and Saponara, M., "Magnetic attitude control of the GOCE satellite," *International ESA Conference on Guidance, Navigation and Control Systems*, 2006, pp. 1–10, Paper ESA SP-606.

[79] Mooij, E., *The Motion of a Vehicle in a Planetary Atmosphere*, Series 08: Astrodynamics and Satellite Systems 01, Delft University Press, 1997.

[80] Klinkrad, H., "On the Use of Atmosphere Models in Re-Entry Predictions," *Environment Modelling for Space-based Applications*, 1996, pp. 287–298, ESA SP-392.

[81] Visser, P. N. A. M. and van den IJssel, J. A. A., "Orbit determination and estimation of non-gravitational accelerations for the GOCE reentry phase," *Advances in Space Research*, Vol. 58, No. 9, 2016, pp. 1840–1853, doi: 10.1016/j.asr.2016.07.013.

[82] Geul, J., Mooij, E., and Noomen, R., "TLE Uncertainty Estimation using Robust Weighted Differencing," *Advances in Space Research*, Vol. 59, No. 10, 2017, pp. 2522–2535, doi: 10.1016/j.asr.2017.02.038.

[83] Wakker, K. F., "Elementary analysis of orbit perturbations," *Fundamentals of Astrodynamics*, chap. 20, Institutional Repository Delft University of Technology, 2015, pp. 555–584.

[84] Saltelli, A., Tarantola, S., Campolongo, F., and Ratto, M., *Sensitivity Analysis in Practice - A Guide to Assessing Scientific Models*, John Wiley & Sons, Chichester, 2004.

[85] Marino, S., Hogue, I. B., Ray, C. J., and Kirschner, D. E., "A methodology for performing global uncertainty and sensitivity analysis in systems biology," *Journal of Theoretical Biology*, Vol. 254, No. 1, 2008, pp. 178–196, doi: 10.1016/j.jtbi.2008.04.011.

[86] Hoots, F. and France, R., "The Future of Artificial Satellite Theories," *Celestial Mechanics and Dynamical Astronomy*, Vol. 66, No. 1, 1997, pp. 51–60.

[87] Stiefel, E. and Scheifele, G., *Linear and Regular Celestial Mechanics*, Springer-Verlag, 1971.

[88] Bond, V. R. and Allman, M. C., *Modern Astrodynamics*, Princeton University Press, 1996.

[89] Waldvogel, J., "Quaternions and the perturbed Kepler problem," *Celestial Mechanics and Dynamical Astronomy*, Vol. 95, No. 1-4, Aug 2006, pp. 201–212, doi: 10.1007/s10569-005-5663-7.

[90] Fukushima, T., "New Two-body Regularization," *The Astronomical Journal*, Vol. 133, No. 1, 2007, pp. 1–10, doi: 10.1086/509606.

[91] Fukushima, T., "Numerical Comparison of Two-body Regularizations," *The Astronomical Journal*, Vol. 133, No. 6, 2007, pp. 2815–2824, doi: 10.1086/518165.

[92] Waldvogel, J., "Fundamentals of Regularization in Celestial Mechanics and Linear Perturbation Theories," *Fundamentals of Regularization in Celestial Mechanics and Linear Perturbation Theories*, 2007, pp. 168–184, doi: 10.1201/b10365-14.

[93] Peláez, J., Hedo, J. M., and Rodríguez de Andrés, P., "A Special Perturbation Method in Orbital Dynamics," *Celestial Mechanics and Dynamical Astronomy*, Vol. 97, No. 2, 2007, pp. 131–150, doi: 10.1007/s10569-006-9056-3.

[94] Waldvogel, J., "Quaternions for Regularizing Celestial Mechanics - the Right Way," *Celestial Mechanics and Dynamical Astronomy*, Vol. 102, 2008, pp. 149–162, doi: 10.1007/s10569-008-9124-y.

[95] Baù, G., Bombardelli, C., and Peláez, J., "A New Set of Integrals of Motion to Propagate the Perturbed Two-body Problem," *Celestial Mechanics and Dynamical Astronomy*, Vol. 116, No. 1, 2013, pp. 53–78, doi: 10.1007/s10569-013-9475-x.

[96] Baù, G. and Bombardelli, C., "Time Elements for Enhanced Performance of the Dromo Orbit Propagator," *The Astronomical Journal*, Vol. 148, No. 3, 2014, pp. 43–58, doi: 10.1088/0004-6256/148/3/43.

[97] Broucke, R. A. and Cefola, P. J., "On the Equinoctial Orbit Elements," *Celestial mechanics*, Vol. 5, No. 3, 1972, pp. 303–310.

[98] Wakker, K. F., *Fundamentals of Astrodynamics*, Institutional Repository Delft University of Technology, 2015.

[99] Kustaanheimo, P. and Stiefel, E., "Perturbation Theory of Kepler Motion based on Spinor Regularization," *Journal für die Reine und Angewandte Mathematik*, Vol. 1965, No. 218, 1965, pp. 204–219, doi: 10.1515/crll.1965.218.204.

[100] Burdet, C. A., "Regularization of the Two Body Problem," *Zeitschrift für Angewandte Mathematik und Physik*, Vol. 18, No. 3, 1967, pp. 434–438, doi: 10.1007/BF01601283.

[101] Ferràndiz, J., "A General Canonical Transformaiton Increasing the Number of Variables with Application to the Two-body Problem," *Celestial Mechanics*, Vol. 41, No. 1968, 1988, pp. 343–357, doi: 10.1007/BF01238770.

[102] Jezewski, D. J., "A Comparative Study of Newtonian, Kustaanheimo/Stiefel, and Sperling/Burdet Optimal Trajectories," *Celestial Mechanics*, Vol. 12, No. 3, 1975, pp. 297–315, doi: 10.1007/BF01228565.

[103] Vittaldev, V., Mooij, E., and Naeije, M. C., "Unified State Model theory and application in Astrodynamics," *Celestial Mechanics and Dynamical Astronomy*, Vol. 112, No. 3, 2012, pp. 253–282, doi: 10.1007/s10569-011-9396-5.

[104] Altman, S. P., "A Unified State Model of Orbital Trajectory and Attitude Dynamics," *Celestial Mechanics*, Vol. 6, No. 4, 1972, pp. 425–446, doi: 10.1007/BF01227757.

[105] Bond, V. R. and Hanssen, V., "The Burdet Formulation of the Perturbed Two-body Problem with Total Energy as an Element," *NASA-JSC-Internal Note*, Vol. 1, No. 73-FM-86 (JSC-O8004), 1973.

[106] Vallado, D. A., *Fundamentals of Astrodynamics and Applications*, Microcosm Press, 3rd ed., 2007.

[107] Allione, M., Blackford, A., J.C.Mendez, and M.M.Wittouck, "The N-Body Problem and Special Perturbation Techniques," *Guidance, Flight Mechanics and Trajectory Optimization*, chap. Volume VI, National Aeronautics and Space Administration, 1968, pp. 1–128.

[108] Hamming, R., *Numerical methods for scientists and engineers*, Dover Publishers, 1987.

[109] Shampine, L. F. and Gordon, M. K., "Local Error and Variable Order Adams Codes," *Applied Mathematics and Computation*, Vol. 1, No. 1, 1975, pp. 47–66.

[110] Corliss, G. and Chang, Y. F., "Solving Ordinary Differential Equations Using Taylor Series," *ACM Transactions on Mathematical Software*, Vol. 8, No. 2, 1982, pp. 114–144, doi: 10.1145/355993.355995.

[111] Scott, J. R. and Martini, M. C., "High Speed Solution of Spacecraft Trajectory Problems Using Taylor Series Integration," *Journal of Spacecraft and Rockets*, Vol. 47, No. 1, 2012, pp. 199–202, doi: 10.2514/1.43459.

[112] Bergsma, M. C. W. and Mooij, E., "Application of Taylor Series Integration to Reentry Problems," *AIAA Science and Technology Forum and Exposition*, 2016, pp. 1–28, doi: 10.2514/6.2016-0024.

[113] Klinkrad, H., "The Current Space Debris Environment and its Sources," *Space Debris - Models and Risk Analysis*, edited by H. Klinkrad, chap. 2, Springer Verlag, Berlin, 2006, pp. 5–58.

[114] Patera, R. P., "General method for calculating satellite collision probability," *Journal of Guidance, Control, and Dynamics*, Vol. 24, No. 4, 2001, pp. 716–722, doi: 10.2514/2.4771.

[115] Klinkrad, H., Alacrón, J., and Sánchez, N., "Collision Avoidance for Operational ESA Satellites," *European Conference on Space Debris*, 2005, pp. 509–515.

[116] Klinkrad, H., Alarcón, J., and Sánchez, N., "Operational Collision Avoidance with Regard to Catalog Objects," *Space Debris - Models and Risk Analysis*, edited by H. Klinkrad, chap. 8, Springer Verlag, Berlin, 2006, pp. 215–240.

[117] Mason, J., Stupl, J., Marshall, W., and Levit, C., "Orbital debris–debris collision avoidance," *Advances in Space Research*, Vol. 48, No. 10, 2011, pp. 1643–1655, doi: 10.1016/j.asr.2011.08.005.

[118] Römgens, B., Mooij, E., and Naeije, M., "Satellite collision avoidance prediction using verified interval orbit propagation," *Journal of Guidance, Control, and Dynamics*, Vol. 36, No. 3, 2013, pp. 821–832, doi: 10.2514/1.57888.

[119] Celletti, A. and Chierchia, L., "On the stability of realistic three-body problems," *Communications in Mathematical Physics*, Vol. 186, No. 2, 1997, pp. 413–449, doi: 10.1007/s002200050115.

[120] Hoefkens, J., Berz, M., and Makino, K., "Controlling the wrapping effect in the solution of ODEs for asteroids," *Reliable Computing*, Vol. 9, No. 1, 2003, pp. 21–41, doi: 10.1023/A:1023009910949.

[121] Alessi, E. M., Farres, A., Jorba, À., Simo, C., Vieiro, A., and Summerer, L., "Efficient usage of self validated integrators for space applications," *ESA and Universitat de Barcelona TR-07/5202, Barcelona, Spain*, 2007.

[122] Armellin, R., Morselli, A., Di Lizia, P., and Lavagna, M., "Rigorous computation of orbital conjunctions," *Advances in Space Research*, Vol. 50, No. 5, 2012, pp. 527–538, doi: 10.1016/j.asr.2012.05.011.

[123] Urrutxua, H., Souied, Y., and Peláz, J., "Sensitivity Analysis of Regularized Orbit Formulations with Interval Arithmetic," *Advances in the Astronautical Sciences*, Vol. 168, 2019, pp. 1157–1172, Paper AAS 19-328.

[124] Valli, M., Armellin, R., Di Lizia, P., and Lavagna, M. R., "Nonlinear Mapping of Uncertainties in Celestial Mechanics," *Journal of Guidance, Control, and Dynamics*, Vol. 36, No. 1, 2013, pp. 48–63, doi: 10.2514/1.58068.

[125] Geul, J., Mooij, E., and Noomen, R., "Regularised methods for high-efficiency propagation," *Proceedings of the 2015 AAS/AIAA Specialist Conference, Vail, CO, USA*, 2015, pp. 4105–4124.

[126] Hoefkens, J., *Rigorous numerical analysis with high-order Taylor models*, PhD thesis report, Michigan State University. Department of Mathematics, 2001.

[127] Moore, R. E., *Interval analysis*, Vol. 4, Prentice-Hall Englewood Cliffs, NJ, 1966.

[128] Moore, R. E., "Interval arithmetic," *Interval analysis*, Vol. 4, chap. 1, Prentice-Hall Englewood Cliffs, NJ, 1966, pp. 8–14.

[129] Makino, K., *Rigorous analysis of nonlinear motion in particle accelerators*, PhD thesis report, Michigan State University. Dept. of Physics and Astronomy, 1998.

[130] Berz, M. and Makino, K., "New methods for high-dimensional verified quadrature," *Reliable Computing*, Vol. 5, No. 1, 1999, pp. 13–22, doi: 10.1023/A:1026437523641.

[131] Neumaier, A., "Taylor forms - use and limits," *Reliable computing*, Vol. 9, No. 1, 2003, pp. 43–79, doi: 10.1023/A:1023061927787.

[132] Makino, K. and Berz, M., "Taylor model range bounding schemes," *Third International Workshop on Taylor Methods, Miami Beach, FL*, 2004, pp. 1–70.

[133] Nedialkov, N. S., "Interval Tools for ODEs and DAEs," *Scientific Computing, Computer Arithmetic and Validated Numerics*, 2006, pp. 35–46, doi: 10.1109/SCAN.2006.28.

[134] Lin, Y. and Stadtherr, M. A., "Validated Solutions of Initial Value Problems for Parametric ODEs," *Applied Numerical Mathematics*, Vol. 57, No. 10, 2006, pp. 1145–1162, doi: 10.1016/j.apnum.2006.10.006.

[135] Nedialkov, N. S., Jackson, K. R., and Corliss, G. F., "Validated solutions of initial value problems for ordinary differential equations," *Applied Mathematics and Computation*, Vol. 105, 1999, pp. 21–68, doi: 10.1016/S0096-3003(98)10083-8.

[136] Eble, I., *Über Taylor-Modelle*, PhD thesis report, Universität Karlsruhe, 2007.

[137] Auer, E. and Rauh, A., "VERICOMP: a system to compare and assess verified IVP solvers," *Computing*, Vol. 94, No. 2-4, 2012, pp. 163–172, doi: 10.1007/s00607-011-0178-4.

[138] Wakker, K. F., "Regularization," *Fundamentals of Astrodynamics*, chap. 10, Institutional Repository Delft University of Technology, 2015, pp. 219–242.

[139] Amato, D., *Advanced orbit propagation methods applied to asteroids and space debris*, PhD thesis report, Universidad Politécnica de Madrid, Departamento de Física Aplicada a las Ingenierías Aeronáutica y Naval, 2017.

[140] Hernando-Ayuso, J., Bombardelli, C., and Baù, G., "Uncertainty propagation in the N-body problem using Dromo elements," *Acta Astronautica*, Vol. 156, 2019, pp. 252–261, doi: 10.1016/j.actaastro.2017.12.030.

[141] Stiefel, E. and Scheifele, G., "Typical perturbations," *Linear and Regular Celestial Mechanics*, chap. 5, Springer-Verlag, 1971, pp. 73–125.

[142] Bond, V. R. and Allman, M. C., "Special perturbation methods," *Modern Astrodynamics*, chap. 9, Princeton University Press, 1996, pp. 147–183.

[143] Wakker, K. F., "Perturbing forces and perturbed satellite orbits," *Fundamentals of Astrodynamics*, chap. 20, Institutional Repository Delft University of Technology, 2015, pp. 527–554.

[144] Tapley, B. D., Schutz, B. E., and Born, G. H., "Observations," *Statistical Orbit Determination*, chap. 3, Elsevier, 2004, pp. 93–158.

[145] Vallado, D. A., "Special perturbation techniques," *Fundamentals of Astrodynamics and Applications*, chap. 8, Microcosm Press, 3rd ed., 2007, pp. 491–566.

[146] Geul, J., Mooij, E., and Noomen, R., "Analysis of Uncertainties and Modeling in Short-Term Reentry Predictions," *Journal of Guidance, Control, and Dynamics*, Vol. 41, No. 6, 2018, pp. 1276–1289, doi: 10.2514/1.G003258.

[147] Stiefel, E. and Scheifele, G., "Typical perturbations," *Linear and Regular Celestial Mechanics*, chap. 6, Springer-Verlag, 1971, pp. 100–126.

[148] Montenbruck, O. and Gill, E., "Force Model," *Satellite orbits: models, methods and applications*, chap. 3, Springer Science & Business Media, 2012, pp. 53–113.

[149] Bergsma, M. and Mooij, E., "Application of Taylor-Series Integration to Reentry Problems with Wind," *Journal of Guidance, Control, and Dynamics*, 2016, pp. 2324–2335, doi: 10.2514/1.G000378.

[150] Dumontel, M., Bacchetta, A., Vinai, B., Allasio, A., and Berto, A., "Orbit Data Messages - Recommendation for Space Data System Standards," Tech. Rep. CCSDS 502.0-B-2, CCSDS Secretariat, 2009.

Curriculum Vitæ

Jacco Geul

10-10-1985 Born in Vlaardingen, The Netherlands.

Education

1998–2005 Secondary school
Regionale Scholengemeenschap, Oud-Beijerland, The Netherlands

2005–2011 Bachelor of Science in Aerospace Engineering
Delft University of Technology, Delft, The Netherlands

2011–2014 Master of Science in Space Exploration
Delft University of Technology, Delft, The Netherlands
Thesis: Neurocontrol for Global Optimisation of Low-thrust Trajectories
Supervisors: Ir. R. Noomen and dr. ir. E. Mooij

2014– Candidate Doctor of Philosophy (PhD) at Astrodynamics and Space Missions
Delft University of Technology, Delft, The Netherlands
Dissertation: On the Uncertainty of Space Debris Trajectory Predictions
Promoter: Prof. dr. ir. P.N.A.M. Visser
Co-promoter: Dr. ir. E. Mooij
Supervisors: Ir. R. Noomen and dr. ir. E. Mooij

Awards

2018 "Outstanding Paper Award for Young Scientists"
for the work presented in Chapter 3
by the Committee on Space Research (COSPAR).

Activities

During his PhD research at the section of Astrodynamics and Space Missions, Jacco Geul contributed to education, through supervision of students and teaching of courses, and development of the TU Delft Astrodynamics Toolbox (Tudat).

From 2012 to 2016, Jacco Geul was involved in the founding and the board of Society Vis Viva, which provided a forum for space professionals from various backgrounds.

Since 2019, Jacco Geul is employed at the Netherlands Organisation for Applied Scientific Research (TNO) at the department of Military Operations.

List of Publications

Journal Articles

4. **Geul, J.**, Mooij, E., and Noomen, R., "Verified Regularized Interval Orbit Propagation", *Journal of Guidance, Control, and Dynamics*, Vol. 44, No. 4, pp. 719–731, 2021.

3. **Geul, J.**, Mooij, E., and Noomen, R., "Analysis of Uncertainties and Modeling in Short-Term Re-Entry Predictions", *Journal of Guidance, Control, and Dynamics*, Vol. 41, No. 6, pp. 1276–1289, 2018.

2. Hoogendoorn, R., Mooij, E., and **Geul, J.**, "Uncertainty Propagation for Statistical Impact Prediction of Space Debris", *Advances in Space Research*, Vol. 61, No. 1, pp. 167–181, 2018.

1. **Geul, J.**, Mooij, E., and Noomen, R., "TLE Uncertainty Estimation using Robust Weighted Differencing", *Advances in Space Research*, Vol. 59, No. 10, pp. 2522–2535, 2017.

Conference Proceedings

3. **Geul, J.**, Mooij, E., and Noomen, R., "GOCE Statistical Re-entry Predictions", *7th European Conference on Space Debris*, Vol. 7, No. 1, 2017.

2. **Geul, J.**, Mooij, E., and Noomen, R., "Modelling and Assessment of the Current and Future Space Surveillance Network", *7th European Conference on Space Debris*, Vol. 7, No. 1, 2017.

1. **Geul, J.**, Mooij, E., and Noomen, R., "Regularised Methods for High-Efficiency Propagation", *Proceedings of the AAS/AIAA Astrodynamics Specialist Conference*, Vol. 156, No. 1, August 9-13, 2015, Vail (CO), USA, Paper AAS 15-697, pp. 4105–4124, 2016.

We demand rigidly defined areas of doubt and uncertainty!

Douglas Adams, The Hitchhiker's Guide to the Galaxy